Inaugural Dissertation

zur

Erlangung der Doktorwürde

der

Naturwissenschaftlich-Mathematischen Gesamtfakultät

der

Ruprecht-Karls-Universität Heidelberg

Vorgelegt von

M. Sc. Sven Mehlhose

geboren in Grimma, Deutschland

Tag der mündlichen Prüfung: 20. Mai 2019

Dissertation

submitted to the

Combined Faculty of Natural Sciences and Mathematics

Heidelberg University, Germany

for the degree of

Doctor of Natural Sciences (Dr. rer. nat.)

Presented by

M. Sc. Sven Mehlhose

Born in Grimma, Germany

Oral examination: May 20th, 2019

Biofunctionalization of GaN/AlGaN/GaN High Electron Mobility Transistors

Referees: Prof. Dr. Motomu Tanaka
Prof. Dr. Martin Eickhoff

Eidesstattliche Versicherung gemäß § 8 der Promotionsordnung der Naturwissenschaftlich-Mathematischen Gesamtfakultät der Universität Heidelberg

1. Bei der eingereichten Dissertation zu dem Thema

Biofunctionalization of GaN/AlGaN/GaN High Electron Mobility Transistors

handelt es sich um meine eigenständig erbrachte Leistung.

2. Ich habe nur die angegebenen Quellen und Hilfsmittel benutzt und mich keiner unzulässigen Hilfe Dritter bedient. Insbesondere habe ich wörtlich oder sinngemäß aus anderen Werken übernommene Inhalte als solche kenntlich gemacht.

3. Die Arbeit oder Teile davon habe ich wie folgt/bislang nicht[1)] an einer Hochschule des In- oder Auslands als Bestandteil einer Prüfungs- oder Qualifikationsleistung vorgelegt.

Titel der Arbeit:

Hochschule und Jahr:

Art der Prüfungs- oder Qualifikationsleistung:

4. Die Richtigkeit der vorstehenden Erklärungen bestätige ich.

5. Die Bedeutung der eidesstattlichen Versicherung und die strafrechtlichen Folgen einer unrichtigen oder unvollständigen eidesstattlichen Versicherung sind mir bekannt.

Ich versichere an Eides statt, dass ich nach bestem Wissen die reine Wahrheit erklärt und nichts verschwiegen habe.

Ort und Datum

Unterschrift

[1)] Nicht Zutreffendes streichen. Bei Bejahung sind anzugeben: der Titel der andernorts vorgelegten Arbeit, die Hochschule, das Jahr der Vorlage und die Art der Prüfungs- oder Qualifikationsleistung.

Abstract

The primary aim of this thesis is the creation of new electrochemical biosensor systems on solution-gated GaN/AlGaN/GaN high electron mobility transistors (HEMT) for the transduction of biological functions into electrical readouts. For this purpose, the surface of transistors was functionalized with various biomimetic and bioorganic molecular systems, such as helical peptides, lipid monalayers and membranes. The full characterization of thickness, roughness, and density of such biomimetic molecular assemblies enables to quantitatively translate the change in surface monopoles and dipoles into the carrier mobility.

In Chapter 4, monolayers of bio-inspired, non-biological helical peptides were deposited on GaN semiconductor surfaces in order to modulate the electronic band structures of GaN by macromolecular dipole moments. By covalently coupling the peptides via N- or C-terminus to the GaN surfaces, the sign (direction) of exerted dipole moments could precisely be controlled, realizing the modulation of the carrier mobility. Moreover, the chronoamperometry measurements have demonstrated the additional ferrocene terminal group enables the directed electron transfer through peptide chains via an inelastic hopping mechanism.

In Chapter 5.3, cell membrane models were deposited on the GaN surfaces pre-coated with hydrophobic, organic silane monolayers. By incorporating lipids with nitrilotriacetic acid (NTA) head groups into lipid membranes, changes in the surface potentials induced by the binding of charged recombinant proteins to the surface lipid membranes could be detected at a high sensitivity. The systematic variation of surface density of NTA lipids and the comparison with impedance spectroscopy data of bulk GaN electrodes, it has been demonstrated that the sensitivity of this system to changes in the surface charge density is as high as $\Delta Q < 0.1\ \mu C/cm^2$.

In Chapter 5.2, to accommodate the incorporation of transmembrane proteins under non-denaturing conditions, a more realistic cell membrane model, bilayer lipid membranes, was deposited on GaN by using regenerated cellulose films as the polymer support. The current-voltage characteristics clearly indicated the high electric resistance of lipid membranes, which seems promising for the detection of molecular recognition and selective material transport.

Last but not least, such molecular constructs were transferred onto the surface of molecularly thin, organic semiconductors that have shown a high charge mobility under dry conditions (Chapter 6). The preliminary attempts already demonstrated the formation of uniform lipid monolayers on organic semiconductor surfaces exposing hydrocarbon chains. Moreover, the reversible binding and unbinding of recombinant proteins has been confirmed. Although further optimization of the device geometry and Ohmic contacts are

necessary, the data suggest a large potential of all organic electronic sensors operating under water.

The obtained results highlighted the potential of the combination of biomimetic molecular constructs and inorganic and organic semiconductor devices for the highly sensitive and quantitative determination of properties and functions under physiological conditions.

Zusammenfassung

Diese Arbeit beschreibt die Entwicklung neuer elektrochemischer Biosensorsysteme auf Basis von GaN/AlGaN/GaN-Transistoren mit hoher Elektronenbeweglichkeit (engl. HEMT), die es ermöglichen biologische Funktionen in elektrische Signale zu übersetzen. Dazu wurde die Modulation der elektronischen Umgebung der Transistor Oberfläche durch Veränderungen in den Oberflächenpotentialen und -Ladungen untersucht, die durch die Funktionalisierung der GaN-Transistoroberflächen mit verschiedenen biomimetischen und bioorganischen mole-kularen Systemen erzeugt werden. Verschiedene Membran- und Monolagenmodell von bio-analogen Molekülen wurden dafür zur quantitativen Charakterisierung der Eigenschaften und Prozesse, die an solchen Systemen stattfinden, untersucht.

Biologische Systeme zeigen eine breite Reihe möglicher Molekülladungen und Dipolmomente auf. Die Modulation von elektronischen Bandenprofilen durch solche Dipolmomente wurde anhand von GaN-Halbleitern gezeigt, unter Verwendung von makromolekularen Dipolpotentialen, die von geordneten Monolagen von synthetischen, bioinspirierten, helikalen Peptiden erzeugt werden. Die kovalente Bindung der Peptide über den N- oder C-Terminus an GaN ermöglichte die kontrollierte Ausrichtung der Dipol-momente, die entweder in Richtung oder von der GaN Oberfläche weg zeigen. In Abhängigkeit von dieser Richtung zeigten die Stromspannungseigenschaften des GaN-HEMT, dass eine präzise Modulation der Ladungsträgerbeweglichkeit im zweidimensionalen Elektronengase des GaN Transistors durch den Peptiddipol erreicht wurde.

Veränderungen der Oberflächenmonopole wurden durch die Bindung von rekombinanten Proteinen an Festkörper gestützten Lipid Membranen nachgewiesen. Diese enthielten Ankerlipide mit Nitrilotriessigsäure (NTA) Kopfgruppen, welche in Gegenwart von Ni^{2+} die reversible Komplexierung von Oligohistidin markierten rekombinanten Proteinen (eGFP) ermöglicht. Änderungen in den HEMT-Strom-Spannungs-Kurven zeigten, dass Unterschiede in der Oberflächenladungsdichte Q, die durch diese Prozesse verursacht werden, mit einer hohen Empfindlichkeit von $\Delta Q < 0{,}1\ \mu C/cm^2$ nachgewiesen werden können.

Ein weiteres Membran-Modellsystem wurde durch die Funktionalisierung von GaN-HEMTs mit Lipidmembranen auf regenerierten Cellulose Polymeren entwickelt. Dies ermöglicht den Einbau von Transmembranproteinen und die Messung deren Funktionen in einer naturähnlichen Umgebung. Die Eigenschaft von Lipidmembranen wie ein elektrischer Isolator zu wirken wurde durch einen deutlichen Anstieg des Widerstands gegenüber angelegten Gate Potentialen in den HEMT Strom-Spannungs Kurven bestätigt,

was eine ausreichende Empfindlichkeit für die Bestimmung von Membranprotein Aktivitäten gewährleistet.

Das oben erwähnte Monoschichtmodell wurde schließlich auf neuartige flüssigkristalline organische Halbleitermaterialien, zur Schaffung einer neuen Klasse von Biosensorsystemen, angewendet. Erste Schritte dahin wurden durch die Bildung von Lipid Monolagen auf diesen Halbleitern und deren Betrieb in wässrigem Medium beschreiben, was bisher nicht tiefgehend untersucht wurde.

Die hier erhaltenen Ergebnisse verdeutlichen das Potenzial von kombinierten GaN-Halbleiterbauelementen und biomimetischen Molekülstrukturen zur hochempfindlichen und quantitativen Bestimmung von Eigenschaften und Funktionen biologischer und biomimetischer Systeme.

Acknowledgements

Submitting this thesis I would like to thank…

…**Prof. Dr. Motomu Tanaka** for giving me the possibility to work on this interdisciplinary project and the opportunity to spend several months at the Department of Material Chemistry in Kyoto University, Japan to broaden my personal and scientific horizon. I sincerely appreciate your scientific guidance and constant sharp critical eye on my work as well as your priority in driving me to improve as an independent researcher.

…**Prof. Dr. Martin Eickhoff** for acting as my reviewer, for the great collaboration and support within the gallium nitride projects and my frequent research stays.

…**Geshe Müntze, Daniel Stock** and **Sara Hölzel** for their mentoring on HEMT mechanics, sample preparation and the friendly athmosphere during my research stays.

…**Prof. Dr. Shunsaku Kimura** and **HeKKSaGOn** for acting as my hosts during my research stay at Kyoto University, Japan.

… **Dr. Wasim Abuillan** for the help and mentoring in all kind of questions and problems and the inspiring scientific discussions during my PhD.

…**Prof. Dr. Takashi Kato, Prof. Dr. Toshihiro Okamoto** and **Prof. Dr. Yuko Ueno** for supplying various interesting samples and opening many stimulating research opportunities.

…**Federico Amadei, Judith Thoma, Philipp Linke, Salomé Mielke, Julian Czajor, Benjamin Fröhlich, Esther Kimmle, Akihisa Yamomoto, Maryam Eshrati, Ronja Rapport, Moritz Herrmann, Stefan Kaufmann** and **Mariam Veshgini** for the support and cheerful time in the office, lab and outside of work.

…**Dr. Stefan Kaufmann and Dr. Tim Schlosser** for proof-reading my thesis and their insights on how to improve my writing.

…**Karl-Phillip Strunck** and **Soh Kushida** for the open accsess to experimental equipment.

…**Gabriele Fabry, Sybille Kürner-Winkeler** and **Mieko Yoshida** for their help on all administratory questions.

…**Michael Schukin, Lukas Scheiderer** and **Tamara Skarke** for the supportive and reliable work in the lab.

Special thanks go to my **family**, **friends** and especially **Steffy Becht** for their great support, valuable advice, necessary distraction besides the PhD, as well as making me strife to improve myself and bearing with all my shenanigans.

Table of Contents

1. Introduction

Biosensors combine the specificity and selectivity of biochemical recognition elements with a transducer, generating a quantifiable readout. In this context, label free electronic readouts such as potentiometry, conductometry and impedance measurements (Thévenot 2001) are utilized in conjecture with semiconductors as sensor platform. After the development of one of the first biosensors by Clark and Lyons in 1962 for the monitoring of a patients' blood oxygen and carbon dioxide levels over the blood pH (Clark and Lyons 1962), the recognition of biological processes has been achieved with enzymes (Müntze, Baur *et al.* 2015), deoxyribonucleic acid (DNA) strands (Thapa et al. 2012) and antibodies (Huang et al. 2013) as well. Recently, the development of such sensors was expandend to encompass further medicinal applications, such as drug development (Gebinoga et al. 2012, Makowski et al. 2013, Kang et al. 2013), diagnostics (Chen, Svedendahl et al. 2011, Zhang et al 2011) and protein detection (Kang et al. 2005, Huang et al. 2013). In nature, many of the physical and biochemical interactions of biosystems (e.g. cells) involve biological interfaces. The most prominent examples of such biointerfaces are cell membranes. The interactions at the interface are mediated by complex interplays of short and long-range forces (e.g. van der Waals, electrostatic, steric (entropic) forces, and hydration forces (Israelachvili 1985, Derjaguin 1987), often involving many elemental and synergistic processes, which are difficult to quantify directly. Thus, the design of cell membrane models with a reduced number of components is necessary to study the fundamental principles of reactions and processes at biological interfaces. Modification of planar solid surfaces with organic, biocompatible layers enables the fabrication of novel biofunctional hybrid materials. Using this approach of "supported membranes" (Sackmann 1996, Sackmann and Tanaka 2000, Tanaka and Sackmann 2005) allows for the matching of interface properties between solid surfaces and biological systems for the stress-free immobilization of artificial as well as native cell membranes and proteins onto solid-based devices (Hillebrandt et al. 1999, Purrucker et al. 2001, Hillebrandt et al. 2002). A high sensitivity to the immobilization and functionality of biosystems can be achieved by the use of semiconductors, which translate changes in surface potential from reactions at the biointerface into electronic signals (Bergveld 1986). The use of GaN as semiconductor material promises outstanding chemical and electrochemical stability over a broad frequency range (Steinhoff, Hermann *et al.* 2003, Steinhoff, Purrucker *et al.* 2003, Schaefer, Koch *et al.* 2012). This notion is further supported, since no degradation under physiological conditions is observed for GaN compared to other materials, such as Si (Allongue 1985, Bergveld 1986) and GaAs (Adlkofer 2000). As a wide band gap semiconductor (E_g = 3.4 eV) GaN further allows for a higher flexibility and control in its electronic properties by doping, as well as a high

degree of band gap engineering by alloying it with In or Al. This enables the fabrication of various complex semiconductor heterostructures, possessing high carrier densities and thus high sensitivities to their electronic surface environment. To this date several studies detailing the immobilization of biosystems on bulk GaN electrodes (Schubert, Steinhoff et al. 2009, Stine et al. 2010) have been reported. However, the use of GaN heterostructure devices as biological sensor platform has only recently drawn attention (Baur, Howgate et al. 2006, Müntze, Baur et al. 2015). In this work the use of GaN semiconductors and GaN/AlGaN/GaN high electron mobility transistors was explored as highly sensitive sensor platform for the recognition of various biological systems, molecules, proteins.

First, in Chapter 4, the potential of band gap engineering using the tunable macro molecular dipole moment of synthetic helical peptides (Morita 2000, Kaindl 2010, Frenkel 2015) to modulate the surface potential and electronic band structures in bulk GaN semiconductors and GaN/AlGaN/GaN heterostructures was investigated (in collaboration with Prof. Dr. S. Kimura, Kyoto Univ. and Prof. Dr. M. Eickhoff, Univ. Bremen). The peptides, based on a leucine - α-amino isobutyric acid (Leu - Aib)$_n$ sequence, form a stable α-helix and through interdigitation of the side chains are able to form well-packed self-assembled monolayers (Morita and Kimura 2003, Kitagawa 2004). Covalent grafting of these peptides on either C- or N-termini to the solid support enables the directional control of the applied dipole moment (Figure 1.1). The peptide functionalization was first performed on bulk GaN electrodes. After systematic structural characterization of the formed peptide layers, grafting protocols were transferred to GaN/AlGaN/GaN transistors, in order to investigate and quantify the impact of the macro molecular dipole moment on the electrochemical properties of GaN and GaN heterostructures.

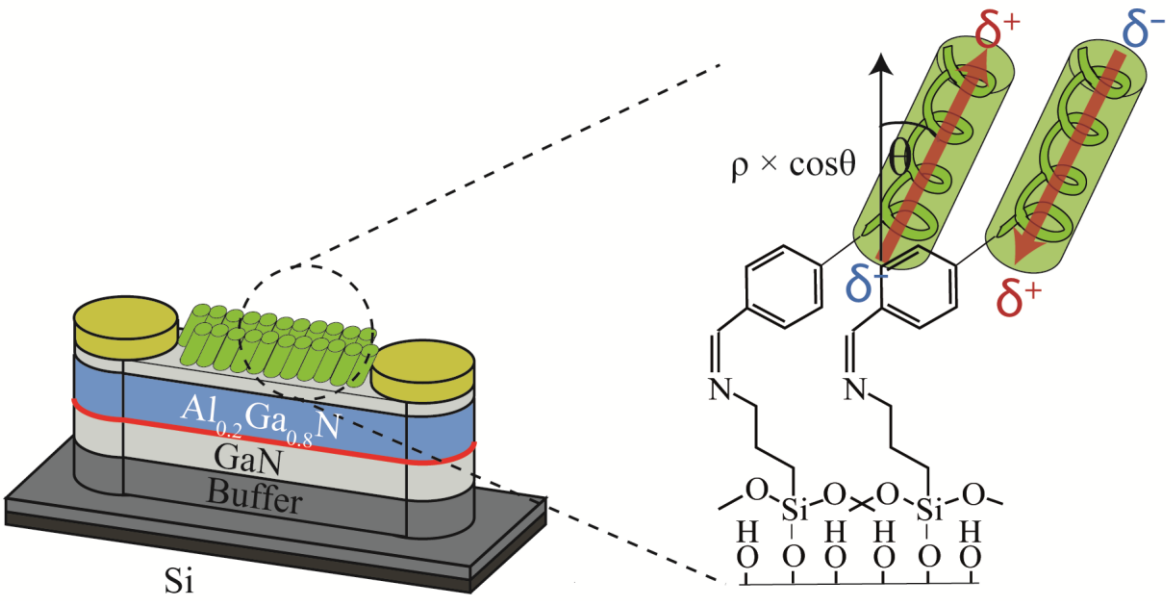

Figure 1.1: *Schematic representations of the aminosilanized and helical peptide grafted GaN/AlGaN/GaN heterostructures. The arrows indicate the possible orientations of the peptide dipole moment.*

In Chapter 5.1, a hybrid sensor system for the electronic detection of the binding/unbinding of recombinant proteins to membrane surfaces was investigated by the functionalization of GaN/AlGaN/GAN heterostructure (in collaboration with Prof. Dr. M. Eickhoff, Univ. Bremen) surfaces with supported lipid membranes. In order to demonstrate the potential of this multilayer system for the electronic detection of the protein binding/unbinding, nitrilotriaceticacid (NTA) chelator lipids were incorporated into the supported lipid monolayer. These lipids allow the formation of charged chelator complexes with divalent metal ions and the reversible coupling of histidine tagged recombinant proteins (Figure 1.2a) onto the lipid monolayer. Changes in the surface potential at the membrane interface, caused by reversible chemical/biochemical protein binding were then investigated by the changes in current-voltage (*I-V*) characteristics of GaN/AlGaN/GaN HEMTs.

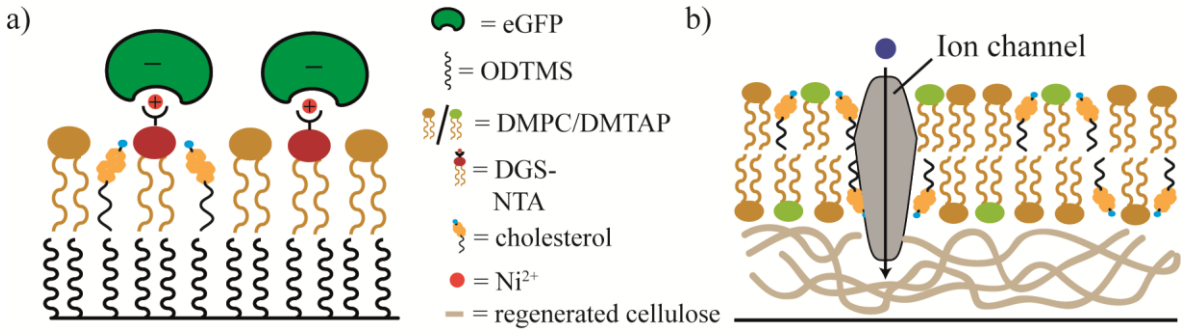

Figure 1.2: *Schematic representation of (a) reversible couping of charged proteins on supported monolayer membrane containing NTA chelator lipids and (b) polymer supported lipid bilayer membrane for the incorporation of intermembrane proteins, such as ion channels, under non-denaturating conditions.*

Additionally, Chapter 5.2, details the immobilization of biological membrane models on soft polymer supports of hydrated cellulose on GaN/AlGaN/GaN HEMT devices (Figure 1.2b). Here ultrathin polymer "*cushions*" (Wegner 1992 and 1993, Sackmann 1996) of cellulose are used to separate soft membrane model systems and reduce their interaction with the rigid surface of the sensor platform. These cushions provide a bioanalogous environment for membrane proteins, creating hydration pathways and enabling the incorporation of integral proteins without denaturation (Hillebrandt et al. 1999). Membranes exhibit similar fluidity and self healing properties to biological membranes on such soft polymer interfaces (Rädler 1995, Nissen 1999) reducing defects in the membrane. Thus high electrical resistance in these membranes can be achieved, allowing for a high sensitivity to the functions of the membrane and integral proteins (e.g. ion channels) (Hillebrandt et al. 1999). Here, the influence of such membrane systems on electronic properties of GaN heterostructures is analyzed by the change in *I-V* characteristics of GaN/AlGaN/GaN HEMTs.

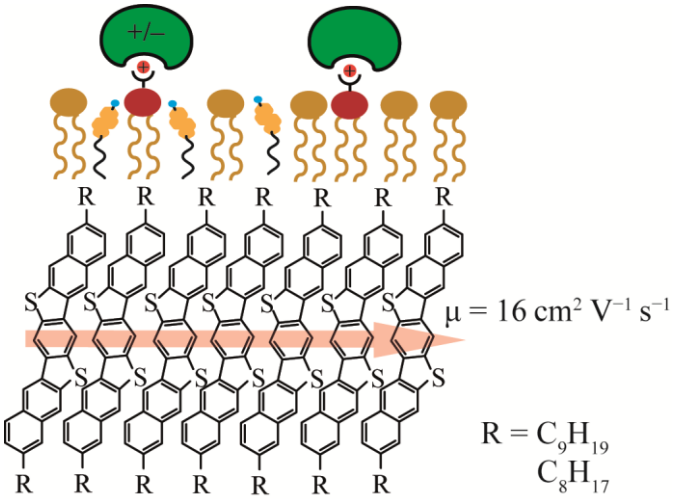

Figure 1.3: *Schematic representation of anchored recombinant proteins on the organic semiconductor (DNBDT) film.*

In Chapter 6 the same approach detailed in Chapter 5.2 was applied to a single crystalline film of an organic semiconductor material developed by the group of Okamoto and Takeya et al. (Mitsui, Okamoto et al. 2014, Makita et al. 2017). The provided semiconductor material Dinaphtho[2,3-d:2′,3′-d′]benzo[1,2-b:4,5-b’] dithiophene (DNBDT) is used as a support for membrane systems towards the fabrication of novel organic field effect transistor (OFET) biosensors using the flexibility and low cost of OFETs (in collaboration with Prof. Dr. T. Okamoto and Prof. Dr. J. Takeya, Univ. Tokyo). This structure self-assembles into a single crystal film forming π-stacks from its N-shaped π-core system (Figure 1.3) (Mitsui, Okamoto et al. 2014) and expresses outstanding carrier mobility and low threshold voltage. This makes this material a very promising candidate for the exploration of biosensor applications of supported membrane models on organic semiconductor materials. In this Chaper the lipid monolayer formation on these materials is detailed. The operation of these materials is furthermore investigated under aqueous buffer conditions, marking this work as one of the first times such a single crystalline OFET is operated under water. The details of the obtained results are described in the following sections.

2. Materials and Methods

2.1 Materials

2.1.1 Chemicals

Cholesterol and 1,2-dioleoyl- *sn* -glycero-3-[(*N* -(5-amino-1-carboxy-pentyl)iminodiacetic acid)succinyl] (nickel salt) (DGS-NTA(Ni)), 1,2-dioleoyl-*sn*-glycero-3-phosphocholine (DOPC), 1,2-dimyristoyl-sn-glycero-3-phosphocholine (DMPC) and 1,2-dimyristoyl-3-trimethylammonium-propane (chloride salt) (DMTAP) were purchased from Avanti Polar Lipids (Alabaster, USA). The expression and prurification of his-tagged GFP from E.coli is described elsewhere (Frenkel 2014). His-tagged ds-Red protein monomers were purchased from Biovision (Milpitas, USA). Unless stated otherwise, all other chemicals were purchased from Sigma Aldrich (Steinheim, Germany) and used without further purification. Ultrapure water (Millipore, Molsheim, France) with a resistivity of 18.2 MΩcm was used in all experiments. Standard HEPES buffer contained 10 mM HEPES, 150 mM NaCl at pH 7.5. For Ca- and Ni- buffers additional 2 mM $NiCl_2$ or $CaCl_2$ respectively were added. For peptide coated GaN experiments (Chapter 4) a HEPES buffer containing 10 mM HEPES and 100 mM NaCl at pH 7.0 was used.

2.1.2 Substrates

Native oxide Si (100) substrates used for AFM and X-ray reflection experiments and thermal oxide Si (100) with an oxide layer of 150 nm used for ellipsometry were purchased from Si-Mat (Landsberg/Lech, Germany). Glass cover slips made from borosilicate glass (Menzel GmbH, Braunschweig, Germany) with a diameter of 32 mm and thickness of 0.17 ± 1 mm were used for Fluorescence microscopy and FRAP experiments.

GaN films were grown on c-plane sapphire substrates (330 µm) with a total thickness of 3 µm (first 300 nm low temperature undoped GaN buffer, then 2.7 µm C-compensated GaN) by metal organic chemical vapor deposition (MOCVD). GaN wafers were cleaved into 5 × 5 mm^2 pieces for AFM, XPS, and XRR. For Electrochemical Impedance Spectroscopy and Cyclic Voltammetry, a 210 nm thick Ge doped (N_D = 1 × 10^{20} cm^{-3}) GaN film was deposited on an undoped GaN templates by MOCVD (Fritze 2012). The high donor concentration ensures a sufficiently high semiconductor space charge capacitance for electrochemical sensing. High-electron-mobility-transistor (HEMT) heterostructures (GaN/$Al_{0.25}Ga_{0.75}N$ (20 nm)/GaN) grown on Si(111) substrates by

MOCVD (Figure 2) were generous gifts from Fujitsu Ltd. (Kawasaki, Japan). The sheet carrier density and the carrier mobility of the two-dimensional electron gas (2DEG) were determined to (8.3 ± 0.1) x 10^{12} cm^{-2} and (1781 ± 5) $cm^2 \cdot V^{-1} \cdot s^{-1}$ at room temperature from Hall-effect measurements. Organic C8-DNBDT transistors were a generous gift from Prof. Dr. T. Okamoto Group (Tokyo University). The organic semiconductor phase was drop cast onto Si (100) and cover slip substrates.

2.1.3 Chemical Coupling of Peptides

The three formyl-terminated peptides used in this study (F8OMe, Boc8F, and Fc8F) were previously synthesized (Frenkel 2015, Mehlhose and Frenkel 2018) and are shown in Figure 1. The peptides are built with repeated units of leucine (Leu) and aminoisobutyric acid (Aib) and form stable α-helix (Fujita, Kimura et al 1995, Miura, Kimura et al 1998) and are coupled to the surface from either the N-terminus (F8OMe, FcF8) or from the C-terminus (Boc8F).

Prior to surface functionalization, GaN and HEMT substrates were cleaned in a 3:1 H_2SO_4:H_2O_2 solution for 15 min, rendering the surface hydrophilic and terminated with hydroxyl groups. After thorough rinsing with water the samples were dried under N_2 stream, and treated by an UV-Ozone cleaner (ProCleaner™, BioForce Nanosciences, Wetzlar, Germany) for 20 min. The hydrophilic GaN samples were immersed into a solution of aminopropyltriethoxysilane (APTES, 20 mM) in dry toluene. After the condensation reaction at 50 °C for 10 min, the samples were rinsed in toluene, methanol, and acetic acid to remove the residual amount of physisorbed silane molecules. Afterwards they were dried under N_2 stream and stored in vacuum. The coupling of the formyl-terminated peptides to the primary amine of APTES was performed by reflux of the APTES coated sample in the peptide solution in $CHCl_3$ ($c = 0.2$ mM) overnight, rinsing with in $CHCl_3$, and drying under N_2 stream.

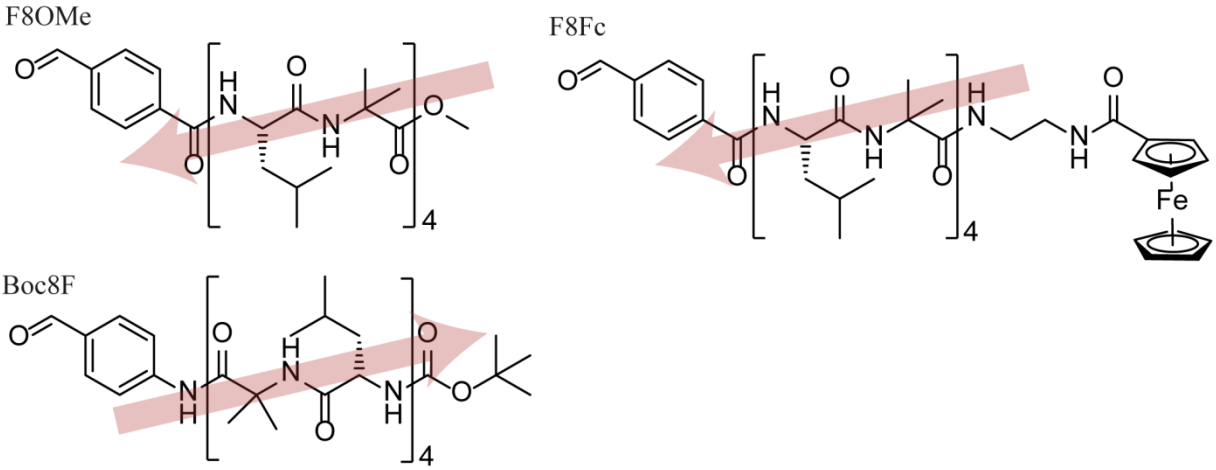

Figure 2.1: *Chemical structures of the three peptides used in this study and the schematic representation of the direction of their projected macromolecular dipole moment (red).*

2.1.4 Substrate Coating with Octadecyltrimethoxysilane (ODTMS)

GaN/AlGaN/GaN HEMT structures, Si or glass substrates were coated with octadecyl-trimethoxysilane (ODTMS) in order to achieve hydrophobic surfaces for lipid monolayer deposition (Mooney et al. 1996, Baur, Howgate et al. 2006, Howgate, Schoell et al. 2010). Before functionalization, the substrates were cleaned by immersion in 3:1 H_2SO_4: H_2O_2 solution for 5 minutes followed by thorough rinsing with water and drying under N_2 stream. The freshly cleaned substrates were then silanized, using an ice-cooled (T = 0 °C) solution of 5% (v/v) solution of ODTMS in water-free toluene with 0.5% (v/v) butylamine as catalyst (Brzoska et al. 1992). In contrast to previous repots (Baur, Howgate et al. 2006, Frenkel 2014) the substrates were incubated for 90 min without sonication at T = 0 °C in order to minimize damage to the ohmic contacts. After rinsing with isopropanol the substrates were dried at 70 °C and stored in a vacuum chamber. Static contact angle of each ODTMS monolayer was evaluated to be beyond 90°, to confirm that the GaN surface was hydrophobic enough for the deposition of a lipid monolayer.

2.1.5 Synthesis of Trimethylsilylcellulose (TMSC)

Microcrystalline cellulose (0.5 g) was dried under nitrogen atmosphere for 2 h at 105 °C. The dried cellulose was suspended in dimethylacetamide (DMAc) (20 ml, anhydr.) and continued to stir 1 h at 150 °C under nitrogen atmosphere. The suspension was left to cool down to 100 °C and LiCl was added (1.5 g). After 5 min further stirring the suspension was left to cool to room temperature and turned transparent. Hexamethyldisilazane (HDMS) (2 ml) was stepwise added over 1 h at 80 °C and the solution becomes turbid. The solution was then centrifuged at 3040 rpm for 20 min and the yellowish solvent

removed. The gel phase was washed with MeOH. The resulting white solid was dissolved in THF and recrystallized with MeOH. A yield of 0.34 g TMSC was achieved.

2.1.6 TMSC coating of substrates

Prior to the coating of the substrates they were cleaned by immersion in 3:1 H_2SO_4: H_2O_2 solution for 5 minutes. Afterwards the substrates were rinsed extensively with water and dried under N_2 stream. A solution of 4 g/L TMSC in Toluene was spun on a Delta 10 spin coater (BLE Laboratory Equipment GmbH, Radolfzell am Bodensee) for 30 s at 4000rpm on a freshly cleaned Si, glass or HEMT substrate. To regenerate the cellulose from TMSC the samples were exposed to HCl vapor and rinsed with water. A dry film thickness of ~ 5 nm is achieved. Film thickness and roughness were determined by Ellipsometry, AFM and XRR.

2.1.7 Lipid membrane Preparation

Stock solutions of DOPC or DMPC and DMTAP in $CHCl_3$ (25 mg/mL) were mixed with cholesterol in various molar fractions for use in bilayer studies. Molar fractions of 40/20/40 % or 65/0/35 % of DOPC/DMTAP/cholesterol or DMPC/DMTAP/cholesterol were used respectively. For fluorescence experiments 0.2 mol% Texas-Red-DHPE was added to this mixture.

Vesicle fusion protocol

After evaporation of $CHCl_3$ under a gentle nitrogen stream and storage under vacuum overnight, the lipids were suspended in HEPES buffer (150 mM NaCl, 10 mM Hepes, pH 7.5) to a concentration of 2 mg/ml and sonicated with a titanium microtip sonicator S3000 (Misonix Inc., Farmingdale, USA) for 10 min to obtain small unilamellar vesicles (SUVs). To remove any residual titanium particles, vesicle suspensions were centrifuged (Eppendorf, Hamburg, Germany) for 10 min at 13400g.

Cellulose and solid supported membranes were prepared by vesicle fusion (Sackmann 1996). SUV suspensions were injected into a flow chamber containing the sample substrate and incubated at 40°C, followed by rinsing with HEPES buffer (150 mM NaCl, 10 mM Hepes, pH 7.5) to remove excess SUVs.

Solvent exchange protocol

As a second method for the deposition of lipid bilayers onto cellulose coated surfaces the dried lipid mixtures were suspended in 50 % Isopropanol and 50 % HEPES buffer. This suspension was injected into a flow chamber containing the sample substrate and in intervals of 15 minutes the buffer content of the solution was increased by 5 % up to a final buffer content of 90% (Hohner 2010). After 30 minutes at the final concentration the substrate was rinsed with HEPES buffer.

2.2 Methods

2.2.1 Atomic Force Microscopy (AFM)

Principle of the Technique

The Atomic Force Microscopy (AFM) is a versatile technique for the study of samples at nanoscale. The detection of attractive or repulsive forces, such as van der Waals, dipole-dipole, electrostatic and magnetic forces, between sample and probe, allows the determination of mechanical properties and the 3-D topography of a surface (Binnig; Quate 1986). Resolution and sensitivity of the measurement are greatly limited by the design, geometry and coating of the sensing probe, the so called cantilever.

A schematic setup is shown in Figure 2.1. The spring-like cantilever with a sharp tip is positioned over the sample. A piezoelement enables z-plane movement and oscillation for the cantilever. For movement in xy-plane the sample is mounted on another piezomotor. Interactions of the cantilever with the sample result in its deflection. With a laser reflected on the back of the cantilever this deflection is measured on a photodiode as a change in photocurrent.

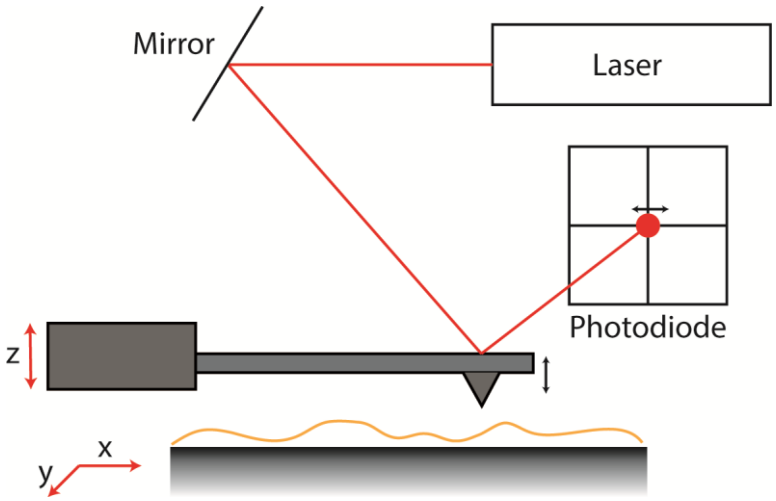

Figure 2.1: *Schematic setup of the AFM showing the delection pathway of the laser on the cantilever.*

The AFM can be used in three modalities: force measurement, manipulation, and imaging.

In force measurement the interaction forces between the sample and the cantilever probe are measured in terms of their spatial separation. This is used for the determination of the

mechanical and electrical properties of the sample, such as stiffness, adhesion strength, conductivity and surface potential.

For manipulation mode, the cantilever probe can be used for the creation of artificial surface structures on a nanometer scale (Lieber 1993). Controlled atomic manipulation with interaction forces between probe and sample are used in techniques like scanning probe lithography.

In imaging mode the deflection of the cantilever imposed by the interaction with the sample can be used to record the 3D-topography of the sample. The sample is raster scanned along the x-y-plane, while employing either a constant height or force between probe and sample with an electronic feedback loop. To characterize the topography the root-mean square (rms) roughness can be used as a measure of the surface smoothness. The rms roughness is described as the average height deviation from the mean height value:

$$rms = \sqrt{\frac{\sum_i (z_i - \bar{z}^2)}{N}} \tag{2.1}$$

Where z_i is the sampling point height, $\bar{z}$ the mean height, and N the number of recorded data points.

Approaching the surface with the cantilever attractive forces dominate at first, with repulsive forces becoming larger at the point of contact. With this, different imaging modes can be realized: (i) contact mode, (ii) non-contact mode, (iii) tapping or intermittent contact mode.

In contact mode the surface profile is gained directly from the deformation of the cantilever pressing on the surface with a certain force. To gain a large signal from the cantilever deformation and to avoid damage to the sample, low stiffness cantilevers that have a low spring constant k are needed. Since this mode is prone to noise and drift intermittent contact mode is more commonly used (Zhong 1993). In non-contact mode is kept at a certain height above the sample, where changes in the height profile reduce/increase the attractive forces between sample and probe and thus cause changes in the cantilever deflection. For intermittent contact mode the cantilever is oscillated near its resonance frequency. The cantilever is in contact with the sample only at the bottom of its amplitude. Near the sample, interaction forces between surface and cantilever cause its oscillation to change. By keeping the oscillation frequency and amplitude constant with and electronic feedback loop the changes in the amplitude can be translated into height differences in the sample. For a stable oscillation stiffer cantilevers compared to contact

mode are used. In general intermittent contact mode caused less damage to the surface, since forces on the surface are only applied for a short duration and lateral forces are significantly lower.

Protocols

Measurements for were performed on glass or silicon substrates with a JPK Nanowizard 3 (JPK Instruments AG, Berlin, Germany). For measurements in contact mode SNL-10 cantilevers with a spring constant of k = 0.35 N/m and a tip radius of 12 nm (Bruker, Karlsruhe, Germany) were used. NCHV-A cantilevers (Bruker, Karlsruhe, Germany) with a spring constant of 42 N/m and a tip radius of 8 nm were used for intermittent contact mode measurements. The scanning speed was 0.3 Hz for scan areas of 10 × 10 μm^2. The images were subjected to a plane correction procedure. Thickness estimation of the grafted peptide, cellulose or other organic layer was done by scratching the surface using RTESPA cantilevers with a spring constant of k = 5 N/m (Bruker, Karlsruhe, Germany) in contact mode in an area of 0.5 × 0.5 μm^2 at F = 1 µN. After the scratching, the topographic profile of an area of 1.5 × 1.5 μm^2 was recorded with using the same cantilever at F = 31.6 nN.

2.2.2 Ellipsometry

Principle of the Technique

Using the change in polarization of light upon reflection Ellipsometry is used for the non-destructive, non-contact investigation of thin multilayer structures. The ellipsometer is used in the PCSA-configuration where the laser beam passes a polarizer, compensator, sample and analyzer in sequence before its intensity is measured in a detector afterwards.

The monochromatic light from the source is linearly polarized by the polarizer. The compensator, usually a λ/4 plate, imposes a defined phase retardation on either the perpendicular (s) or the parallel (p) oriented part of the beam. After reflection on the sample under an angle φ the analyzer determines the changed polarization. In Nullellipsometry the reflected linear polarized light is recorded at the state where the analyzer completely cancels out its polarization and the intensity at the detector is zero.

Hitting the surface the laser beam is reflected and its polarization is changed after passing layers of optical active materials depending on the refractive indices and thicknesses of each layer. The light polarization is represented by two parameters, the ellipsometric angles Δ and Ψ, which are given by the complex reflection coefficients R_s (*s*-polarized light, perpendicular oriented) and R_p (*p*-polarized light, parallel oriented):

$$\tan(\Psi) \cdot e^{i\Delta} = \frac{R_p}{R_s} \quad (2.2)$$

where $tan(\Psi)$ is the amplitude ratio upon reflection and Δ is the phase shift. From these two abstact parameters the material characteristics of thickness *d* and refractive index *n* of each passed layer can be gained through model fitting. As a prerequisite for the measurement samples with well defined, homogeneous layers and low interfacial roughness are needed. Since no further sample preparation is needed, Ellipsometry allows fast data acquisition of solid as well as liquid thin films while high spatial resolutions in the Angstrom range are achieved. (Fujiwara 2007).

Measurement Protocol

All Elliplometry measurements were performed on thermal oxide Si-wafers (Si-Mat, Kaufering, Germany) with an oxide layer thickness *d* of ~ 144 nm. An Optrel Multiskop (Sinzing, Germany) was used with a wavelength of λ = 632.8 nm at an incident angle of 70°. The data was fitted using a self-written script based on IGOR Pro (Wavemetrics, USA).

2.2.3 Contact Angle

Principle of the Technique

Contact angle is a tool used to describe the wettability of a solid surface via the determination of the angle between the contact line of the solid/liquid and liquid/vapor interface. Each system has a unique equilibrium contact angle at a given pressure and temperature defined by the properties of the solid (S), liquid (L) and vapor (V) phase. The equilibrium contact angle is taken at the state of thermodynamic equilibrium and reflects the strength of molecular interaction at the solid, liquid, vapor interfaces. Molecules at the interface between two phases possess different potential energies to those inside the bulk material. The presence of different neighbors to the bulk forces a change in coordination number, resulting in surface tension and the difference in the interfacial energy γ.

The interfacial energy is given by the change in free energy upon creation of a new surface area:

$$\gamma_i = \left(\frac{\partial G}{\partial A}\right)_{PT} \quad (2.3)$$

With the minimization of the free energy *G* per surface area *A* in equilibrium:

$$dG = \sum_i \gamma_i \, dA_i = 0 \quad (2.4)$$

The change in interfacial area by the droplet is given by:

$$dA_{SL} = dA_{SV} = \cos(\theta) dA_{LV} \tag{2.5}$$

With this the free energy is obtained by:

$$dG = (\gamma_{SV} - (\gamma_{LV} \cos(\theta) + \gamma_{SL}))) dA_{SL} \tag{2.6}$$

In the equilibrium state the contact angle is then only dependent on the interfacial energies given by the Young Equation:

$$\gamma_{SV} - \gamma_{SL} - \gamma_{LV} cos\theta_C = 0 \tag{2.7}$$

Where γ_{SV} is the interfacial energy between the solid and the vapor, γ_{SL} the interfacial energy between the solid and the liquid and γ_{LV} is the interfacial energy between the liquid and the vapor. As described in Figure 2.2 θ_C is the equilibrium contact angle (Tadmor 2004).

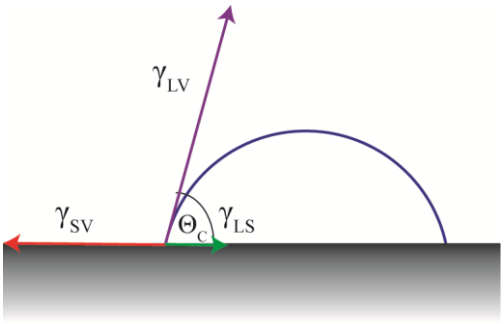

Figure 2.2: *Schematic representation of the solid-liquid (SL), solid-vapor (SV) and liquid-vapor (LV) interfaces formed by a droplet on a surface.*

The equilibrium contact angle is subject to hysteresis in form an advancing and receding contact angle, which describes the maximum and minimum contact angle respectively. Removal or addition of a small amount of liquid to an already deposited droplet causes a de- or increase in the contact angle, while the contact line remains pinned. From this observation the advancing (θ_A) and receding (θ_R) contact angles are derived and the hysteresis as θ_A θ_R. For a perfectly flat surface the equilibrium contact angle θ_C can be calculated by:

$$\theta_C = arccos\left(\frac{\Gamma_A cos\theta_A + \Gamma cos\theta_R}{\Gamma_A + \Gamma_R}\right) \tag{2.8}$$

With $\Gamma_A = \left(\frac{sin^3\theta_A}{2-3cos\theta_A+cos^3\theta_A}\right)^{1/3}$, $\Gamma_R = \left(\frac{sin^3\theta_R}{2-3cos\theta_R+cos^3\theta_R}\right)^{1/3}$ (2.9)

Where θ_A and θ_R are the advancing and receding contact angles (Tadmor 2004, Chibowski 2008).

The contact angle is also influenced by the interfacial roughness of a surface. It is found that the wettability expressed by the surface is enhanced with added roughness if the surface is homogeneously covered by the liquid. As described by the Wenzel equation a hydrophobic surface would become more hydrophobic with additional roughness:

$$cos\theta_m = r\, cos\theta_C \quad (2.10)$$

Where θ_m is the measured contact angle, θ_C is the contact angle and r is the roughness ratio between the actual and projected solid surface area, describing the additional surface area contributed by the texture. Influences on the surface wetting were fond for micro as well as nano scale roughness (Wenzel 1936).

If the liquid does not penetrate into the grooves of a rough surface the measured contact angle is described by the Cassie-Baxter equation, giving the contact angle for a heterogeneous surface with two different materials (Cassie; Baxter 1944):

$$cos\theta_m = x_1 cos\theta_{C1} + x_2 cos\theta_{C2} \quad (2.11)$$

With x_1 and x_2 as the area fraction of the two different materials. If the second material is air the equation can be written as:

$$cos\theta_m = x_1(cos\theta_c + 1) - 1 \quad (2.12)$$

Surfaces with contact angles below 90° are considered hydrophilic, whereas for hydrophobic surfaces contact angles over 90° are observed.

Protocols

Static contact angle measurements were performed in this study on an Optrel Multiskop goniometer (Sinzing, Germany) equipped with a back light and a CCD camera to capture the profile of the water droplet. The water droplet volume deposited on the surface was 2 µl at room temperature. Contact angles determined in this fashion are close to the advancing contact angles.

2.2.4 X-ray Photoelectron Spectroscopy (XPS)

Principle of the Technique

X-ray Photoelectron Spectroscopy (XPS) is a quantitative surface analysis technique which gives access to the elemental composition of the surface as well as the bonding states of the elements (Vickerman and Gimore 2009). High energy X-ray beams, most commonly Mg Kα (1253.6 eV) und Al Kα (1486.6 eV), are used to irradiate the sample surface. Energy transfer from the X-ray photon to an electron of surface atoms causes photoemission of electrons with a defined kinetic energy E_{kin} that is characteristic for a specific element:

$$E_{kin} = hv - E_B - \Phi \tag{2.13}$$

Where E_{kin} is the kinetic energy of the photoelectrons, hv is the X-ray photon energy, Φ is the work function depending on the sample and spectrometer setup and E_B is the binding energy of the corresponding core level electrons.

The electrons can be emitted from the core level as well as occupied valence band states. In Figure 2.3 the electron emission processes are presented.

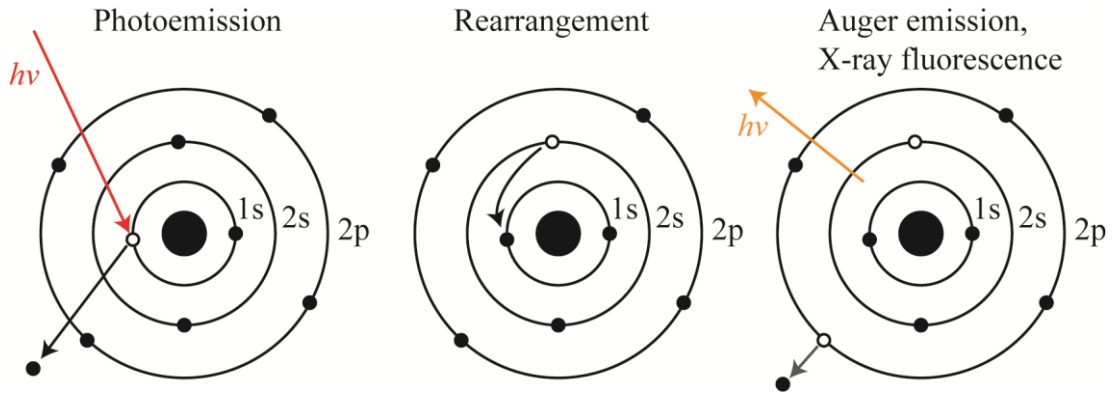

Figure 2.3: *Scheme of the photoelectron emission processes.*

The first process is the photoemission of a core level (1s) electron with the energy $E_{kin} - E_{1s}$, caused by the energy transfer from the X-ray photon. The hole left is then filled by an electron from a higher energy level (2s). This process is called rearrangement. Excess energy $E_{1s} - E_{2s}$ left from this process allows for either emission of an X-ray photon with lower energy than the source beam (X-Ray fluorescence) or the emission of an electron from an energetically higher level (e.g. 2p) (Auger electrons). The characteristic kinetic energy of such Auger electrons is:

$$E_{kin} = E_{1s} - E_{2p} - E_{inter}(2s2p) - \Phi + E_R \quad (2.14)$$

Where E_{inter}(2s2p) is the interaction energy between the 2s and 2p energy levels and E_R is the relaxation energy of the intra- and inter-atomic processes.

The binding energy of an element can differ depending on its chemical environment. This so called chemical shift depends on the degree of electron bond polarization between nearest neighbor atoms, since the core binding energies are determined by electrostatic interaction between core electrons and nucleus, and by the electrostatic shielding of the nuclear charge from all other electrons in the atom.

For an accurate detection of the emitted photoelectrons the XPS must be operated under ultra high vacuum (UHV) conditions ($p < 10^{-9}$ mbar $< 10^{-7}$ mbar) since the electron counting detectors are usually one meter away from the sample. The intensity of photoelectrons detected from the surface of the sample is much stronger than from atoms below the surface, since emitted photoelectrons can undergo inelastic collisions, recombination and excitation of the sample. This causes an exponential attenuation of the photoelectron intensity according to Lambert-Beer law:

$$I_S = I_0 e^{-d/\lambda} \quad (2.15)$$

Where I_0 is the photoelectron intensity emitted at depth d, I_S is the intensity at the surface and λ is the attenuation length.

Since the recorded signal is strongly surface weighted, this can be exploited to estimate the depth of the measured element in layered samples. The sampling depth of the XPS is not dependent of the X-ray penetration depth (1-10 μm) but rather on the inelastic mean free path of an electron λ_e in a solid. Only electrons that can leave the surface without energy loss contribute to a sharp peak of the element specific kinetic energy. Electrons that lost energy before escaping the surface contribute to the background intensity. Characteristic peaks seen in XPS spectra correspond to the electron configuration of the electrons in the element. The intensity is related to the amount of the specific element in the volume sampled by the X-ray beam. Atomic percentages can be gathered from normalized intensities of each detected element, excluding Hydrogen and Helium, which cannot be detected.

Protocols

XPS measurements were carried out under UHV conditions (5×10^{-9} mbar) with a MAX200 spectrometer (Leybold-Heraeus, Cologne, Germany) equipped with an Mg Kα X-ray source (1253.6 eV, 200 W) and a hemispherical analyzer. The recorded spectra on functionalized GaN substrates were corrected for the spectrometer transmission.

2.2.5 High-Energy Specular X-ray Reflectivity (XRR)

Principle of the Technique

X-rays have become an important tool to probe the structure of matter since the discovery by Röntgen in 1895 (Röntgen 1898). With the total reflection of X-rays on layered, solid substrates with smooth surfaces, reported by Compton in 1923 (Compton 1923), X-Ray Reflectivity becomes a highly surface sensitive technique. By measuring the reflected intensity of a monochromatic X-ray beam in dependence of the angle of incidence α_i the layer thickness, roughness and electron density of single or multilayered samples can be determined (Tolan 1999). Since the index of refraction n of materials is below unity for X-rays, total external reflection is observed at sufficiently low incidence angles. At higher angles of incidence the refection intensity decays steeply, enabling the high surface sensitivity of the technique. While the dependency of the penetration depth on the angle of incidence XRR allows for the investigation of thin films in the range of Ångstroms up to several nanometers, such as polymer films (Russell 1990), biological films and supported membranes (Salditt 2002, Rosetti 2015). The complex refractive index n in the X-ray region is given by:

$$n = 1 - \delta + i\beta \tag{2.16}$$

Where the real part δ describes the interaction strength between material and the X-ray beam and is related to the electron density ρ_e and in turn to the scattering length density (SLD).

$$\delta = \frac{\lambda^2}{2\pi} r_e \rho_e = \frac{\lambda^2}{2\pi} SLD \tag{2.17}$$

With r_e being the classical electron radius and λ the X-ray wavelength. The imaginary part β is related the X-ray attenuation coefficient $1/\mu$ (Tolan 1999, Als-Nielsen 2011):

$$\beta = \frac{\mu\lambda}{4\pi} \tag{2.18}$$

δ values are typically in the range of 10^{-5} - 10^{-6} and for most biological matter β is in the range of 10^{-8}.

Figure 2.4 shows the reflection and refraction of an X-ray beam occurring between two media with the refractive indices n_1 and n_2.

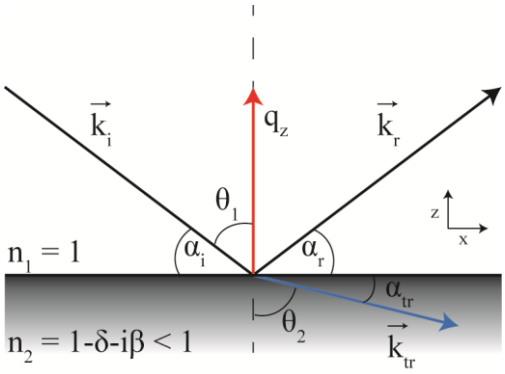

Figure 2.4: *Reflection and refraction of an incident plane wave at a solid, smooth surface.*

Since $n < 1$ for X-rays in most materials, X-rays are refracted away from the surface normal at the air-solid or air water interface. The relationship between angle of incidence α_i and the angle of refraction α_r is given by Snell's law:

$$n_0 \cos \alpha_i = n \cos \alpha_r \tag{2.19}$$

Where the critical angle α_c where only total external reflection is observed for a single vacuum/medium interface is defined as:

$$\alpha_c \approx \sqrt{2\delta} \tag{2.20}$$

For the vacuum-silicon interface $\alpha_c = 0.22°$ at 1.54 Å and for the vacuum-GaN interface $\alpha_c = 0.67°$. Above the critical angle, refraction is occurring as well, leading to an exponential decrease in reflected intensity R. In most cases, reflectivity profiles are given as a function of the reflection wave vector transfer q_z.

$$q_z = \frac{4\pi}{\lambda} \sin \alpha \tag{2.21}$$

The reflection (r) and transmission (tr) of an incident beam (i) on a smooth surface is described by the Fresnel equations (Born 1999). By using Snells law and the Maxwell equations for the propagation of an electromagnetic wave in matter the coefficient of reflection is given by:

$$r(\alpha_i) = \frac{\sin\alpha_i - \sqrt{n^2\cos^2\alpha_i}}{\sin\alpha_i + \sqrt{n^2\cos^2\alpha_i}} \tag{2.22}$$

At small incident angle α_i and in the absence of absorption, the Equation 2.22 can be written as:

$$r(\alpha_i) = \frac{\alpha_i - \sqrt{\alpha_i^2 - \alpha_c^2}}{\alpha_i + \sqrt{\alpha_i^2 - \alpha_c^2}} \tag{2.23}$$

The reflectivity R corresponds to the square of the reflection coefficient. With the absorption of the X-ray beam by the material taken into account the Fresnel reflectivity R_F is given by:

$$R(\alpha_i) = rr^* = \left|\frac{\alpha_i - \sqrt{\alpha_i^2 - \alpha_c^2 - 2i\beta}}{\alpha_i + \sqrt{\alpha_i^2 - \alpha_c^2 - 2i\beta}}\right|^2 = \left|\frac{q_z - \sqrt{q_z^2 - q_c^2 - \frac{32i\pi^2\beta}{\lambda^2}}}{q_z + \sqrt{q_z^2 - q_c^2 - \frac{32i\pi^2\beta}{\lambda^2}}}\right|^2 \tag{2.24}$$

The intensity profile of to the Fresnel reflectivity shows three distinct regions. A plateau region at $0 < q_z < q_c$ where total external reflection of the incident X-ray beam is occurring. At $q_z \geq q_c$, where the incidence angle becomes greater than the critical angle, the reflected intensity decays very rapidly with higher fractions of transmission and refraction occurring. This leads to an asymptotic dependence of R_F at $q_z > 3q_c$. In this regime the reflectivity decreases with $1/q_z^4$ and can be written as:

$$R_F(q_z) = {q_c^4}\Big/{16q_z^4} \tag{2.25}$$

The transmitted intensity in the Fresnel reflection is:

$$T = tt^* = \left|\frac{2\alpha_i}{\alpha_i + \sqrt{\alpha_i^2 - \alpha_c^2 - 2i\beta}}\right|^2 = \left|\frac{2q_z}{q_z + \sqrt{q_z^2 - q_c^2 - \frac{32i\pi^2\beta}{\lambda^2}}}\right|^2 \tag{2.26}$$

With the Fresnel coefficient of the transmission as:

$$t_{j,j+1} = {2k_{j,j}}\Big/{k_{j,j} + k_{j,j+1}} \tag{2.27}$$

These equations are only valid for the reflection on a single smooth layer. To investigate systems with several layers of differing electron densities the mathematical description of the reflection is more complex (Als-Nielsen 2011). The kinematical theory allows the calculation of the reflection on multilayer systems for an arbitrary number of homogeneous layers with sharp interfaces, while it assumes that multiple reflections and refractions are negligible small. The reflectivity is calculated for one layer and added up to the whole multilayer system and depends on the reflectivity for one layer, the average absorption per layer and the layer thickness. This approximation is only valid at higher angles ($q_z > 3q_c$) and for smooth surfaces where the reflection of the X-ray beam is purely specular (in XZ plane). A different approach using the Born approximation to describe the ratio of the reflected intensity and the Fresnel reflectivity as a function of the absolute square of the Fourier transform of the normalized gradient of the electron density across the interface

$$\frac{R(q)}{R_F(q)} = \left| \int_{-\infty}^{\infty} \left(\frac{df}{dz}\right) e^{iqz} dz \right|^2 \tag{2.28}$$

also is only valid for high q ranges and fails to describe the reflectivity near the critical angle (Als-Nielsen 2011).

To improve the description of the intensity profile in small q_z regions Parratt introduced a recursive method using the ratio X_j of the amplitude of the transmitted T_j and reflected X-rays R_j (Parratt 1954).

$$X_j = \frac{R_j}{T_j} = e^{2ik_{z,j}z_j} \frac{r_{j,j+1} + X_{j+1} e^{(-2ik_{z,j+1}z_j)}}{1 + r_{j,j+1} X_{j+1} e^{(-2ik_{z,j+1}z_j)}} \tag{2.29}$$

With the Fresnel coefficient given by:

$$r_{j,j+1} = \frac{k_{j,j} - k_{j,j+1}}{k_{j,j} + k_{j,j+1}} \tag{2.30}$$

The specular reflected intensity R is then obtained by:

$$R = \left| X_j \right|^2 \tag{2.31}$$

With this method multiple reflections at different interfaces and refraction effects are taken into account. The Parratt formalism is the most widely used method to model data for layer structures.

The described models assume smooth interfaces. Real interfaces always have a certain roughness causing a steeper decrease of the reflectivity profile and loss of information due to additional diffusive off-specular reflectivity. The Parratt formalism can be extended to account for the interfacial roughness by introducing an idealized uncorrelated roughness σ, if the relative roughness is small compared to the layer thickness.

The roughness here is used as the mean standard deviation of the layer thickness $\sigma = \sqrt{\langle d^2 \rangle}$. With this the extended Fresnel coefficient is then given by:

$$R = R_F e^{-2\sigma^2 q_z^2} \tag{2.32}$$

Some information on the thickness, electron density and roughness of the sample can directly be determined from the shape of the reflectivity profiles. Figure 2.5 shows the simulated reflectivity profiles for different film thicknesses. With rising film thickness more pronounced minima can be observed in the profiles (green curve). These so-called Kiessing fringes are oscillations from destructive and constructive interference of the reflected beams from two interfaces.

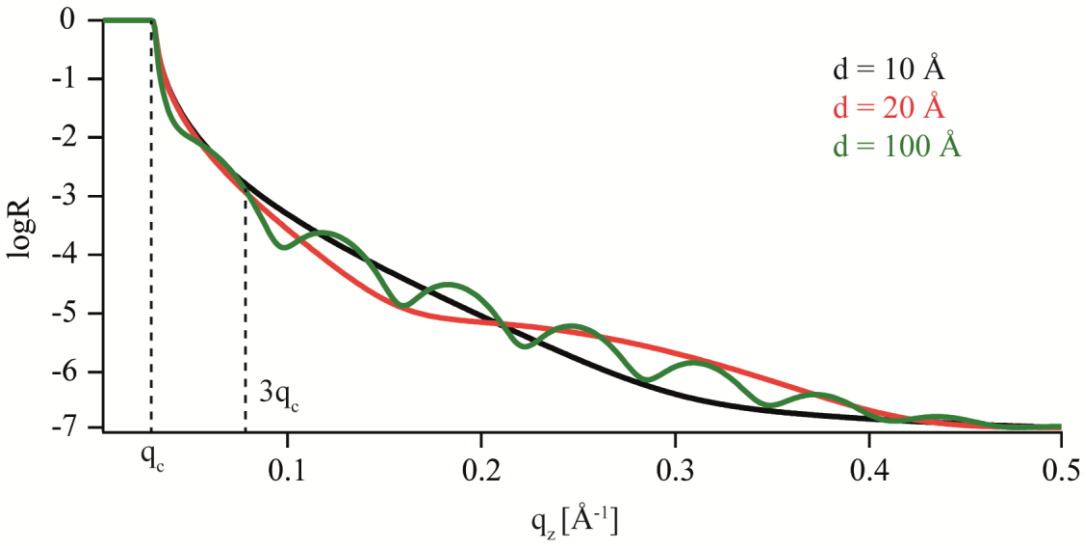

Figure 2.5: *simulated reflectivity profiles for different top layer thickness.*

The thickness d can be estimated from the distance between the minima Δq_z with:

$$d \approx 2\pi/\Delta q_z \tag{2.33}$$

The minimum thickness that can be resolved by XRR is determined by the maximum q_z, which is dependent on the flux and focus of the X-ray beam and the brilliancy of the sample. Additionally the difference in electron density between the film and the substrate

is reflected is the amplitude of the oscillations and the roughness determines the steepness of the intensity decay as given by equation 2.29. To obtain quantitative results from the fitting of the reflectivity data a model representing the experimental system is assumed. For multilayer systems a slab of homogenous electron density ρi, thickness di and roughness σi < di is used for each assumed layer.

Protocols

XRR measurements were performed using a Bruker D8 Diffractometer (Karlsruhe, Germany). Mo K_α radiation (E = 17.48 keV, λ = 0.0709 nm) with a beam size of 200 µm was used for all measurements. Samples measured in aqueous buffer were placed in a Teflon chamber with Kapton windows. The momentum transfer perpendicular to the interface is given as a function of the angle of incidence α_i; $q_z = \frac{4\pi}{\lambda}\sin\alpha_i$. After the subtraction of background and the beam footprint correction, the specular reflectivity was fitted using the Parratt formalism (Parratt 1954, Tolan 1999) implemented in the Motofit software package with a genetic minimization algorithm (Nelson 2006).

2.2.6 Fluorescence Recovery after Photobleaching (FRAP)

Principle of the Technique

FRAP is used to measure the lateral mobility of fluorescent labeled particles (Axelrod *et al.* 1976). It can be employed to determine the Diffusion coefficient D and mobile fraction R in a lipid mono- or bilayer. In order to do this, lipid vesicles of a matrix lipid, mixed with a small molar fraction of a dye-labeled lipid were deposited on the substrate (Merkel *et al.* 1989). A defined area of the substrate is photobleached with a focused, high intensity laser pulse. The recovery of the fluorescence intensity in the bleached area due to lateral diffusion of unbleached fluorophores from the surrounding membrane is then observed (Merkel *et al.* 1989, Sigl *et al.* 1997). This recovery is described by equation 2.31 (Soumpasis 1983):

$$F(t) = F(\infty) - (F_0 - (F(0))\left(1 - e^{-2\tau/t}\left(I_0\left(\frac{2\tau}{t}\right) + I_1\left(\frac{2\tau}{t}\right)\right)\right) \tag{2.34}$$

where $F(\infty)$ is the equilibrium intensity at the time point t, F_0 is the initial fluorescence intensity *before bleaching,* $F(0)$ is the intensity in the bleach spot at time t = 0 after bleaching, I_0 and I_1 are modified Bessel functions of the zero and first order, respectively and τ is the characteristic time constant. With the assumption of a Gaussian profile of the bleaching beam the lateral diffusion coefficient D can be determined by:

$$D = \frac{r^2}{4\tau} \tag{2.35}$$

With D as the diffusion coefficient, τ as the characteristic time constant and r as the radius of the bleached area at t = 0.

The relative recovery R of the fluorescence, which can be related to the fraction of mobile fluorophores can be given by:

$$R = \frac{F(\infty)-F(0)}{F_0-F(0)} \tag{2.36}$$

In this study, through-the-objective total internal reflection fluorescence (TIRF) microscopy was used for the FRAP measurements. Using a high numerical aperture (*NA*) objective, a laser beam with the excitation wavelength of the fluorophore is shot through the front lens of the objective with a shallow, but greater angle than the angle of total reflection at the sample interface. From the total reflection at the interface a thin (~200 nm) evanescent electromagnetic field, propagating in z-direction into the sample medium, is created. Only in this defined region the excitation of fluorescent labeled molecules and structures can take place, allowing for the study of samples near the surface without the extra-focal blur of usual fluorescence microscopes. The minimum necessary *NA* of the objective depends on the maximum angle of light exiting the objective and is given by:

$$NA = n_1 \sin\alpha \tag{2.37}$$

To achieve total reflection at the interface between one medium (n_1) and another (n_2), one requires that $n_1 > n_2$ and a greater incidence angle than the critical angle of total reflection $\alpha_i > \alpha_c$. With this,

$$n_1 \sin\alpha_i > n_1 \sin\alpha_c = n_2 \tag{2.38}$$

is given and the required *NA* can be determined as $NA \geq n_2$. For samples suspended in aqueous medium, an objective with $NA > 1.33$ is required for TIRF imaging.

Protocols

FRAP measurements were carried out on a Nikon Ti2 inverted microscope with H-TIRF module (Nikon Plan Apo VC 60× NA 1.4 oil immersion objective, Hamamatsu C9100–02 EMCCD camera) at the Nikon Imaging Center, Heidelberg University. The bleach spot size was r = 5.75 µm with an illumination wavelength of λ = 561 nm. The data were evaluated according to the procedure described by Soumpasis (Soumpasis 1983). Dyes of Texas-Red-DHPE with a molar fraction of 0.2% were used for cellulose and C8-DNBDT

supported membranes and DS-Red monomers were used to determine protein diffusion on C8-DNBDT surfaces.

All other fluorescence images were taken on Axio Observer Z1 microscope (Zeiss, Oberkochen, Germany) equipped with an oil immersion objective lens (NA 1.25, 63 ×). A monochromatic light from a high-pressure metal halide lamp (λ = 546 nm) was selected with a band-pass filter for the observation of stained membranes.

2.2.7 Impedance Spectroscopy (IS)

Principle of the Technique

Impedance spectroscopy (IS) is an important technique especially in interfacial electrochemistry and material science for the observation of electrochemical processes, like charge transfer processes, dynamics of ionic transport or surface charges (MacDonald and Kenan 1987) at complex electrode/electrolyte interfaces. The IS method provides a fixed measurement setup and the possible automation of the measurement process and as a noninvasive and label-free technique enables the investigation of biophysical systems under its natural environment. Thus IS has gained a growing interest in the field of Biophysics and Biosensing. Systems involving functional proteins, such as ions channels or specific adsorption on lipid membranes which are deposited on solid supported planar electrodes (Stelzle, Weissmuller 1993, Sackmann 1996, Gritsch, Nollert 1998, Sackmann and Tanaka 2000, Tanaka and Sackmann 2005, Frenkel 2014) or on field effect transistors (Rentschler and Fromherz 1998) were investigated by the determination of their electrochemical properties. For such biological systems IS allows an accurate insight into material properties, such as dielectric constants, thickness and diffusion constants, as well as mass transport properties, including the rate of chemical reactions, microstructure and influences on the conductance from the composition of the liquids, ions, membranes or solids involved.

By recording the current response to an applied sinusoidal voltage the frequency dependent impedance $Z(\omega)$ of the system is gained. The analysis of this impedance employs theoretical circuit models composed of equivalent circuit components, which are associated to specific chemical or physical processes occurring at the electrode interface. Using a non-linear curve fitting algorithm, the impedance $Z(\omega)$ values are fitted with the equivalent circuit models to simulate the impedance spectra equivalent to the experimental impedance spectra, allowing one to understand the physical meaning of each component used (MacDonald and Kenan 1987).

The complex impedance $Z(\omega)$, where ω is the angular frequency, can be interpreted as the frequency dependent resistance to an AC voltage. It is defined as the ratio of the Fourier-transform $\hat{U}(\omega)$ of the applied AC voltage $U(t)$, and the Fourier-transform $\hat{I}(\omega)$ of the current response $I(t)$.

$$Z(\omega) = \frac{\hat{U}(\omega)}{\hat{I}(\omega)} \tag{2.39}$$

In cartesian or polar coordinates the complex impedance $Z(\omega)$ can be given as

$$Z(\omega) = Re\big(Z(\omega)\big) + i \cdot Im\big(Z(\omega)\big) = Z_0(\omega)e^{-i\varphi(\omega)} \tag{2.40}$$

Where $i = \sqrt{-1}$ and φ is the phase shift between the applied AC potential and the current response. Impedance spectra $Z(\omega)$ can be obtained in either the time domain or in the frequency domain. In the time domain measurement, also called spectral analysis, the AC perturbing signal is composed of multiple frequencies that are all applied simultaneously (Popkirov and Schindler 1992, Popkirov and Schindler 1993). This technique provides an enhanced time resolution allowing for the investigation of highly dynamic processes, like the opening of membrane ion channels (Wiegand, Sackmann 2000). In the frequency domain used in this study sinusoidal potentials with given frequencies

$$U(\omega) = U_0(\omega)\sin(\omega t) + U_{Bias} \tag{2.41}$$

were applied, while the current response

$$I(\omega) = I_0(\omega)\sin\big(\omega t + \varphi(\omega)\big) \tag{2.42}$$

was simultaneously recorded at the same frequency with a Lock-in amplifier. The impedance spectrum is obtained by a sequential frequency sweep for each separate frequency over the desired frequency range. A high enough perturbation amplitude $U_0(\omega)$ has to be considered to overcome thermodynamic fluctuations, but it should otherwise be small to keep the system in a linear response regime. The resulting impedance spectra were plotted either in polar representation (Bode Plot) or in Cartesian coordinates (Nyquist Plot).

Equivalent Circuits

The physical and electrochemical properties and processes occurring in the studied system are directly associated to particular circuit elements, that compound the idealized electric circuit model used for the analysis. The connection of different circuit elements to an equivalent circuit model follows the first and second Kirchoff law (MacDonald and Kenan 1987). The Impedance $Z(\omega)$ of a serial connection of i circuit elements is the sum of the separate impedances of each element $Z_i(\omega)$

$$Z(\omega) = \sum_i Z_i(\omega) \tag{2.43}$$

while a parallel connection results in the reciprocal sum of each element.

$$\frac{1}{Z} = \sum_i \frac{1}{Z_i} \tag{2.44}$$

The equivalent circuit model usually cannot resolve all processes on the surface and becomes a simplification of the real system. Since the designed circuit models become unambiguous if a large amount of circuit elements are used, only the simplest circuits give a unique description of the experimental data (MacDonald and Kenan 1987). Ideal circuit elements, such as Resistance R and Capacitance C, are often used to make up the equivalent circuit. The Resistance R describes the ohmic behaviour of the electrode interface and includes all events that occur in phase ($\Delta\varphi = 0$) with the applied AC voltage $U(\omega)$ and are independent from the frequency. Thus the resistance contributions to the impedance do not scale with the frequency. The AC-impedance response for the resistance is:

$$\mathrm{Z_R}(\omega) = \mathrm{R} \tag{2.45}$$

Ideal capacitors react to external potentials with charge redistribution. This causes a capacitive current response $i_c(\omega)$ with a phase shift of $-90°$ in regards to the applied AC voltage $U(\omega)$. The resulting impedance response of the capacitor is:

$$Z_C = \frac{1}{i\omega C} \tag{2.46}$$

From this equation one can see, that the capacitor impedance has a strong dependence on the AC frequency, which grows with the power of -1. The capacitance of a planar capacitor is given by:

$$C = \frac{d\sigma}{dV} = \frac{\varepsilon_0 \varepsilon}{d} A \tag{2.47}$$

where ε_0 is the dielectric constant in vacuum, ε the relative dielectric constant of the medium, A the active electrode area and d the distance between the capacitor 'plates'. This planar capacitor model can be used to extract the thickness for systems like organic thin films, membranes or the Helmholz layer on the electrode surface, since their discrete thickness defines the interplate distance of the capacitance.

The current response of the semiconductor/electrolyte system is a sum of faradaic currents $i_{f,}$ occurring across the interface and capacative currents i_c, occurring from charging processes at the semiconductor or electrode interface. Faradaic currents are generated in processes that involve charge transfer between ions in the electrolyte and the semiconductor, but processes such as adsorption and ion diffusion can also contribute to this. As shown in Figure 2.6a these currents occur in parallel in the semiconductor, which leads to a parallel connection of their corresponding impedance elements, the total interface capacitance C_p (i_c) and the resistive element Z_f (i_f) occurring from the faradaic currents, as well.

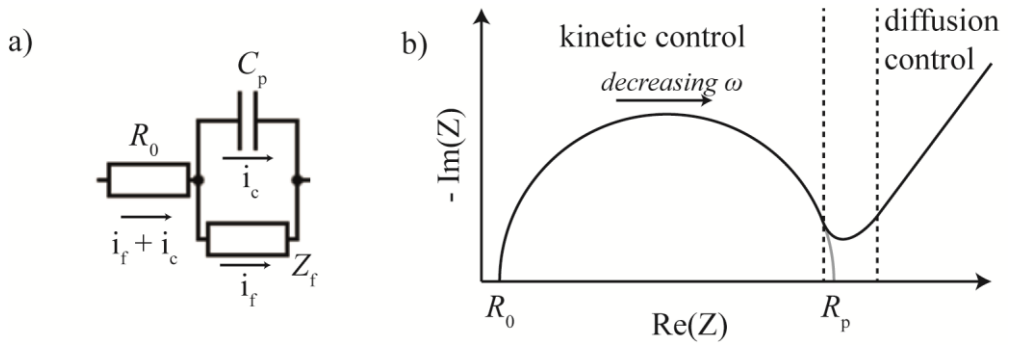

Figure 2.6: *(a) Simplified equivalent circuit model of the electrolyte/electrode interface and the occurrence of faradaic and capacitive currents. R_0 is the electrolyte ohmic resistance, Cp the total interface capacitance resulting from capacitive currents and Z_f is the resistive element attributed to the faradaic currents. (b) Schematic impedance spectrum in Nyquist representation of the simplified equivalent circuit.*

For biophysical systems deviations from the ideal behavior can be caused from structural inhomogeneities, finite permeability and diffusive processes of the system. To account for these contributions distributed elements, such as the Warburg element *W* and the Constant

Phase Element *CPE* are introduced. The Warburg element arises from non-localized processes at the electrode surface. It was first introduced to account for the electron transfer from the bulk electrolyte to the semiconductor (Randles 1947). Later it was demonstrated that the Warburg element could also be used to quantify the diffusion of metals into electrodes (Ho, Raistrick et al. 1980) and ions across thin layers (Finklea, Snider et al. 1993).For diffusively controlled charge transfer processes, the real and imaginary part of the total impedance Z(ω) are equal $-Im\big(Z(\omega)\big) = Re(Z(\omega))$ and the phase shift ϕ becomes −45°. The Warburg impedance is then defined as (MacDonald and Kenan 1987):

$$Z_W \equiv W(\sigma_w) = \left(\sigma_w + \frac{1}{\sigma_w}\right)\omega^{-1/2} \tag{2.48}$$

From the Warburg parameter σ_w the diffusion constant *D* of the ions across the layer can be determined by:

$$\sigma_w = \frac{4RT}{\sqrt{2}n^2F^2A\rho}\,\frac{1}{\sqrt{D}} \tag{2.49}$$

with the active electrode area A, the diffusion constant *D*, the surface ion density ρ. The constants *R*, *T*, *n*, and *F* have their usual meaning as gas constant, absolute temperature, the ion charge of the electrolyte, and Faraday constant respectively. The frequency dependency of the total impedance grows with the power of −0.5 (MacDonald and Kenan 1987), as shown by equation 2.45. Thus with higher frequencies the influence of the Warburg element and in turn the diffusion processes to the total impedance is diminished. In the Nyquist representation of the impedance spectra of the semiconductor/electrolyte system (Figure 2.6b) two regions can be distinguished. In the first region, at high AC frequencies, the spectrum is dominated by kinetically controlled faradaic processes that can be represented by an ohmic resistance *R*. In the second, low frequency region diffusion controlled processes becomes dominant. There the rate of ion adsorption and diffusion to the electrode surface is slower than the rate of charge transfer, limiting the speed of the charge transfer (Sluyters and Oomen 1960). These diffusion controlled faradaic processes are modeled with a Warburg resistance. For non-ideal systems both kinetic and diffusive controlled processes coexist and the resistive element Z_f is then compounded by a serial connection of an Ohmic resistance and a Warburg resistance.

The Constant Phase Element is an empirical impedance element that takes the frequency and non-linear dependencies from inhomogeneities (MacDonald 1994) or surface roughness appearing in real systems into account (de Levie 1989, Lindholm-Sethson 1996).

The impedance response of the *CPE* is given by:

$$Z_{CPE} = K\omega^{-\alpha} \tag{2.50}$$

In ideal systems the *CPE* corresponds to an ideal resistor when the frequency exponent $\alpha = 0$ and $K = R$. When $\alpha = 1$ and $K = 1/C$ the *CPE* acts as an ideal capacitance and for $\alpha = 0.5$ as an ideal Warburg impedance. Inhomogeneities from defects or roughness cause deviations from these ideal values. Although the use of a *CPE* improves the fit quality, the analysis is only of a qualitative manner, since the *CPE* is just an empirical element. In this work impedance spectra were interpreted with the electrochemical equivalent circuit models presented in Figure 2.7a.

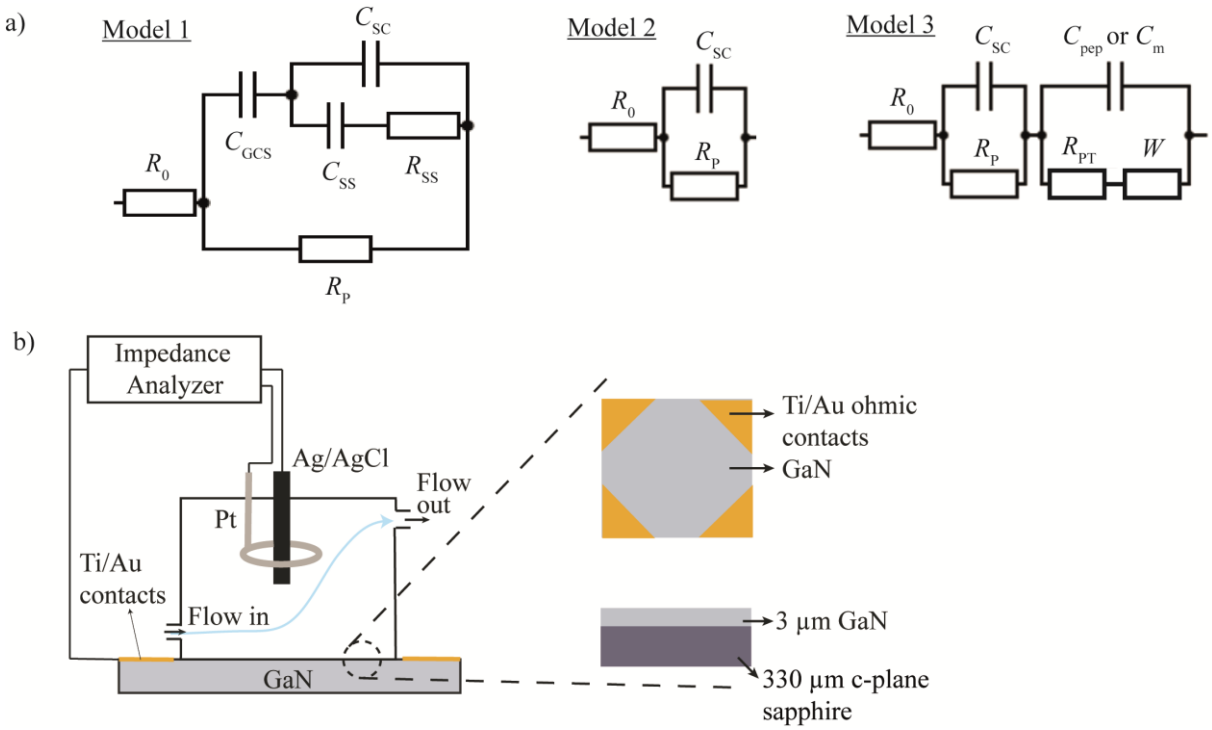

Figure 2.7: *(a) Equivalent circuits used for impedance analysis. Model 1 depicts the general equivalent circuit for the electrolyte-semiconductor interface. R_0 represents the resistance of electrolyte and ohmic contacts, R_P the semiconductor/electrolyte interface resistance, C_{GSC} is the capacitance of the Gouy-Chapman-Stern layer, C_{SS} and R_{SS} are the capacitance and resistance of surface states and C_{SC} the interface capacitance, represented by the space charge capacitance of semiconductor. Model 2 is a simplified equivalent circuit used for the analysis of untreated semiconductor samples. Model 3 includes an additional RC circuit for coated semiconductors including the peptide or membrane capacitance C_{pep} or C_m the Warburg impedance W and phase transfer resistance R_{PT}. (b) Three electrode flow chamber used for electrochemical analysis with*

Pt counter electrode, Ag/AgCl reference electrode and top and side view of the bulk GaN working electrode.

A general representation for the impedance response of the semiconductor/electrolyte interface is described by Allongue and Horowitz and shown in the equivalent circuit Model 1 (Horowitz, Allongue 1984, Allongue 1985). This model includes impedance representations for the resistance of the electrolyte and ohmic contacts R_0, the semiconductor interface resistance R_p and the interface capacitance, as well as resistance and capacitance contributions (R_{SS} and C_{SS}) arising from surface states and defects in the semiconductor. The interface capacitance C_p includes contributions from the capacitance of the Gouy-Chapman-Stern layer C_{GCS} forming at the electrolyte/semiconductor interface and the space-charge capacitance C_{SC} of the semiconductor interface (Bard 1980). The capacitance contribution of the Gouy-Chapman-Stern layer can further be separated into influences from the Helmholtz layer C_H and diffuse ion layer C_{diff}. These contributions usually can be omitted (Aldkofer 2001), since $C_H \geq 140$ μFcm^{-2} and $C_{diff} \geq 0.9$ Fcm^{-2} (Bard 1980) the semiconductor interface is not sensitive enough to changes in these parameters. For capacitances connected in series, the smaller capacitance is dominant and has a stronger influence on the total impedance. Additionally the contributions from surface states, arising from the break in lattice periodicity at the semiconductor surface, can be neglected when the measurement is performed at bias potentials far away from the flat band condition of the semiconductor (Schmuki 1995). There the ratio $C_{SS}/C_{SC} < 0.1$ and the quantitative determination of C_{SS} is not possible (Horowitz, Allongue 1984, Allongue 1985). Using these simplifications the semiconductor/electrolyte interface can be described with Model 2 (Steinhoff, Purrucker 2003), where the semiconductor interface capacitance is mainly dependent on its space-charge capacitance C_{SC}. With Model 3 deposited organic layers or biological membranes on the semiconductor are modeled by an additional Randles cell that includes phase transfer resistance R_{PT}, Warburg element W and capacitance for the peptide layer or lipid membrane used in this work (Randles 1947, Schubert, Steinhoff 2009).

Protocols

Electrochemical measurements were carried out in an electrochemical flow chamber (Figure 2.7b) equipped with the functionalized GaN as working electrode, a Pt counter electrode, and a Ag/AgCl reference electrode (World Precision Instruments, Berlin, Germany). The GaN electrodes with an active area of 0.5 cm^2 were contacted by four copper plates touching the front side corners of the substrate with four Ti (30 nm)/Au (100 nm) Ohmic contacts (Figure 2.6 b). The buffer was continuously pumped through the chamber with a flow rate of 1 ml/min by a peristaltic pump (Perimax, Spetec GmbH,

Erding, Germany) to avoid the formation of dielectric surface layers. The impedance spectra of GaN were measured at frequencies between 100 kHz and 15 mHz with 20 frequencies per decade and with an AC voltage oscillation amplitude of 20 mV. The obtained impedance spectra were fitted using non-linear curve fitting algorithm (Macdonald and Kenan 1987).

2.2.8 Cyclic Voltammetry

Cyclic Voltammetry (CV) is an electrochemical technique providing information on the thermodynamics of redox processes and the kinetics of heterogeneous electron-transfer and redox reactions present in an analyte. CV is performed by cycling a linear voltage sweep between a fixed potential range (Figure 2.8a) and at a fixed rate and measuring the current response of the system. To induce the redox process a larger potential range than predicted by the Nernst equation (Equation 2.51) for the measured redox system is needed.

$$E = E^0 + \frac{RT}{zF} ln \prod_i a_i^{v_i} \tag{2.51}$$

With the standard cell potential E^0, universal gas constant R, temperature T, number of transferred electrons in the reaction z, Faraday constant F and the chemical activity a of the reactants.

Usually CV is performed with a three electrode setup of reference, working and counter electrode (Figure 2.6b), where the potential and current of the working electrode, in this case the sample electrode, is measured against the reference electrode. The reference electrode is maintaining a constant potential in the meantime. (Bard 2000, Wang 2000)

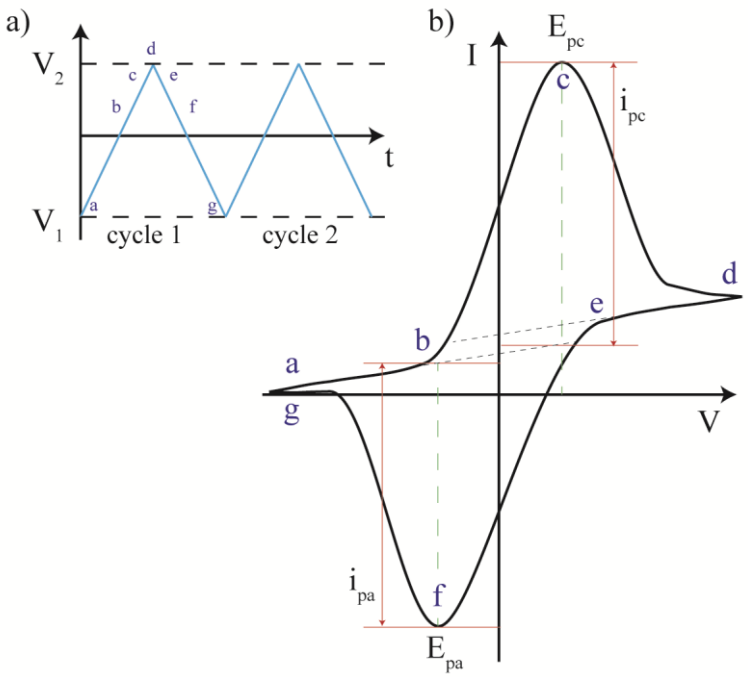

Figure 2.8: *(a) applied voltage profile in CV and (b) the resulting current response from one sweep cycle.*

The potential sweep, depicted in Figure 2.8a, first starts with a negative potential V_1 (a) and is linearly scaled to the so called switching potential V_2 (d), that is sufficient to initiate the redox process in the analyte. Then the reverse scan is performed from V_2 (d) to V_1 (g). In the reverse scan the potential is brought back to the equilibrium position, gradually converting electrolysis product of the forward scan back to the original reactant. The current flow now is opposite to the forward sweep from the solution species back to the working electrode. The resulting current signal of such a potential sweep is depicted in Figure 2.8b. showing a typical reduction peak occurring in the region from (a) to (d) where the potential scans positively and an oxidation peak occurring from (d) to (g) where the potential scans negatively. The resulting current in the forward scan (a-d) is called cathodic current (i_c), with the corresponding cathodic peak potential (E_{pc}) occurring at (c), when the analyte at the working electrode surface has been reduced completely. The reverse scan (d-g) causes an anodic current (i_a) from oxidation until the anodic peak potential (E_{pa}) is reached with complete oxidation at (f). The characteristic CV peaks reflect the formation of the diffusion layer near the electrode surface. The continuous change in the surface concentration at the working electrode induces an expansion of the diffusion layer thickness. Thus, the peak current corresponds to a purely diffusion controlled reaction, while the drop in current after the peak shows a dependence of $t^{-1/2}$, indifferent to the applied potential. With the use of microelectrodes the shape of the

voltammogramm is sinusoidal, since the mass transport process dominated by radial, instead of linear diffusion.

Reversible Systems

The CV of a reversible electrochemical reaction with fast reaction kinetics is defined by several parameters. These include the two peak currents and potentials, which provide the basis for analyzing the CV response developed by Nicholson and Shain (Nicholson 1965). The peak current given for a reversible redox couple at 25°C, is given by the Randles-Sevcik equation:

$$i_p = (2.69 \times 10^5) n^{3/2} A c D^{1/2} v^{1/2} \quad (2.52)$$

with the anodic or cathodic peak current i_p, the number of electrons n, the electrode area A in cm^2, the concentration c in mol/cm^3, the diffusion coefficient D in cm^2/s, and the scan rate v (in V/s). According to this equation the peak current is increases with the square root of the scan rate as shown in Figure 2.9a. With varying scan rates the formation diffusion layer above the electrode is different.

For low scan rates the diffusion layer reaches further from the electrode, while the flux to the electrode is smaller than at faster scan rates. Since the current is proportional to the flux towards the electrode, this causes a decrease in current compared to faster scan rates. Further, the scan rate can be determined from the slope of the anodic and cathodic current peaks.

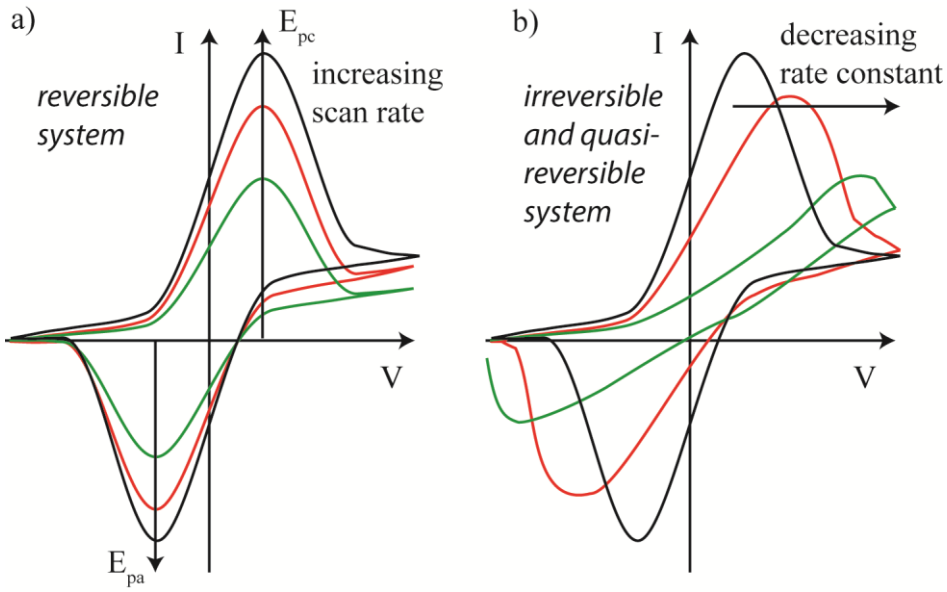

Figure 2.9: *(a) scan rate dependent change in CV spectra for a reversible redox system and (b) change in spectra depending on electron transfer rate for irreversible systems.*

Using the formal potential E^0 from Nernst Equation of the measured redox system, the position of the peak potentials E_p can be determined by:

$$E^0 = (E_{pa} + E_{pc})/2 \tag{2.53}$$

This equation shows that the formal potential for a reversible redox system is centered between E_{pa} and E_{pc}, with the separation between the peak potentials given by:

$$\Delta E_p = E_{pa} - E_{pc} = 59\ mV/n \tag{2.54}$$

With this the number of electrons *n* transferred in the reaction can be calculated from the peak separation. The peak separation can also be used to confirm Nernstian behavior of the redox process, where both the cathodic and anodic peak potentials are independent of the scan rate.

A further criteria for reversible systems is the unity of anodic-to-cathodic peak current ratio (i_{pa}/i_{pc} =1). This ratio is strongly influenced by reactions coupled to the redox process, such as instability of the redox products or irreversible reactions. The magnitudes of the current peaks are determined by extrapolation of the preceding baseline current.

Irreversible and Quasi-reversible Systems

The above conditions only apply when the electron transfer rate in the reaction is high. In case this transfer process is slow in relation to the scan rate the system is not reversible anymore and is referred to as quasi-reversible or irreversible. Figure 2.9b shows voltammogramms for different oxidation and reduction rate constants. In case the oxidation and reduction rate constants are still fast compared to the scan rate (black curve) the voltammogramm is similar to that of a reversible system. As the rate constants decrease a shift towards more reductive potentials is observed. The applied voltage in this case does not generate sufficient concentration of the redox reaction product predicted by the Nernst equation at the electrode surface. Due to the slow reaction kinetics the equilibrium at the electrode surface cannot be rapidly established in comparison to the voltage scan rate. In these cases the peak separation is not constant but varies with the scan rate, since the current takes more time to respond to the applied voltage than in the reversible case, while the change in the peak current is no longer proportional to the square root of the scan rate. For irreversible processes the current peaks are reduced in magnitude with a larger peak separation. The shift of the peak potential for completely irreversible systems is defined by:

$$E_p = E^0 - \left(\frac{RT}{\alpha n_a F}\right)\left(0.78 - \ln\left(\frac{k^0}{D^{\frac{1}{2}}}\right) + \ln\left(\frac{\alpha n_a F}{RT}\right)^{1/2}\right) \tag{2.55}$$

where α is the transfer coefficient, n_a is the number of electrons involved in the charge-transfer step and k^0 the electron transfer rate. From this it is apparent that E_p occurs at higher potentials than E^0, with the overpotential related to k^0 and α. The peak potential will differ by $48/\alpha n$ mV, increasing the peak separation proportionally as αn decreases. From the shift in peak position it is possible to determine the electron transfer rate constants.

The peak current of an irreversible process is then given by:

$$i_p = (2.99 \times 10^5) n (\alpha n_a)^{1/2} A c D^{1/2} v^{1/2} \tag{2.56}$$

Where n is the number of electrons transferred in the reduction, A is the working electrode surface area in cm^2, D is the diffusion coefficient in cm^2/s, v is the scan rate in V/s, and c is the bulk molar concentration in mol/cm^3. The decrease in pear current magnitude depends on α. When $\alpha = 0.5$, the irreversible current peak is about 80 % of the peak in the reversible case. In quasi-reversible systems, when $10^{-1} > k° > 10^{-5}$ cm/s, the current is dependent upon the charge transfer at the electrode as well as the mass

transport. The shape of The CV is then determined by the ratio of $k^0/(\frac{\pi\nu nFD}{RT})^{1/2}$, with an increasingly reversible like behavior as the ratio increases.

Nonfaradaic current

Another current contribution to the CV spectra occurs from of a nonfaradaic current. In contrast to the faradaic current response from the charge transfer at the electrode, the nonfaradaic stems from the charging of the double layer capacitance at the electrode surfaces with changing potentials.

The current response from the nonfaradaic process causes the hysteresis in CV spectra (Figure 2.10a), with the current proportional to the scan rate *v*:

$$i_F = \frac{i_a - i_c}{2} = AC_{dl}\frac{dE}{dt} = \nu AC_{dl} \tag{2.57}$$

with the double-layer capacitance C_{dl} in the equivalent circuit for the ion-double-layer (Figure 2.10b) described by:

$$C_{dl} = \frac{\varepsilon\varepsilon_0 A}{d_{dl}} \tag{2.58}$$

where R_F is the resistance of the Faradaic reaction, R_{cell} the resistance of the solution to the diffusion of ions, d_{dl} the double-layer thickness and A the electrode area.

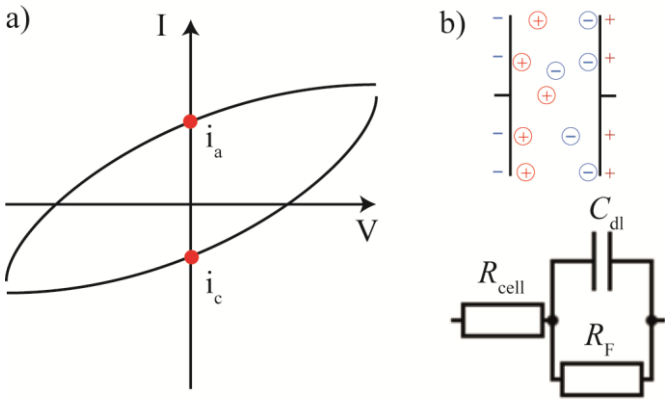

Figure 2.10: *(a) schematic faradaic current response and (b) equivalent circuit for the formation of the ion-double-layer at the electrode surfaces.*

Protocols

Voltammograms of ferrocene terminated peptides were measured in Na_2SO_4 (100 mM) in the potential range between – 1 V and + 1.5 V for 5 cycles and at various scan speeds of 50-120 mV/s. A three electrode electrochemical flow chamber setup under static conditions, as described for impedance measurements was used.

2.2.9 Chronoamperometry

Chronoamperometry is an electrochemical technique investigating the current response over time to a potential step on the working electrode and is used to study kinetics of redox reactions and diffusion processes. Like in cyclic voltammetry a three electrode setup is used for this technique. At first a potential V_0 where no faradaic process occurs is applied to the working electrode (Figure 2.11).

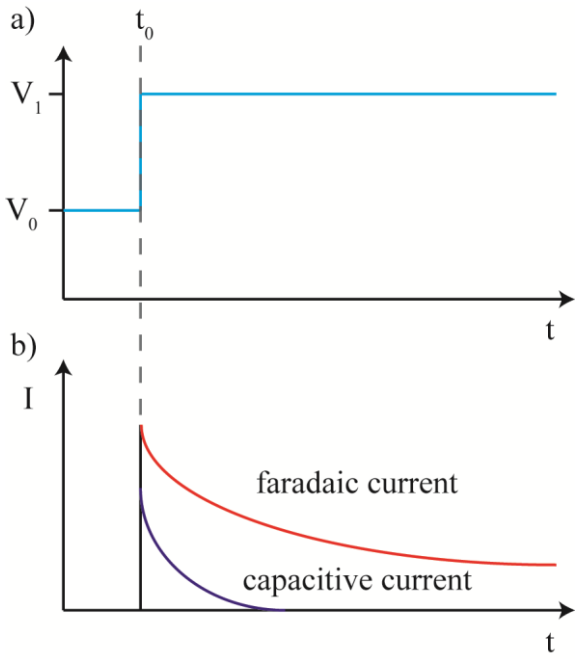

Figure 2.11: *(a) schematic representation of the potential step applied during the measurement and (b) the resulting faradaic and capacitive current response from the occurring electron transfer and double layer charging.*

At $t = t_0$ the potential is stepped to a value V_1 at which electron transfer at the electrode (e.g. the redox reaction of the analyte) can occur. This faradaic reaction at the electrode generates a so called faradaic current response that decays over time as the initial concentration of the analyte undergoes redox reaction and is only replenished by diffusion.

For diffusion controlled reaction this current decays with $t^{1/2}$ and follows the Cottrell-equation (Bard 2000):

$$I(t) = nFAc_0\sqrt{\frac{D}{\pi t}} \tag{2.59}$$

where n is the number of electrons in the redox process, F is the Faraday constant, A is electrode area, c_0 the bulk concentration of the electro active species, D is the diffusion coefficient of the redox species and t is time.

The potential step applied between the working and reference electrode also causes a nonfaradaic response in the form of the reordering of the ion double layer near the electrode surface. This current generated from the charging of the double layer is purely capacitive and decays exponentially over $(t) \propto e^{-kt}$. This capacitive current is only significant during the initial period following the step and can usually be avoided by only taking the data of the last 90% of the step time into account.

Protocols

The electron transfer rate was measured by chronoamperometry, using the same buffer and experimental setup as for cyclic voltammetry. The bias potential was stepped from 0 V to various over-potential of 0.2 – 1 V and the current response was monitored over time.

2.2.10 Transistor I-V Characteristics

The operation of the high-electron-mobility-transistor (HEMT) in general is similar field effect transistors (FET). But unlike other types of transistors conduction is determined by the formation of a two-dimensional electron gas (2DEG) close to the Hetero-junction between two semiconductor phases, allowing for a high mobility of the electrons. As a result an enhanced performance is achieved for HEMTs compared to standard junction or metal-oxide-semiconductor-FETs. For the AlGaN/GaN HEMT used in this study the 2DEG is formed by the diffusion of electrons from the n-type AlGaN to the hetero-junction (Figure 2.12b). The bias or gate potential (V_G) applied to the transistor gate modulates the number of electrons in the 2DEG and thus the carrier mobility and transistor conductivity (Ambacher 2000). Such changes are observed by the determination of the transistor current-voltage (*I-V*) characteristics, by recording of its output and transfer curves. The Output characteristics are gained by recording the current at the drain electrode (I_{DS}) versus the voltage applied between the drain and source contacts (V_{DS}) at various V_G. As shown in Figure 2.12c the characteristic output curves of

an n-channel transistor can be divided in different regions. When $V_G < V_{th}$, with V_{th} as the threshold voltage, the transistor is in the subthreshold region. The threshold voltage is defined as the minimum gate voltage (V_G) where a conducting path between the drain and source contacts in the transistor is established. Below V_{th} only a thermally induced subthreshold current is observed (Gray 2001). At higher V_G conduction through the transistor is possible and the transistor is in "on-state". It then performs in a linear or ohmic region, when $V_G > V_{th}$ and $V_{DS} < V_G - V_{th}$. The drain to source current (I_{DS}) through the transistor is linearly proportional to the applied voltage V_{DS} and is given by equation 2.60 (Thuselt 2005), while the slope gives the output resistance.

$$I_{DS} = \mu C_s \frac{w}{L}\left[(V_G - V_{th})V_{DS} - \frac{1}{2}V_{DS}^2\right] \tag{2.60}$$

At $V_{DS} \geq (V_G - V_{th})$ the transistor reaches the saturation region and a near constant saturation-current $I_{DS,sat}$ is observed, given by (Thuselt 2005):

$$I_{DS,sat} = \mu C_s \frac{w}{2L}(V_G - V_{th})^2 \tag{2.61}$$

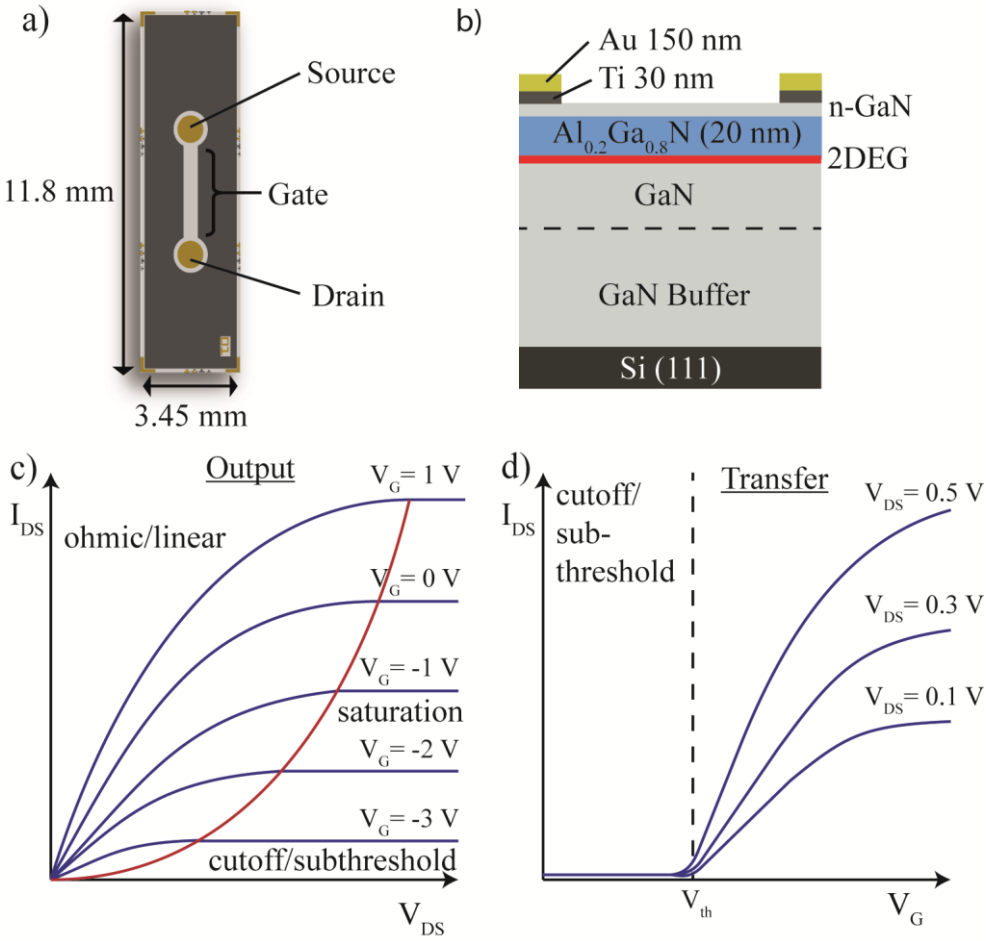

Figure 2.12: *(a) Realistic top view of a processed GaN/AlGaN/GaN HEMT and (b) schematic side view. (c) Schematic Output- and (d) Transfer-characteristics of the GaN/AlGaN/GaN HEMT.*

The transfer curves (Figure 2.12d) are gained by measuring I_{DS} versus the applied gate voltage (V_G) at various drain-source-potentials (V_{DS}). It is used to identify the region of linearity and to determine transconductance g_m of the transistor the from its slope, which is dependent on the capacitance C_s of the AlGaN layer, the carrier mobility μ in the 2DEG and geometric factors of the channel width w and length L of the transistor (Thuselt 2005).

$$g_m = \frac{\partial I}{\partial V} = \mu C_s \frac{w}{L}(V_G - V_{th}) \tag{2.62}$$

Further extrapolation of the linear region to $I_{DS} = 0$ allows the determination of the threshold voltage (V_{th}). With increasing V_{DS} higher currents are obtained. According to ohmic law, $\cdot\, dI = dV$, the rise in V_{DS} leads to a higher potential gradient dV and thus a larger current in the transfer curves. Larger V_G on the other hand induce higher carrier

densities in the conducting channel or 2DEG, increasing the conductivity and at constant *dV* a larger current.

Protocols

The current-voltage (*I-V*) characteristics of GaN/AlGaN/GaN HEMT and organic C8-DNBDT semiconductor chips before and after functionalization were measured in a self-built liquid (Figure 2.13) cell by gating the chip in HEPES (10 mM) with NaCl (150 mM, pH 7.5) with a Ag/AgCl reference electrode. Two gold needles protected with o-rings from the surrounding electrolyte were used to contact the source and drain of the chip. A double source-meter (Keithley Instruments GmbH, Germering, Germany) setup was used to apply the drain-source voltage V_{DS} and the gate potential V_G. The measurement software was written in LabView (National Instruments, USA) and recorded the relationships between the drain-source current I_{DS} and V_G (transfer curves) were monitored at constant V_{DS} of – 3 V and – 30 V, and I_{DS} versus V_{DS} (output curves) was recorded for fixed V_G between 5 V and – 30 V for organic C8-DNBDT semiconductor samples. Transfer curves for GaN HEMT samples were recorded at V_G between – 3.5 V and 0.5 V at constant V_{DS} of 0.3 V and output curves at fixed V_G between – 3 V and 0.5 V.

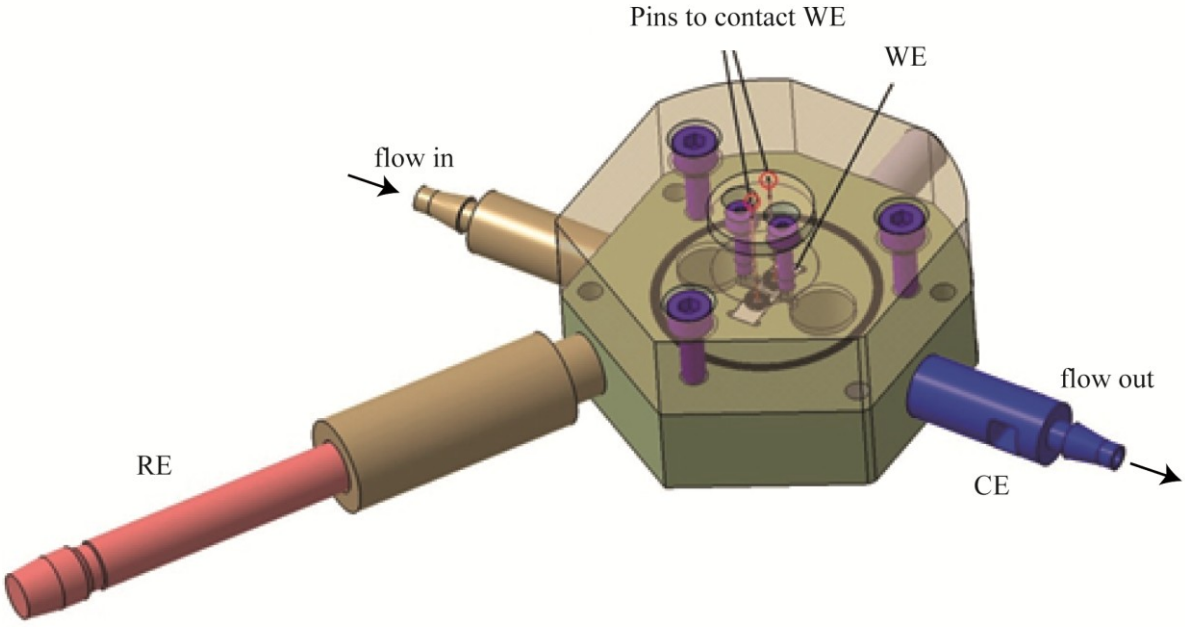

Figure 2.13: *3D-model of the electrochemical flow chamber (developed by Eickhoff group, Univertity Gießen/Bremen) used for the characterization of HEMT samples (WE). Gate potential is applied by an external potentiostat between Ag/AgCl reference electrode*

(RE) positioned in the inflow reservoir and platinum counter electrode (CE) at the chamber outflow.

2.2.11 Spin Coating

Spin coating is a procedure used for the deposition of uniform thin films on flat substrates by the use of centrifugal force of a rotating plate. A small amount of a dissolved polymer or molecule that forms the film is deposited in the center of the substrate. High speed rotation of the substrate causes the coating solution to spread over the substrate (Figure 2.14).

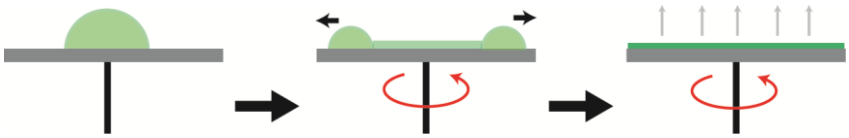

Figure 2.14: *Schematic representation of the spin coating process. Film formation is induced by the spreading of the coating solution by rotation of the substrate and subsequent evaporation of the solvent.*

Usually a volatile solvent is used that evaporates simultaneous as the film is deposited. The resulting film thickness is highly dependent on the coating material concentration and the angular speed of the rotating substrate as shown in equation 2.63. The final height h is defined as (Norrman 2005):

$$h = \left(\frac{3c^3(t)\vartheta_0\phi}{2[1-c_0(t)]\omega^2}\right)^{1/3} \tag{2.63}$$

Where ϕ is the solvent evaporation rate, ϑ the kinematic viscosity of the solution, c the concentration of the deposited molecule or polymer and ω the spin rate.

For a stable deposition of the film subsequent backing is soften required. Spin coating is used microfabrication, e.g. for functional oxide layers on single crystal or glass substrates, where films with nanoscale thicknesses are produced, and the deposition of photoresist layers in photolithography (Middleman 1993).

3. Fundamentals

3.1 Properties of GaN/AlGaN/GaN High-Electron-Mobility-Transistors

Gallium nitride is a group-III-nitride semiconductor that can exist in the stable wurtzite and thermodynamically metastable zinc blende crystal structure (Lei et al. 1991). As shown in Figure 3.1 the more common wurtzite crystal structure is described by the lattice parameters a_0, c_0 and the distance between a nitrogen and group-III atom (e.g. Ga) along the c-axis u_0. Two crystal polarities can be discerned by the growth direction. A Ga-faced polarity is gained with the growth parallel to the c-direction and n-faced polarity in antiparallel direction. In this structure each group-III atom is surrounded by four nitrogen atoms forming a tetrahedron that is compressed in c-direction and elongated in the c-plane. With the difference in electronegativity between nitrogen and gallium ($\Delta\chi$ = 1.23) (Allred 1961) four microscopic dipole moments pointing towards the electronegative nitrogen are formed. Since the wurtzite structure is not centrosymmetric these dipoles do not compensate each other, thus generating a macroscopic spontaneous polarization P_{SP} of 0.029 Cm^{-2} in antiparallel direction to the c-axis (Bernadini 1997).

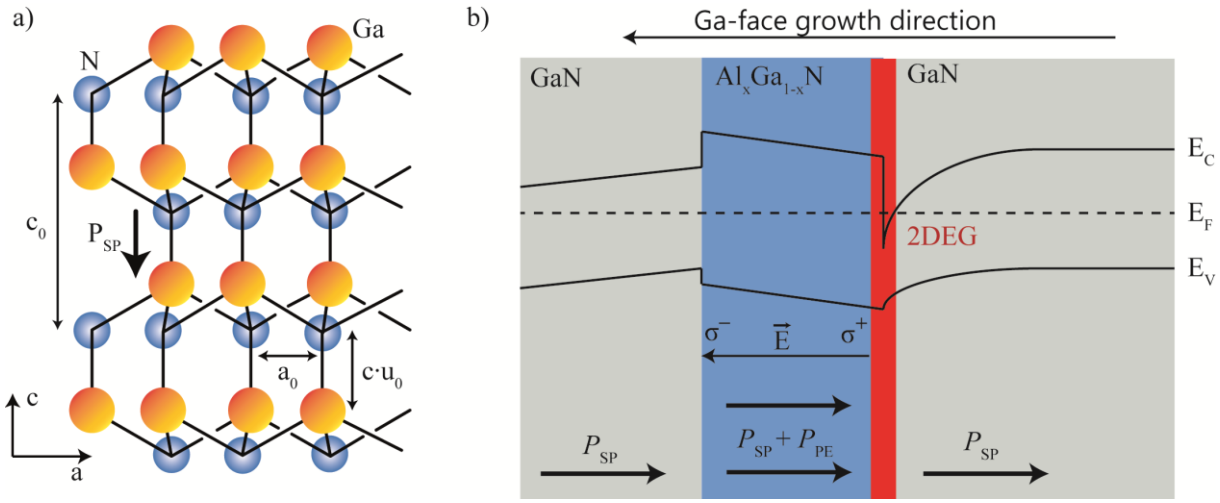

Figure 3.1: *(a) Schematic illustration of the structure and direction of the spontaneous polarization in the GaN wurtzite crystal. (b) Scheme of the band profile in the Ga-face GaN/ $Al_xGa_{1-x}N$/GaN heterostructure used in this work, indicated with the directions of spontaneous and piezoelectric polarization and the resulting induced sheet charge density σ of the $Al_xGa_{1-x}N$ layer.*

In the $Al_xGa_{1-x}N$ alloy used in the HEMT heterostructures both AlN and GaN exist in wurtzite structure. The spontaneous polarization in the AlN tetrahedron is 2.8 times higher (– 0.081 Cm^{-2}) than for GaN (Bernadini 1997), since AlN possesses a higher

difference in electronegativity ($\Delta\chi$ = 1.43) (Allred 1961). Further increase in the spontaneous polarization of AlN in comparison to GaN is obtained from the increase of u_0 from 0.376 to 0.380 (Bernadini 1997) and the decrease in the ratio c_0/a_0. Assuming the polarization in the $Al_xGa_{1-x}N$ phase scales linearly with the aluminum content x, its spontaneous polarization $P_{SP}(x)$ can then be given by (Ambacher 1999):

$$P_{SP}(x) = (-0.029 - 0.52x) \tag{3.1}$$

At layer thicknesses $d \leq 30$ nm and aluminum contents up to 0.38 the $Al_xGa_{1-x}N$ layer is pseudomorph (Ambacher 2000), causing compressive strain along and tensile strain perpendicular to the growth direction from the difference in lattice parameters of AlN and GaN. This strain causes an additional piezoelectric polarization P_{PE} of the $Al_xGa_{1-x}N$ layer and thus this layer exerts a significantly larger total polarization $P(x)$ than the strain less GaN layer. The total polarization $P(x)$ is given by:

$$P(x) = P_{SP}(x) + P_{PE}(x) \tag{3.2}$$

Where P_{PE} is dependent on the elastic constants $C_{13}(x)$, $C_{33}(x)$ and piezoelectric constants $e_{31}(x)$ and $e_{33}(x)$ of the wurtzite crystal lattice (Ambacher 1999):

$$P_{PE} = \frac{a_{strain}(x) - a_0(x)}{a_0(x)} \left(e_{31}(x) - e_{33}(x) \frac{C_{13}(x)}{C_{33}(x)} \right) \tag{3.3}$$

The sharp difference in polarization at the $GaN/Al_xGa_{1-x}N$ heterojunction causes the formation of sheet charge densities $\sigma(x)$ at the interfaces.

$$\sigma(x) = P(x) - P_{SP,GaN} \tag{3.4}$$

As indicated in Figure 3.1b, the sheet charge density formed in the lower $GaN/Al_xGa_{1-x}N$ interface for the Ga-faced heterostructure carries a positive sign ($\sigma^+(x)$) and is negative ($\sigma^-(x)$) at the upper interface closer to the surface. An electrical field $\vec{E}$ of about 1 $MVcm^{-2}$ (Ambacher 1999) in growth direction is generated between these sheet charge densities, that is significantly larger than for other group-III semiconductors (Chen 1995). The emergence of such a strong electric field induces the bending of the conduction and valence bands in the heterostructure as shown in Figure 3.1b, causing free electrons in the $Al_xGa_{1-x}N$ layer to accumulate at the lower GaN/AlGaN interface to compensate for the positive surface charge density. Due to this a quantum well in the conduction band, dropping below the Fermi level E_F at the lower GaN/AlGaN interface is formed (Ambacher 2000), where the accumulated free electrons are confined in z-direction (growth direction) in a highly conductive sheet, the so called 2D-electron-gas (2DEG).

For N-faced GaN the sign of the polarities and surface charges is inverted and the 2DEG is formed at the upper GaN/AlGaN interface. The sheet carrier concentration n_S in the 2DEG depends on the properties of the $Al_xGa_{1-x}N$ layer, mainly the aluminum content x, the thickness d of the layer, as well as the temperature T. The carrier concentration n_S decreases exponentially with T, as the amount of free electrons decreases in the $Al_xGa_{1-x}N$ layer, until it reaches a constant level at $T < 100$ K (Smorchkova 1999), while increases in d and x both lead to increases in n_S (Ambacher 1999). The increase in x not only influences n_S, but also the carrier mobility μ_S inside the 2DEG. An initial increase in μ_S is seen with rising x, due to an increased barrier height of the conduction and valence bands at the $GaN/Al_xGa_{1-x}N$ interface. This leads to a heightened screening of ionized impurities in the heterostructure, as the penetration of the electron wave function is reduced (Smorchkova 1999). Due to increasing alloy disorder and interface roughness with larger aluminum content μ_S starts to decrease at about $n_S > 2 \cdot 10^{12}$ cm^{-2} (Smorchkova 1999). Usually besides large carrier concentrations in the order of 10^{13} cm^{-2} (Ambacher 1999), a high mobility of electrons μ_S in the 2DEG of about 10^3 $cm^2V^{-1}s^{-1}$ (Smorchkova 1999) is achieved compared to other types of transistors, making the $GaN/Al_xGa_{1-x}N/GaN$ heterostructures a high electron mobility transistors (HEMT).

3.2 Surface Electronic Structure of (GaN) Semiconductors

The surface band structure of a semiconductor in contact with an electrolyte or other medium depends on its electron affinity χ_e. For a semiconductor the electron affinity is defined as the energy needed to release an electron from the semiconductor surface conduction band into the vacuum energy level and is given by (Sze 1985, Thuselt 2005),

$$\chi_e = \phi_W - \phi_{BB} - (E_C - E_F) \tag{3.5}$$

where ϕ_W is the work function, ϕ_{BB} the band bending, E_C and E_F the conduction band and Fermi energy levels. For other materials, such as metals, the electron affinity is equal to the work function ϕ_W. The work function defines the energy difference between the Fermi level E_F, where most of the carriers in metals exist, and the vacuum level. At the contact area of the semiconductor with an electrolyte or metal, the Fermi energy levels are equal, assuming thermodynamic equilibrium with no electron-transfer across the interface (Figure 3.2a). A difference in electron affinity emerges at the interface between the two materials, due to an intrinsic difference in their work functions. This creates a contact potential, forcing the band bending and thus redistribution of carrier density at the interface to the bulk semiconductor, forming the space charge region (Thuselt 2005).

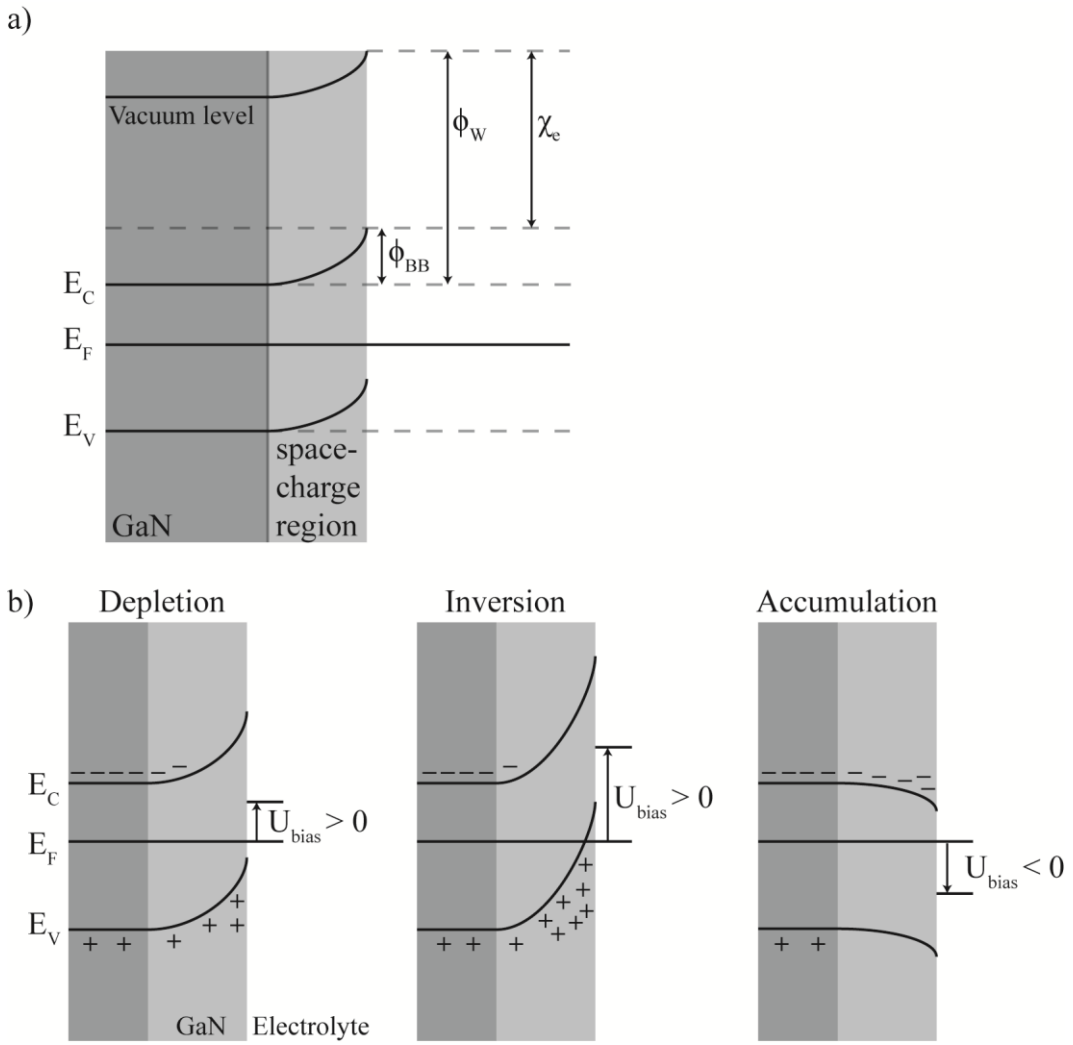

Figure 3.2: *(a) Schematic interface band structure of a semiconductor and (b) space-charge regimes for an n-doped semiconductor.*

The formation of the space charge region is directly influenced by changes in the surface charge, such as ion accumulation, pH changes and molecular dipoles (Bergveld 2003, Ashkenasy 2002, Steinhoff, Herrman 2003, Luber 2004), while the magnitude of the semiconductor electron affinity defines the sensitivity to such influences. As such, the space charge region is also modified by an external bias potential U_{bias} (Figure 3.2b). For an n-doped semiconductor the Fermi level of the electrolyte is raised compared to the semiconductor level at $U_{bias} > 0$, forming the depletion regime in the space charge region. In this regime the electron density near the interface is depleted. With increasing U_{bias} the valence band level E_V at the interface becomes higher than the Fermi level E_F. Holes become the majority carriers near the surface instead of electrons, while electrons are the bulk majority carriers, creating the inversion regime. Negative applied U_{bias} results in downwards band bending and the so called accumulation regime is formed, where the electron density at the semiconductor surface is increasing. For a p-doped semiconductor

the opposite reaction to the applied potential is observed. At a certain U_{bias} when there is no band bending at the surface ($\phi_{BB} = 0$) the flat band condition is reached. The flat-band potential U_{FB} at this condition is an intrinsic characteristic of the semiconductor and is sensitive to all changes in surface potential besides U_{bias}.

3.3 Requirements for Biosensor Applications

As described above the semiconductor electronic structure at the interface can be influenced by changes in the surface potential ψ_s. The resulting redistribution of majority carriers inside the semiconductor is seen in the modification of its space-charge capacitance C_{SC}. This relationship on the surface potential is given by the differential capacitance (Sze 1985):

$$C_{SC}(\psi_s) = \frac{\partial \sigma_s}{\partial \psi_s}$$

$$= \frac{\varepsilon\varepsilon_0}{\sqrt{2}d_n}\left(\frac{p_0}{n_0}\left(1 - e^{-\beta\psi_s}\right) + e^{\beta\psi_s} \Big/ \sqrt{\frac{p_0}{n_0}\left(e^{-\beta\psi_s} + \beta\psi_s - 1\right) + e^{\beta\psi_s} - 1}\right) \tag{3.6}$$

Here ε and ε_0 are the permittivity of the semiconductor and vacuum respectively, n_0 and p_0 the electron carrier and hole density in the bulk semiconductor, e the elemental charge, k the Boltzman constant and T the temperature. The Debye length d_n is given by $d_n = \sqrt{\varepsilon\varepsilon_0/e\beta n_0}$ and $\beta = e/kT$.

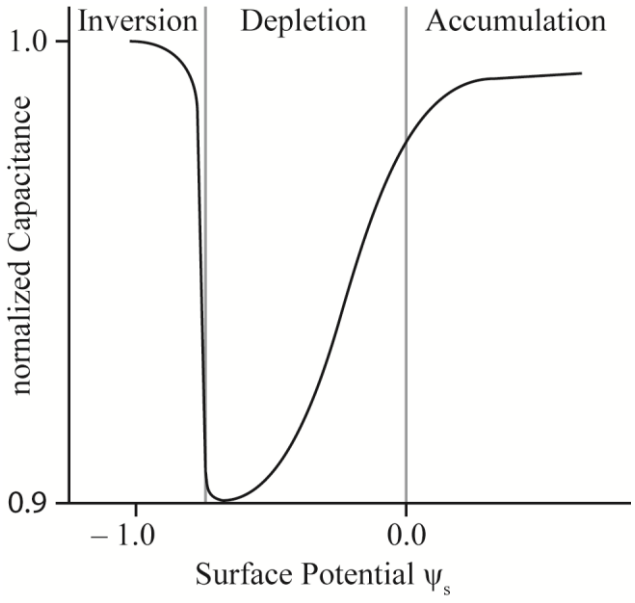

Figure 3.3: *Normalized space-charge capacitance as a function of semiconductor surface potential (ψ_s). $C_{SC}(\psi_s)$ is normalized to the insulator capacitance C_i in an electrolyte-insulator-semiconductor system (EIS). The three space-charge regimes show different capacitive sensitivities to changes of surface potentials.*

Figure 3.3 shows the simulated surface potential sensitivity of the differential space-charge capacitance $C_{SC}(\psi_s)$ that is normalized to the insulator capacitance C_i in an electrolyte/ insulator/semiconductor system. The three space-charge regimes at the semiconductor interface arise in dependence of the magnitude of surface potential. In the inversion regime the semiconductor shows the highest sensitivity of C_{SC} to changes in surface potential. However, the sensitive potential in this regime is narrow. In the depletion regime the potential range where C_{SC} is sensitive to ψ_s is broader and the Mott-Shottky relation (Equation 3.7) becomes linear, allowing for a direct correlation between ψ_s and U_{FB} (Sze 1985).

$$\frac{1}{C_{SC}^2} = \frac{2}{\varepsilon_0 \varepsilon_s N_d q}\left(U_{bias} - U_{FB} - \frac{kT}{e}\right) \tag{3.7}$$

Ensuring the linearity of $1/C_{SC}^2$ versus U_{bias} also allows for the extraction of the semiconductor doping ratio N_d. Under these conditions any changes in the surface potential, e.g. from changes in ion concentration, pH, and grafting of additional layers on the semiconductor surface, causes changes in the space-charge capacitance. In case of the GaN/AlGaN/GaN heterostructures used in this work, the band structure of the different semiconductor phases is also influenced by the surface potential. Depending on ψ_s the inclination of the band profiles is modulated and thus the depth of the quantum well, changing the carrier concentration accumulation in the 2DEG. This change is reflected in

the transistor *I-V* characteristics as C_s and μ are influenced by the surface potential ψ_s in equation 2.62.

4. Modulation of Electronic Band Structures in GaN Semiconductors Using Helical Peptides

4.1 Introduction

The physical properties of semiconductors are mainly determined by their crystalline structures. By changing the atomic composition, commonly via doping, the semiconductor properties can be modulated within narrow limits, as lattice strain becomes detrimental to the desired properties with increasing doping ratio. As a new strategy for a more flexible modulation of the electronic structures of semiconductor devices, the deposition of organic molecules is drawing increasing attention. This not only alters the semiconductor surface structure, but also the surface charges form the introduction of mono- or dipoles, which result in a change in electron affinity and band bending (Ashkenasy 2002, Bergveldt 2003). This concept was explored by the use of small organic thiols that exert a molecular dipole moment perpendicular to the surface of $\rho_{\perp} \leq 1.3$ D (Sengupta 2005). The change in surface potential induced by these molecules is for instance detectable in the lateral resistance of GaAs/AlGaAs heterostructures (Luber 2004). Instead of small organic molecules Kimura et al. further extended this strategy and used helical peptides as building blocks to extend the possible range of surface dipoles. In nature the peptide helix commonly exists in α-helical conformation and is one of the common secondary structures in proteins, which is known to carry macromolecular dipoles (Wada 1976). The formation of α-helical structures was studied by Karle and Balaram 1990, Otoda, Kimura *et al.* 1993, Toniolo *et al.* 2001, using synthetical oligopeptides containing 2-aminoisobutyric acid (Aib). As the allowed angles for the Aib residue occurred in two very restricted regions, corresponding to a right-handed α-helix or 3_{10}-helix or a left-handed α-helix, respectively (Marshall and Bosshard 1972, Burgess and Leach 1973), it is the most promising building block to achieve α-helical structures in artificial peptides. Since the Aib residue does not have an asymmetric Cα atom, L- or D-configuration of the helix is equally possible. L- or D-handedness of the helix is fixed by other residues in the peptide sequence (Karle and Balaram 1990). Due to the helix formation, the helical peptides can be considered as rigid rods with a diameter of approximately 1.5 nm. The dipole moment in helical peptides originates from each peptide bond in the sequence and can reach up to 3.5 D per peptide unit. Since the dipole moments in an α-helix are nearly parallel aligned to the helix axis (Wada 1976, Hol 1978), the peptides can exert a much larger macrodipole moments which is proportional to the number of peptide units (Hol 1978). A helical peptide with 16 amino acids for instance can amount to 50 D (Hol 1978, Sengupta 2005). The electric field generated from the dipole of these peptides alters the surface potential of semiconductors and has a various impact on protein functions, such as frequent N-termini binding of phosphate

moieties, long-range attraction of charged molecules or stabilization of intermediates (Hol 1978), indicating the potential of peptides as biosensing platform. It was further shown, that sequences of $(Ala\text{-}Aib)_n$ or $(Leu\text{-}Aib)_n$ adopt a stable α-helical conformation and form a well-packed monolayer on Au substrates with tilt angles of 30° to the surface normal (Fujita, Kimura *et al.* 1995, Miura, Kimura *et al.* 1998). The combination of dipole interactions and other secondary interactions, such as electron transfer processes, opens up an emerging field of "molecular dipole engineering" (Kimura 2008), using various functional nanoarchitectures inspired by the molecular design of nature. Following the previous studies on GaAs-based 2DEG devices functionalized with small organic molecules (Luber 2004), and their influence on the carrier mobility in GaAs-based 2DEGs (Kaindl 2010), several helical peptides based on $(Leu\text{-}Aib)_n$ sequences were covalently coupled to GaN surfaces. The use of the wide band gap (3.4 eV) semiconductor GaN and GaN/AlGaN/GaN HEMT structures promises high sensitivity for the flexible modulation of its electronic band structures by coupling of helical peptides with tunable macromolecular dipole moments. Following the sequence in Figure 4.1, covalent coupling of peptides was performed by first functionalizing the chemically oxidized GaN surface with an amino silane monolayer (Baur, Steinhoff et al 2005) followed by covalent coupling of the formyl terminated helical peptides to the amino silane layer. Other than the control of magnitude of macromolecular dipoles by the length of α-helices (Kaindl 2010), the sign of dipoles was altered by coupling α-helices either via their C- or N-terminus. Furthermore, one peptide sequence was functionalized with a terminal ferrocene moiety to investigate the electron transfer through the α-helices.

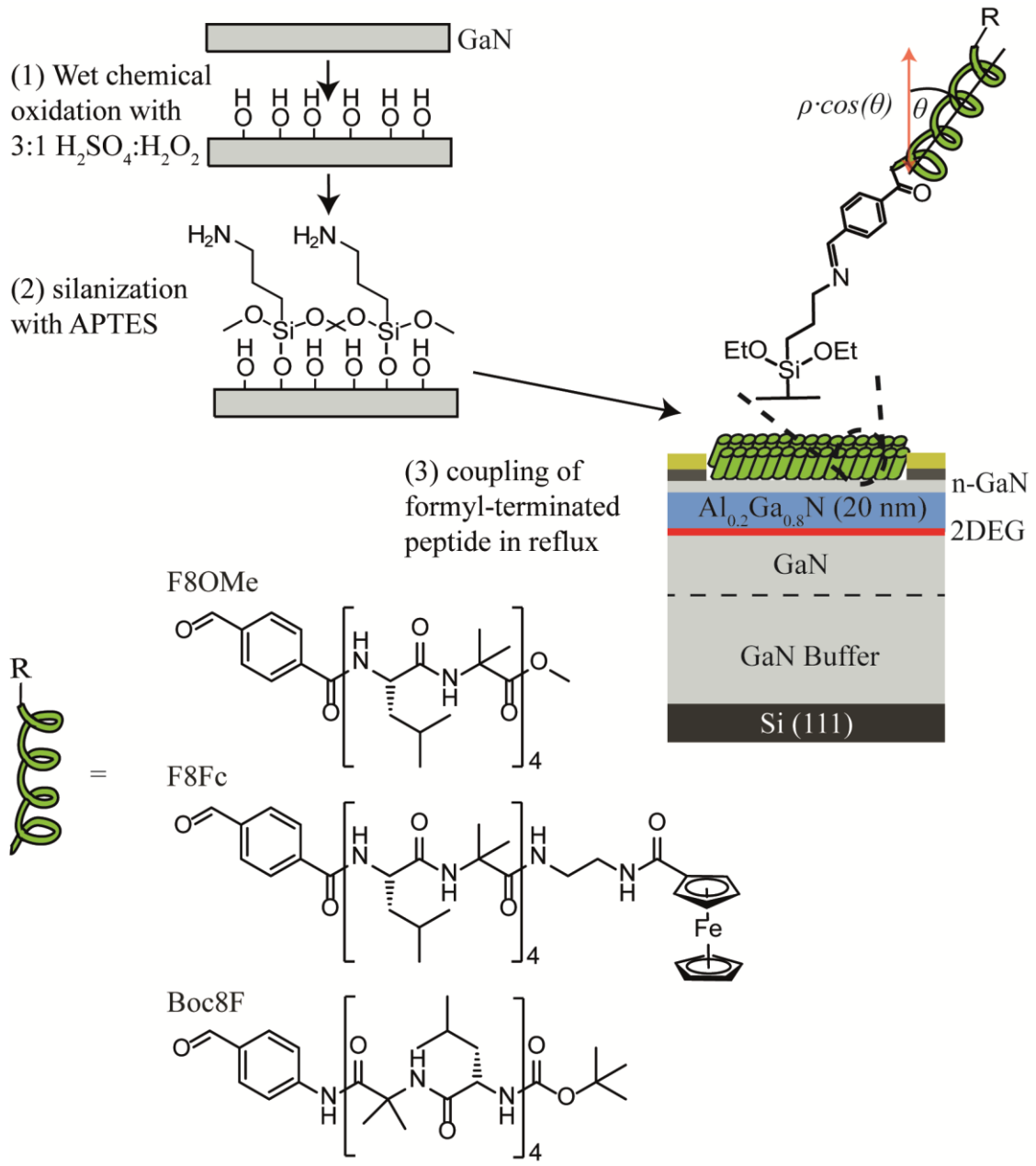

Figure 4.1: *Flow of the step-by-step functionalization of GaN.*

Various surface sensitive and electrochemical techniques were used in order to first characterize the surface modification and the modulation of electronic characteristics in GaN semiconductors. Functionalization protocols were later applied on GaN/AlGaN/GaN heterostructures to investigate the influence of the peptide dipole on the transistor *I-V* characteristics and carrier density in the 2DEG. The details of the obtained results are presented in the following sections. Parts of this Chapter were previously published in Mehlhose and Frenkel et al. 2018.

4.2. Topography, Chemical Composition and Fine-Structure Characterization of the GaN/Peptide Interface

Topographic profiles of planar GaN electrodes were characterized by contact mode AFM within an area of 1.5 × 1.5 μm^2 before and after the functionalization with APTES as well as deposition of peptide. The topographic profiles and scratch tracks are presented in the Supplementary Information section 9.1.1. A root mean square (rms) roughness of σ = 3.2 Å was obtained for the wet chemically oxidized GaN. The grafting of APTES and peptides led to a slight increase in the surface roughness to σ = 5.0 Å for F8OMe, σ = 5.9 Å for BocF8 and σ = 5.7 Å for F8Fc, with no major defects or piles of molecules observed. In fact, the film thickness of 13 Å, 15 Å and 18 Å determined for F8Fc, F8OMe and Boc8F respectively from the height difference between the film surface and the scratch track confirms the deposition of a peptide monolayer. After each functionalization step the chemical surface composition of GaN was assessed by XPS. Data for the Ga3d, N1s, Fe2p, C1s and O1s spectra from untreated GaN, APTES grafted GaN with and GaN deposited with APTES and peptides are presented in Table 4.1. The evolution of the Ga3d, N1s and Fe2p spectra upon functionalization is shown Figure 4.A for the F8Fc peptide.

Table 4.1: *Mean atomic composition from XPS in percentages of untreated GaN, GaN grafted with APTES and GaN grafted with APTES and peptides (F8OMe, Boc8F and Fc8F).*

Sample	**Concentration (%)**					**Ratio**			
	Ga	**O**	**N**	**C**	**Fe**	**N/C**	**O/C**	**N/Ga**	**Fe/C**
GaN	28	9	21	42	0	0.50	0.20	0.75	-
APTES	21	16	16	47	0	0.35	0.35	0.78	-
F8OMe	19	15	16	49	0	0.32	0.31	0.82	-
Boc8F	11	35	10	44	0	0.22	0.80	0.87	-
Fc8F	17	15	15	50	3	0.29	0.31	0.90	0.05

As shown in Table 4.1, a monotonic decrease in Ga3d signals was observed after each grafting step. The Ga surface concentration decreases from bare (28 %) to lower concentrations for APTES (21 %) and peptide coated samples (11-19 %). The same trend was seen for the concentration of N, while an increase in the N/Ga ratio was observed from bare (0.75) to APTES (0.78) and peptide grafted GaN (0.82-0.90), indicating a growth of the organic layers after each reaction step as more layers containing N are deposited. A decrease in the N/C ratio a can clearly be seen as well after each successive reaction step, further confirming a successful layer deposition. Compared to the APTES

sample F8OMe showed the least difference in concentration of N and Ga out of all peptides. This might be due to a lesser density of the peptide layer. For all other peptides the change is more pronounced, indicating higher densities in those films. Moreover, Fe2p doublet peak near 710 eV binding energy was detected for F8Fc (Figure 4.2c), confirming the successful grafting of the ferrocene ferrocene-functionalized F8Fc peptides.

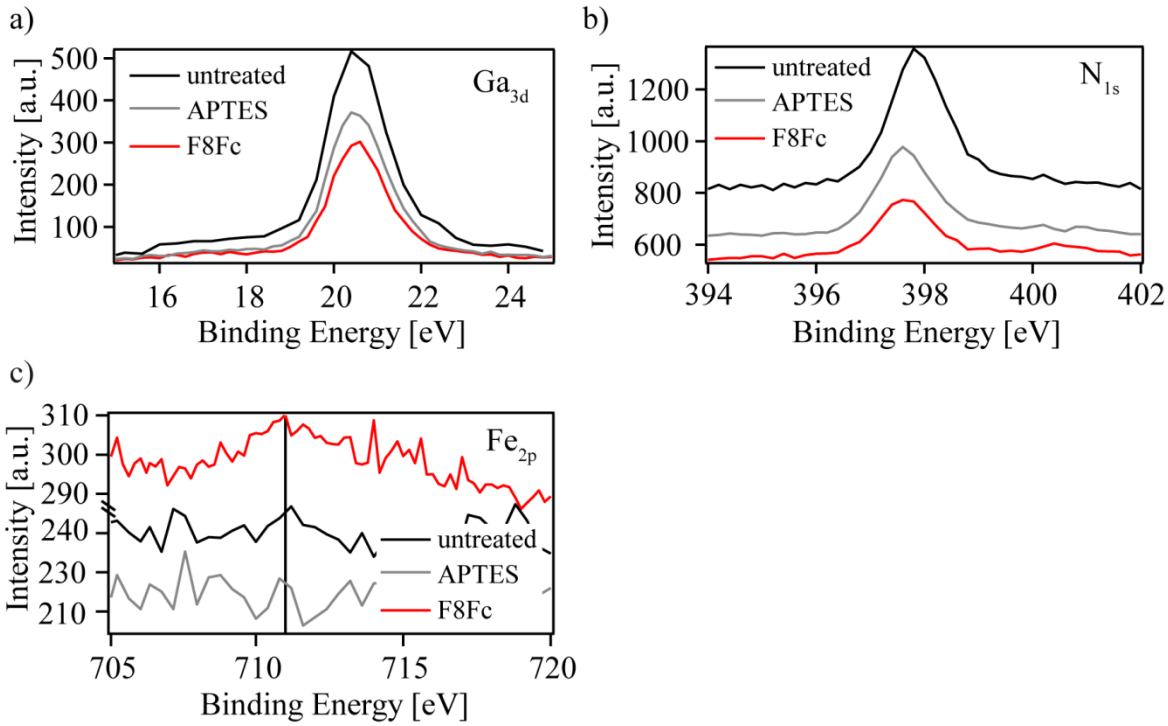

Figure 4.2: *Core level spectra of (a) Ga3d, (b) N1s, and (c) Fe2p from untreated GaN (black), APTES grafted GaN (grey) and GaN after the deposition of APTES and F8Fc (red).*

The thickness, roughness, and density of the films were evaluated by XRR after each reaction step. The preparation protocols were first tested on bulk GaN and the best procedure transferred to the GaN/AlGaN heterostructure. Since the features in the curves are not very prominent, due to the high transparency of the samples the XRR curves were normalized by q_z^4 and given as Fresnel plot. The XRR curves of wet chemically oxidized GaN (black), GaN coated with APTES and F8OMe (orange), Boc8F (blue), and F8Fc (red) are shown in Figure 4.3.

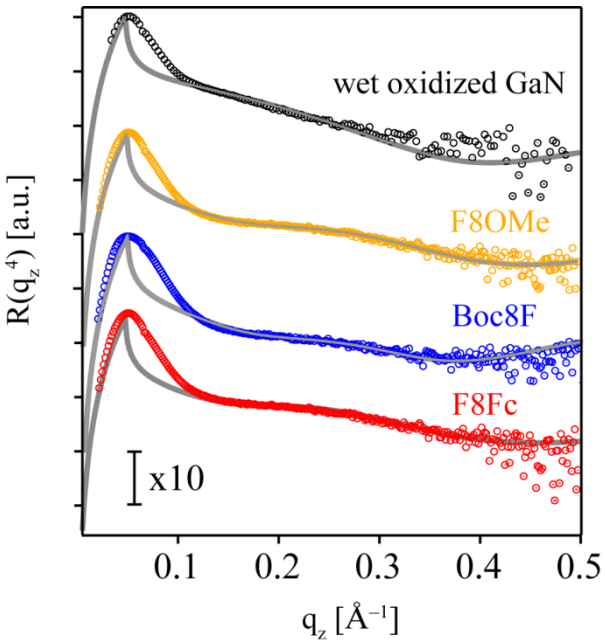

Figure 4.3: *Fresnel plots of wet chemically oxidized GaN (black) and GaN after the grafting of APTES and peptide layers. Orange, blue and red symbols correspond to the experimental data of F8OMe, Boc8F and F8Fc peptides respectively and the solid lines represent the fitting results.*

The bulk GaN samples the measured XRR signals could be well fitted with a three slab model consisting of a slab for peptide, APTES and wet chemically oxidized GaN layers on bulk GaN. For all investigated GaN samples thickness values for the oxide layer of d_{oxide} = 5 – 6 Å and APTES layer of d_{APTES} = 5 – 8 Å were obtained. The obtained APTES thickness lies very well within reasonable range for a monolayer with an expected thickness of 9 Å (Kim 2011). Additionally the thicknesses of these layers were also investigated before grafting of the peptide by ellipsometry. APTES layers of 9 Å, 5 Å and 7 Å were found for the samples to be grafted with F8OMe, Boc8F and F8Fc respectively, confirming the values obtained by XRR. Thickness, scattering length density and roughness values for the peptide layers on bulk GaN are given in Table 4.2.

Table 4.2: *Best fit parameters ($\chi^2 \leq 0.01$) for the XRR results for the F8OMe, Boc8F or FcF8 peptide layer coupled over APTES to bulk GaN.*

Peptide	*d* [Å]	*SLD* [10^6 Å^{-2}]	*σ* [Å]
F8OMe	16.4	5.4	5.5
Boc8F	16.9	6.4	5.0
FcF8	14.8	6.5	5.5

The thickness values of the peptide layers were found to be d_{F8OMe} = 16.4 Å, d_{Boc8F} = 16.9 Å, and d_{F8Fc} = 14.8 Å for F8OMe, Boc8F, and F8Fc peptides respectively. For comparison, estimated lengths *L* of the peptides were calculated by summing up the helix length, the lengths of the two linker parts, and the size of a ferrocene unit (Arikuma 2010). The helix lengths were estimated with 2.0 Å per residue for a 3_{10}-helix of an octamer (Benedetti 1991). For an α-helix (16mer−64mer) the length per residue 1.5 Å should have been considered (Benedetti 1991). The half value of the full-extended length of the linker parts was taken as approximation, because of the unknown conformation and tilt angles. A ferrocene unit was assumed to be a sphere with a 6 Å diameter. Finally, the calculated lengths of the peptides shown in Figure 4.1 are L_{F8OMe} = 19 Å, L_{Boc8F} = 20.5 Å, L_{F8Fc} = 26.0 Å. The obtained thickness values of each peptide are smaller than the theoretically expected length *L*, suggesting that the helical axis is tilted to the direction normal to the substrate plane. The tilt angles from the surface normal were estimated from the ratio between the peptide thickness *d* calculated from XRR and the estimated length of the molecule *L,* $\cos(\theta) = d/L$. The tilt angles found for F8OMe and Boc8F peptides of θ_{F8OMe} = 30.3° and θ_{Boc8f} = 35.5° agree well with similar peptide monolayers from Kimura et al. (Morita and Kimura 2003). For the F8Fc peptide a larger tilt angle of θ_{F8Fc} = 55.3° was found, due to its smaller layer thickness compared to the other peptides. Gaussian roughness values of σ = 4.5 – 5.5 Å at the air/peptide interface were obtained for all measured samples, implying a consistent and homogenous coverage of the peptide layer. These values are consistent between AFM and X-ray reflectivity, although they are estimated in two different manners. Roughness measured by X-ray reflectivity coincides with the gradual change in the scattering length density across the interface and *σ* measured by AFM is calculated from the topographic image. Scattering length densities (*SLD*) of the peptides, SLD_{F8OMe} = $5.4 \cdot 10^{-6}$ Å^2, SLD_{Boc8F} = $6.4 \cdot 10^{-6}$ Å^2, and SLD_{F8Fc} = $6.5 \cdot 10^{-6}$ Å^2, are in reasonable agreement with the value of peptides composed of the same amino acid components grafted on GaAs, $5.6 \cdot 10^{-6}$ Å^2 (Kaindl 2010). From the obtained *SLD* and thickness *d* values of the peptide layers the occupied area *A* of one peptide helix can be calculated can be gained by:

$$A = \frac{r_e \cdot N_e}{SLD \cdot d} \tag{4.1}$$

where r_e is the Thomson electron radius and N_e is the total number of electrons per molecule. The occupied areas per peptide molecule for F8OMe and Boc8F, A_{F8OMe} = 174 Å^2 and A_{Boc8F} = 134 Å^2, seems to agree well with the values reported previously for a peptide with twice as more repeat units measured at the air/water interface, *A* = 150 Å^2 (Kaindl 2010, Kitagawa 2002). An apparently larger area was estimated for F8Fc, A_{F8Fc} =

185 $Å^2$, further suggesting a larger molecular tilt from the direction normal to the substrate, which seems reasonable from its smaller thickness value.

Previously, similar surface coverage results were achieved with other helical peptide SAMs on Au. For instance, tridecapeptides bound to a gold surface at their C-terminal had surface coverage to a lesser extent than those bound at their N-terminal (Morita and Kimura 2003). In addition, other Aib-containing helical peptide SAMs bound to a gold surface via the N-terminal were more dense than the peptide SAM bound via the C-terminal (Fujita et al 1998). The less dense packing of the latter films was explained by unfavorable electrostatic repulsion which possibly takes place between the dipoles of the helical peptide directing towards an aqueous phase and the dipoles of an S-Au linkage opposing the helix dipoles. However, other factors such as the chain-length difference at the anchor part of the molecules and the different size and polarity of the protecting terminal groups could not be excluded (Morita et al 2000, Biebuyck and Whitesides 1993, Nuzzo et al 1987). The difference in SLD between F8OMe and Boc8F is not significant enough to support this for the peptides used in this work. Orientation of the dipole moment has seemingly no effect on the density of the surface coverage. This affinity for less dense packing of C-terminal peptides might be reduced in Boc8F due to the usage of aminobenzaldehyde as a link for covalent bonding to the surface. In this case an opposing dipole moment as seen in the S-Au linkage in SAMs on Au substrates might not present.

4.3. Electrochemical Characterization of Peptide/GaN Interface

Electrochemical characterization was performed on Ge-doped bulk GaN electrodes with a carrier concentration N_d of $1 \cdot 10^{20}$ cm^{-3}. The very high carrier density achieved by doping with Ge as a donor allows the preparation of sufficiently sensitive electrodes to track the change in electrochemical properties by means of impedance spectroscopy (Fritze 2012). Impedance spectra were measured between 100 kHz and 50 mHz in standard HEPES buffer and analyzed with equivalent circuit model 2 for the untreated GaN/electrolyte interface and model 3 for the APTES and peptide grafted GaN (Figure 4.4, see section 2.2.7). At $f < 50$ mHz the signal to noise ratio becomes too low. The fit results for untreated GaN (black), GaN after the deposition of APTES (green), F8OMe (orange), Boc8F (blue), and F8Fc (red) are represented as Nyquist plot of $-Z''$ as a function of Z' (Figure 4.4b) and summarized in Table 4.3.

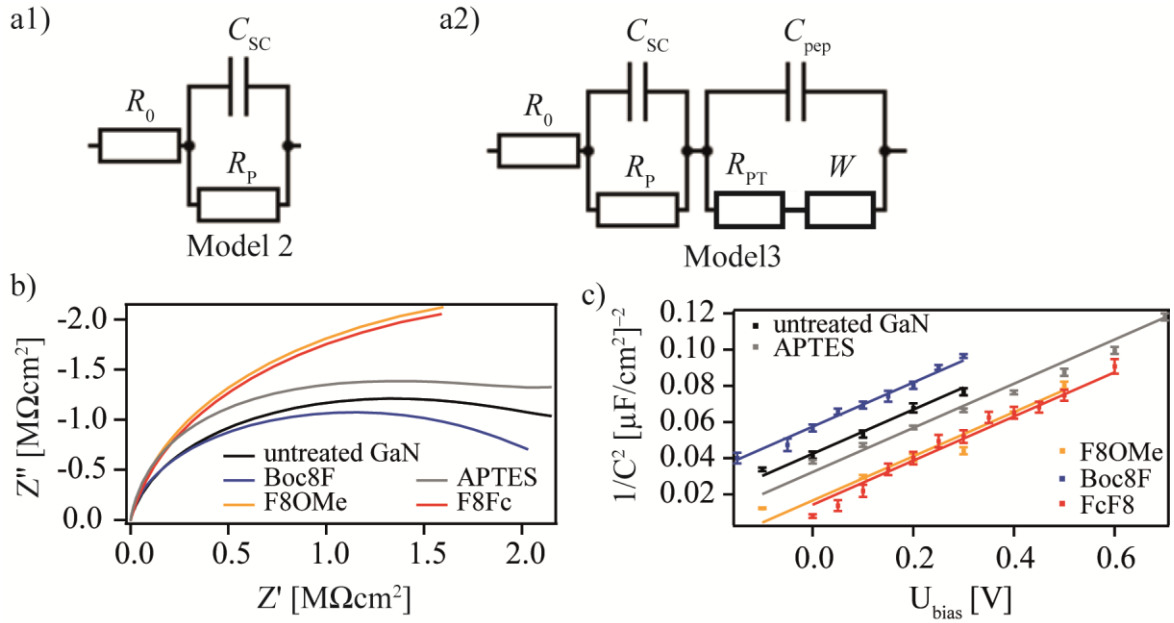

Figure 4.4: *(a1) Simplified circuit model 2 for the semiconductor/electrolyte interface. (a2) Expanded circuit model 3, accounting for the additional peptide layer. The peptide layer is modeled by the parallel combination of the capacitance C_{pep}, phase transfer resistance R_{PT}, and Warburg element W (b) Impedance spectra of bare GaN (black), GaN coated with APTES (grey) and F8OMe (orange), Boc8F (blue), and F8Fc (red), measured in the frequency range between 100 kHz and 50 mHz. (c) Mott-Shottky plots calculated from the impedance spectra.*

From Figure 4.4b one can clearly see a distinct change in impedance spectra upon deposition of APTES and the subsequent peptide. Interestingly, F8OME and F8Fc peptides, whose macromolecular dipole moments point towards GaN, show an almost identical change in the global shape of the curves. The Boc8F peptide in contrast, where the helix sequence and its dipole moment point to the opposite direction, showed a shift in the opposite direction.

Table 4.3: *Fitting coefficients from impedance spectroscopy.*

coating	C_{SC}[a] [µF/cm²]	U_{FB}[a] [V]	C_{pep} [µF/cm²]	R_{PT} [Ω/cm²]	W [MΩ/cm²]
Untreated GaN	3.56	– 0.38	-	-	-
APTES	3.88	– 0.35	1.1	1092	0.29
F8OMe	4.33	– 0.14	1.4	2743	0.40
Boc8F	3.26	– 0.47	1.5	1763	0.30
F8Fc	4.39	– 0.12	1.2	1818	0.44

[a] C_{SC} measured at U_{bias} = 0.2 V, [b] U_{FB} for peptide/GaN systems determined from the linear extrapolation of Mott-Schottky plots (0 V ≤ U_{bias} ≤ 0.6 mV).

The electrochemical properties of APTES and peptide layers could be best represented by the equivalent circuit model 3 (Figure 4.4a2), that includes additional impedance representations for the APTES or peptide layer capacitance C_{pep}, phase transfer R_{PT}, and Warburg element W. (Hillebrandt and Tanaka 2001, Schubert 2009,) With the introduction of W the APTES and peptide layers cannot be assumed as pure dielectric layers, represented by the parallel combination of a resistance and a capacitance. The Warburg element in this model is necessary to account for the frequency dispersion of impedance spectra at high Z' values, as seen for APTES-coated GaN, due to the occurrence of kinetically or diffusion controlled charge processes. From the Warburg impedances obtained in Table 4.3, a clear deviation from an ideal dielectric layer model can be discerned. This suggests that these layers can act as a diffusion barrier for ions. The Warburg impedance can be used as an approximation to quantify diffusion of ions through the APTES layer. With

$$Z_W \equiv W(\sigma_w) = \left(\sigma_w + \frac{1}{\sigma_w}\right)\omega^{-1/2}\,,\ \sigma_w = \frac{4RT}{\sqrt{2}n^2F^2A\rho}\,\frac{1}{\sqrt{D}} \qquad (2.48, 2.49)$$

the diffusion coefficient D of ions through the peptide layer, can be calculated from the Warburg impedance $W(\omega)$, [26] where A is the active electrode area, ρ the ion concentration at the interface and R, T, n, and F have their usual meaning.

With the assumption of a comparable ion concentration at the GaN interface as in the bulk electrolyte the Warburg parameter can be calculated to σ = 8.5 x 10^4 V/A $s^{1/2}$ and the diffusion coefficient of ions in the peptide layer to $D = 3.1 \cdot 10^{-4}$ $\mu m^2 s^{-1}$. Compared to the diffusion coefficient of ions in bulk solutions ($D \sim 10^3$ $\mu m^2 s^{-1}$) (Poisson and Papaud 1983), this diffusion constant is seven orders of magnitude smaller. This suggests the formation of highly dense layers of helical peptides acting like a diffusion barrier that significantly suppress the diffusion of ions, similar to other self-assembled monolayers and supported lipid monolayers (Hillebrandt and Tanaka 2001, Frenkel 2014). Additionally, the rise in C_{pep}, W as well as R_{PT} after grafting of peptides on APTES coated GaN further confirms the successful peptide deposition. As seen from Table 4.3 the subsequent grafting of APTES and peptide incurs changes in the semiconductor space charge capacitance C_{SC}. The dependency of C_{SC} on the applied U_{bias} shows linear behavior in the Mott-Schottky plots in Figure 4.4c (C_{SC}^{-2} vs. U_{Bias}) for untreated GaN (black), GaN after the deposition of APTES (grey), F8OMe (orange), Boc8F (blue), and F8Fc (red) at the applied U_{bias} range of 0 V $\leq U_{bias} \leq$ 0.6 mV, confirming that the GaN semiconductor operates in the sensitive depletion region. This allows the calculation of the change in the flat band potential U_{FB} from the linear extrapolation of the Mott-Schottky plot of each peptide/GaN system given by the Mott-Shottky relation:

$$C_{SC}^{-2} = \frac{2}{\varepsilon_0 \varepsilon_S N_d q}\left(U_{bias} - U_{FB} - \frac{kT}{e}\right) \quad (3.7)$$

From the slope of each plot the carrier concentration N_d = $1.1 \cdot 10^{20}$ cm^{-3} could be determined using ε_S =8.9 (Levinshtein 2001) for the GaN semiconductor, which agrees well with the value determined from Hall effect measurements of $N_{d(Hall)} = 1 \cdot 10^{20}$ cm^{-3} on the same wafer.

From the grafting of APTES on GaN only a slight increase in C_{SC} from $C_{SC(GaN)}$ = 3.56 µFcm^{-2} to $C_{SC(APTES)}$ = 3.88 µFcm^{-2} was observed. This increase also causes a slight, but already clearly distinguishable increase in the flat band potential from $U_{FB(GaN)}$ = – 0.38 V to $U_{FB(APTES)}$ = – 0.35 V as seen in Figure 4.4c, possibly due to the change in surface potential incurred by partial protonation of the APTES amino groups. The subsequent grafting of peptides caused a much more pronounced change. For F8OMe (orange) the interface or space-charge capacitance C_{SC} and U_{FB} increased to $C_{SC(F8OMe)}$ = 4.33 µFcm^{-2} and $U_{FB(F8OMe)}$ = – 0.14 V, causing a change in U_{FB} compared to APTES only coated GaN of $\Delta U_{FB,F8OMe}$ = 0.21 V. Due to the dipole potential of F8OMe pointing towards GaN the surface potential is increased, causing the change in band bending at the semiconductor interface and thus increase in C_{SC}. This notion is further supported by the deposition of Boc8F (blue), which exerts a dipole moment opposite direction. The grafting of this peptide caused a shift to the opposite direction in the Mott-Schottky plot and a decrease in C_{SC} and U_{FB} to $C_{SC(Boc8F)}$ = 3.26 µFcm^{-2} and $U_{FB(Boc8F)}$ = – 0.47 V with a change in U_{FB} compared to APTES only coated GaN of $\Delta U_{FB,Boc8F}$ = – 0.12 V. This was further verified by F8Fc (red), that has the same helical part as F8OMe and caused changes in C_{SC} and U_{FB} in the same direction and with comparable magnitude. With $C_{SC(F8Fc)}$ = 4.39 µFcm^{-2} and $U_{FB(F8Fc)}$ = – 0.12 V the caused $\Delta U_{FB,F8Fc}$ = 0.23 V compared to APTES only coated GaN is similar to the value achieved from the grafting of F8OMe. These results indicate that the macromolecular dipole moments exerted by helical peptides can play a dominant role for the modulation of surface potentials and semiconductor band profiles.

4.4. Investigation of Electron Transfer Across Peptide Helices

To investigate the possibility of electron transfer across the peptide layer the peptide helix was modified with a redox active ferrocene moiety for F8Fc. First, Cyclic voltammetry of untreated GaN (black) and GaN coated with F8OMe (orange) was performed at scan rates of v_{scan} = 50 – 120 mVs^{-1} in 100 mM Na_2SO_4 (Figure 4.5a).

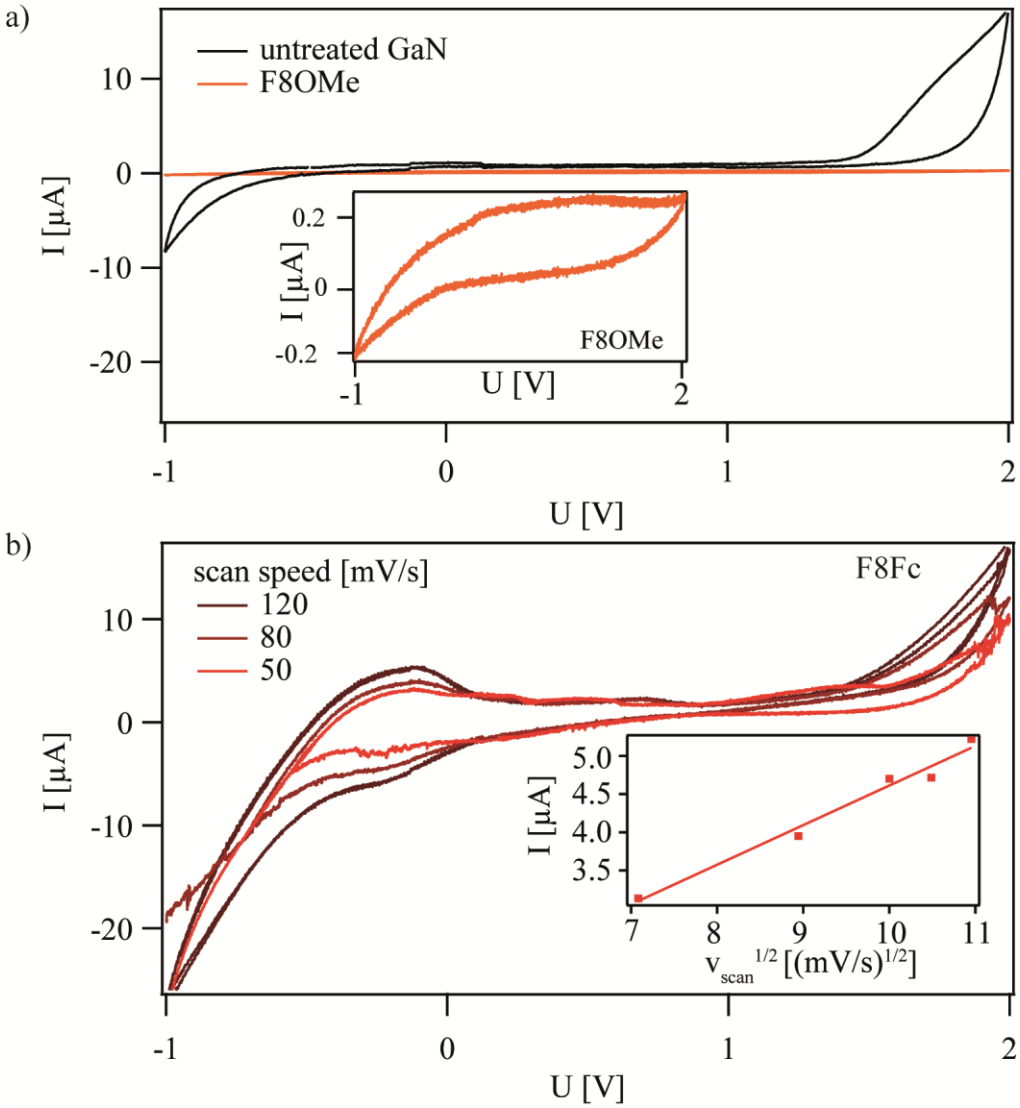

Figure 4.5: (*a) Cyclic votlammograms of F8OMe coated GaN (orange) and untreated GaN electrodes (black) with 0.1M Na_2SO_4 supporting electrolyte at scan speed of v_{scan} = 100 mV/s. (b) Cyclic votlammogram of F8Fc coated GaN in the same electrolyte, measured at v_{scan} = 50, 80, and 120 mVs^{-1}. The Dependency of peak oxidation current I_{peak} for F8Fc on the scan speed is presented in the inset.*

The unmodified GaN electrode showed no sign of irreversible electrochemical degradations in the applied voltage range, owing to the excellent chemical stability compared to GaAs (Adlkofer 2000). Interestingly, the deposition of F8OMe resulted in a drastic suppression of two orders of magnitude for both oxidation and reduction currents. This can be explained by the formation of a diffusion barrier by the grafted peptides, as seen from impedance results, causing the suppression of ion diffusion and thus charge transport towards the GaN electrode interface. For the ferrocene-functionalized peptide (F8Fc) coated GaN, distinct oxidation peaks i_{pc} at $U = -0.16$ V could indeed be detected (Figure 4.5b). Although weak the observed peaks were stable over multiple cycles. Additionally, anodic reduction peaks could not be clearly discerned at lower scan speeds, which could be attributed to the decomposition of the ferrocenium ion process in the presence of Na_2SO_4 after the oxidation process. A linear relationship between oxidation peak current I_{peak} and the square root of the scan rate $v_{scan}^{1/2}$ was found, suggesting that the charge transfer occurs through the organic layers and is not dominated by the charge transfer through defects(Nicholson 1965, Morita and Kimura 2003). These results clearly indicate that the observed redox process is caused by the electron transfer from the ferrocene moiety to GaN through the peptide helix. One should note, that $NaClO_4$ is more commonly used for such experiments, as Kimura et al. previously reported for similar peptides grafted on Au surfaces (Morita and Kimura 2003). Na_2SO_4 was used in this study in order to minimize any potential risk to damage the Ohmic contacts of GaN electrodes. Since ferrocenium ions are partially active in Na_2SO_4, as Valincius et al reported (Valincius 2004) and only the electron transfer mediated by "active" ferrocenes are detected by the following chronoamperometric measurements, the electrolyte can be substituted in this manner.

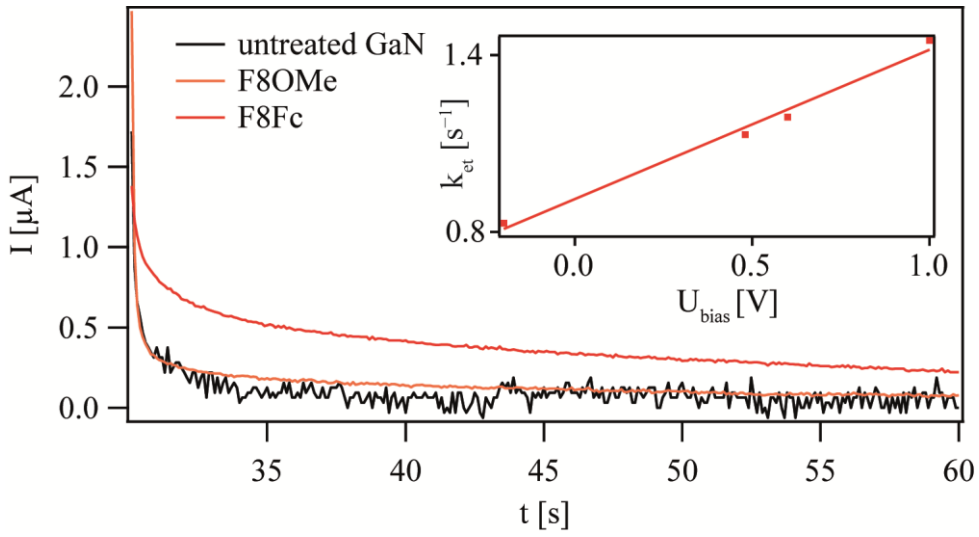

Figure 4.6: *Chronoamperometry of untreated GaN (black), F8OMe (orange) and F8Fc (red) coated GaN, recorded at the overpotential 480 mV. The dependency of electron transfer rate k_{et} of F8Fc-coated GaN on the overpotential U_{bias} is depicted in the inset.*

The rate of electron transfer through the peptide layer was examined by chronoampreometry. In Figure 4.6 the current responses to an overpotential step of U_{bias} = 480 mV at t = 30 s is shown. The current responses of untreated (black) and F8OMe coated (orange) GaN electrodes were almost identical. For both samples an exponential current decay that reached the baseline within the first few second was observed with a characteristic rate constant of k = 6.0 ± 0.3 s^{-1}. Since the decay shows a dependency of $(t) \propto e^{-kt}$, the observed current response is purely capacitive. This seems plausible, as the CV spectra of both samples show no distinct reductive or oxidative current response at the applied U_{bias} range. For ferrocene-functionalized F8Fc (red) in contrast, a much slower current decay was observed with some saturation current level of I > 0.2 µA remaining even after 30 s. This current response could be well described by the Cottrell equation,

$$I(t) = nFAc_0\sqrt{\frac{D}{\pi t}} \tag{2.59}$$

confirming the faradaic redox process occurring in the presence of the ferrocene moiety. A six times smaller electron transfer rate constant k_{et} = 1.1 s^{-1} was obtained, further indicating a sustained electron transfer due to the ferrocene redox reaction. The transfer rate showed a linear dependency on the applied bias potential (inset Figure 4.6), allowing the determination of the the standard electron transfer rate constant k_{et}^{0} = 0.91 s^{-1} by linear extrapolation to U_{bias} = 0 V. Similar transfer rates of k_{et}^{0} = 0.68 s^{-1} (Morita and Kimura 2003) were reported by Morita and Kimura for longer peptides with16 amino

acids on Au surfaces. The obtained electron transfer rate suggests that the transfer follows an inelastic hopping mechanism along the peptide helix, since it is several orders of magnitude larger than the rate calculated for the supercharge mechanism (Immergut 1989).

4.5 Carrier Density Modulation by Macromolecular Dipole Moment in GaN/AlGaN/GaN HEMT Structures

To demonstrate the potential of helical peptides towards the modulation of the channel current in the 2DEGs confined in GaN/AlGaN/GaN heterostructures and further quantify the effect of the peptide deposition on surface potentials, the helical peptides were deposited on the gate region of HEMTs based on GaN/AlGaN/GaN heterostructures (Figure 4.1). The changes in the electrical *I-V* characteristics were analyzed before and after the chemical functionalization by first measuring the HEMT transfer characteristics as the gate voltage (V_G) dependent drain-source current (I_{DS}) at a constant source-drain voltage V_{DS} = 0.3 V (Figure 4.7). The measurements were performed in HEPES buffer under constant flow of 2 ml/min. It should be noted, that measurements for F8OME and F8Fc coated heterostructures was performed on two transistor chips cut from the same wafer, while a chip from a different wafer was used for the Boc8F coated HEMT. The I_{DS}-V_G curves of two untreated GaN chips produced from the same wafer were almost identical (see Supplementary Information section 9.1.3) and showed no remarkable changes from the amonosilanization with APTES. Since the HEMTs had to be dis- and remounted for each chemical functionalization, the reproducibility of the measured *I-V* characteristics was confirmed by repetitive dismounting/mounting cycles prior to the grafting of organic layers. Almost no changes in the *I-V* characteristics were found, with an error range of ΔV_{th} = ± 17 mV and ΔI_{DS} = ± 1.7 µA from repeated installation cycles of the HEMT chip (see Supplementary Information 9.1.3). The changes caused by APTES deposition are within this error range.

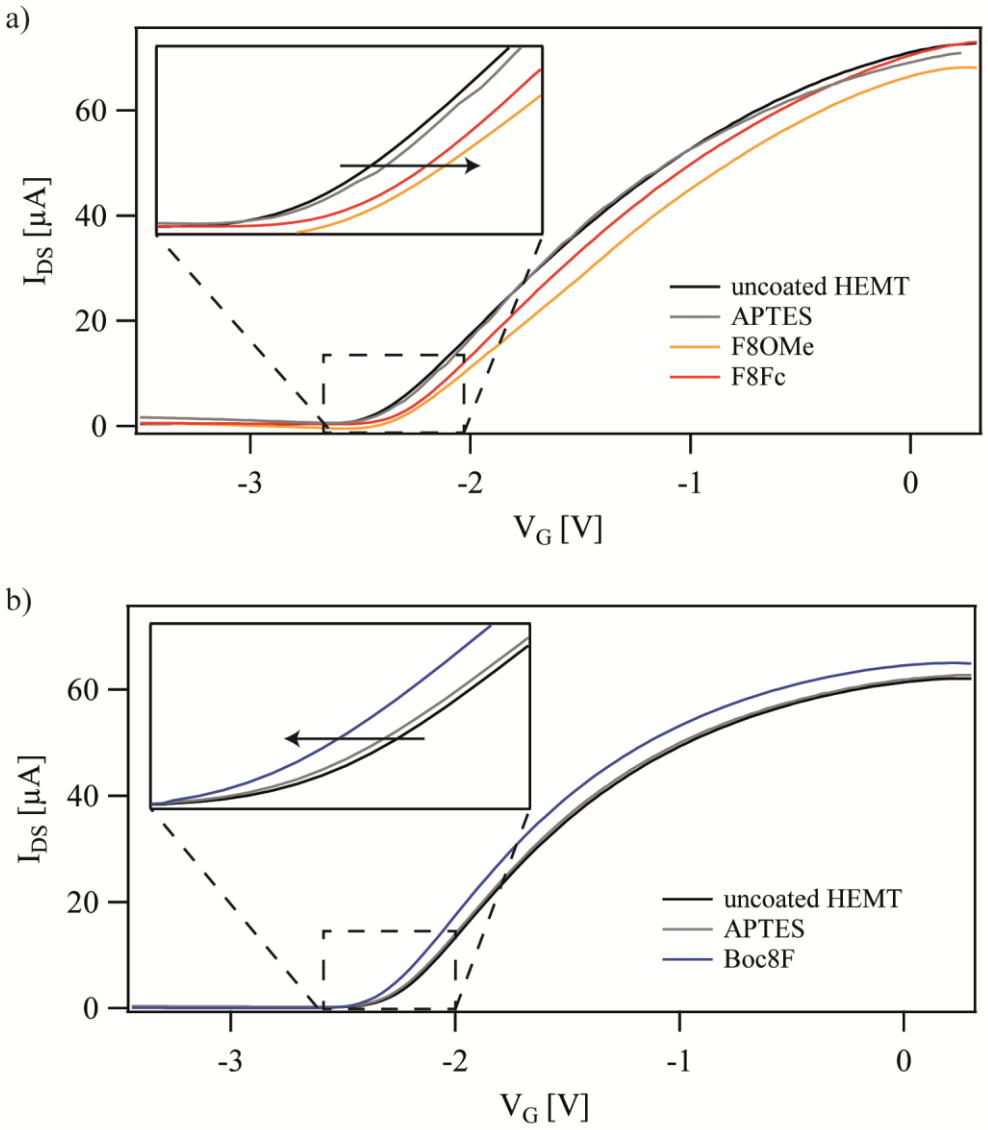

Table a)

coating	V_{th} [V]	g [µS]
Untreated GaN	– 2.54	35.4
APTES	– 2.53	35.5
F8OMe	– 2.38	35.0
F8Fc	– 2.40	36.9

Table b)

coating	V_{th} [V]	g [µS]
Untreated GaN	– 2.46	36.7
APTES	– 2.47	36.5
Boc8F	– 2.60	36.7

Figure 4.7: *(a) Transfer (I_{DS}-V_G) curves from two HEMT chips produced from Wafer 1 measured at V_{DS} = 0.3 V, with the untreated HEMT (black), APTES (grey), F8OMe (orange) and F8Fc (red) grafted HEMT. The transfer curves of the untreated HEMT (black) and APTES-coated HEMT (grey) were identical between two chips, confirming the excellent reproducibility. (b) I_{DS}-V_G curves from one HEMT chip from Wafer 2 measured at V_{DS} = 0.3 V, with the untreated HEMT (black), APTES (grey) and Boc8F (blue) grafted HEMT. Threshold voltage V_{th} and transconductance g values were obtained from linear regression at V_G = – 1.50 ± 0.25 V.*

The deposition of F8OMe and F8Fc resulted in a more pronounced change in the I_{DS}-V_G curves (Figure 4.7a). Irrespective of the presence or absence of peptide layers the linear region of the I_{SD}-V_G curves yields the transconductance of the 2DEG channel of $g_m = \left[\partial I_{SD}/\partial V_g\right]_{V_{SD}=const} = 35 - 37\mu S$. As summarized in Table a) in Figure 4.7, the threshold voltage V_{th}, obtained from the linear extrapolation of I_{DS}-V_G curves at V_G = – 1.50 ± 0.25 V to I_{DS} = 0, exhibited pronounced changes in V_{th} from functionalization with F8OMe and F8Fc to $V_{th(F8OMe)}$ = – 2.38 V and $V_{th(F8Fc)}$ = – 2.40 V respectively. It is noteworthy that the deposition of two peptides possessing the same macromolecular dipole moments pointing towards GaN led to comparable shifts in the threshold voltage, ΔV_{th} = 140 – 160 mV with no remarkable change in the channel transconductance. Figure 4.7b represents the results from a different chip cut a second wafer that was grafted with the Boc8F peptide. Though the absolute levels of g_m and V_{th} of bare GaN showed a deviation from those presented in Figure 4.7a, the obtained results show a clear trend. The functionalization with Boc8F, carrying an opposite dipole moment from F8OMe and F8Fc, resulted in a "decrease" in the threshold voltage of ΔV_{th} = – 140 mV without changing the slope of I_{DS}-V_G curves (Table b, Figure 4.7). These data clearly indicate that the surface functionalization, especially the deposition of helical peptides carrying macromolecular dipole moments, can be detected using surface sensitive GaN/AlGaN/GaN HEMT structures. The directions of the shift in V_{th} are consistent with the shift of U_{FB} obtained from impedance spectroscopy. The APTES deposition led to a slight increase in U_{FB} and the further functionalization with F8OMe and F8Fc resulted in a more pronounced increase in U_{FB}. In contrast, the deposition of Boc8F resulted in a clear decrease in U_{FB}, while the magnitudes of the changes are comparable between V_{th} and U_{FB}. These results confirm that the surface density and the orientation of peptide helices are comparable to those on bulk GaN electrodes. As determined from the impedance spectra, the dipole moments of F8OMe and F8Fc point towards GaN, while that of Boc8F points the opposite direction.

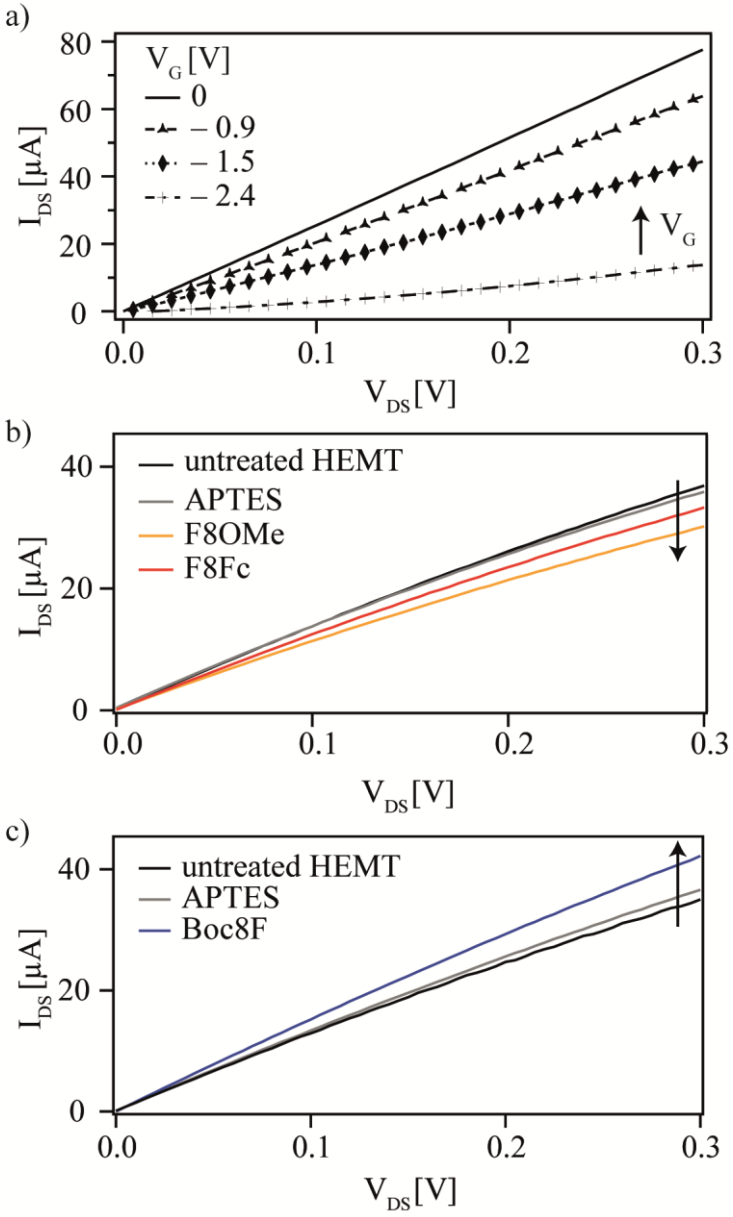

Figure 4.8: *Output (I_{DS}-V_{DS}) curves measured at V_G = – 1.5 V of (a) untreated HEMT from Wafer 1 at various V_G. Output curves of (b) two HEMT chips from Wafer 1, and (c) HEMT chip from Wafer 2 after each functionalization step.*

In the next step, the changes in V_G caused by the deposition of peptide monolayers were determined. To calculate the effective dipole potential generated by each peptide, the Output (I_{DS} -V_{DS}) characteristics of the HEMT structures were measured. Figure 4.8a represents the I_{DS}-V_{DS} characteristics of a bare HEMT chip measured at different V_G. The deposition of F8OMe and F8Fc caused decreases in I_{DS}, which can be translated into the decrease in surface potential V_G (Figure 4.8b), while the deposition of Boc8F resulted in a shift in the opposite direction (Figure 4.8c). These measurements were performed at V_G = – 1.5 V, where all the samples exhibited the maximum transconductance and thus

maximum sensitivity. The calibration with the I_{DS}-V_{DS} curves of bare HEMT at various V_G enables one to estimate the apparent change in V_G (ΔV_G) corresponding to each peptide to $\Delta V_{G(F8OMe)} = -0.29$ V, $\Delta V_{G(F8Fc)} = -0.16$ V, and $\Delta V_{G(Boc8F)} = +0.28$ V. The magnitude of these changes agrees well with those determined for U_{FB} (Table 4.3). The changes have opposite signs, since V_G is applied from the gate (Ag/AgCl) to the source (GaN/AlGaN/GaN), while U_{bias} is applied from the working electrode (GaN) to the reference electrode (Ag/AgCl). A much higher sensitivity to the effective potential applied by the peptide dipole moment can be obtained from these measurements, as shown by the higher accuracy of the fit for the determination of V_{th} ($r^2 = 0.995$) compared to U_{FB} in Mott-Shottky plots ($r^2 = 0.831$), confirming that the modulation of the electronic band profile by macromolecular dipoles can be detected by GaN HEMT with a high sensitivity. The effective dipole potentials exerted from the peptide helix on the HEMT structure can also be estimated from the threshold voltage shifts in I_{DS}-V_G curves. However, the experiments at different V_G would provide with less reliable data because the HEMT is operating under different working points. The influence of ferrocene moieties could further not be discerned from the *I–V* characteristics, which could be attributed to a faster carrier relaxation time in the 2DEG channel of the HEMT than electron transfer rate ($k_{et}^{\,0} = 0.91\ s^{-1}$).

The dipole potential generated by the deposition of peptides ΔV_G calculated from Figure 4.8b and Figure 4.8c follows the Helmholtz equation and can be given as a function of the macromolecular dipole moment ρ of a helical peptide:

$$\Delta V_G = \frac{\rho}{\varepsilon \varepsilon_{0A}} \cos(\theta) \tag{4.2}$$

where ε is the dielectric constant of peptide, ε_0 the permittivity of vacuum, A the average area per molecule, and θ the tilt angle between the helical axis and surface normal. The tilt angle was approximated by the ratio between the peptide thickness calculated from XRR d and the estimated length of the molecule L; $\cos(\theta) = d/L$. The dielectric constant of the peptide layer ε was calculated from the experimentally determined C_{pep}, d, and the electrode area $A_{ele} = 0.5\ cm^2$:

$$\varepsilon = \frac{C_{pep} d}{A_{ele} \varepsilon_0} \tag{4.3}$$

With the obtained capacitance values of the peptide layer $C_{pep(F8OMe)} = 1.4\ \mu F cm^{-2}$, $C_{pep(Boc8F)} = 1.5\ \mu F cm^{-2}$, and $C_{pep(F8Fc)} = 1.2\ \mu F cm^{-2}$, the dielectric constants of peptides were determined to $\varepsilon_{F8OMe} = 5.2$, $\varepsilon_{Boc8F} = 5.9$, and $\varepsilon_{F8Fc} = 4.0$. Since the peptides in this study are immersed in bulk water ($\varepsilon = 80$), the slightly larger dielectric constants compared to "dry" peptides in air $\varepsilon_{dry} = 3.5$ seem reasonable (Fujita, Kimura et al 1995),

possibly due to the water incorporation into the peptide layer. From these values, the macromolecular dipole moments exerted by the peptides can finally be calculated to $\rho_{F8OMe} = -8.1$ D, $\rho_{Boc8F} = 7.1$ D, and $\rho_{F8Fc} = -5.5$ D. The obtained values seem smaller than those expected from the dipole per peptide bond in vacuum (3.45 D) (Sengupta 2005), which can also be attributed to the screening effect by aqueous media and the tilted conformation of the peptide layer. Interestingly a larger ΔV_{th} from peptide deposition on the GaN/AlGaN/GaN heterostructure was achieved compared to a peptide with twice as many repeat units on GaAs (Kaindl 2010), demonstrating the excellent sensitivity of the GaN heterostructures.

4.6 Summary

The flexible modulation of the surface band profiles was achieved via macromolecular dipole moments by covalent coupling of bio-inspired, but non-biological peptide helices on GaN semiconductor and heterostructures surfaces. After the formation of well defined peptide monolayers was confirmed on GaN by AFM, XPS, and XRR, it was shown that the peptide macromolecular dipoles alter the flat band potentials by means of electrochemical impedance spectroscopy. The sign of the alterations could be controlled by the sign of dipole moments, determined by the selective termination of either N- or C-terminal with aldehyde moieties. It was further demonstrated by using a peptide helix terminated with a ferrocene moiety that electron transfer along the peptide helix can occur via inelastic hopping. Without ferrocene chronoamperometry measurements revealed that the current response is purely capacitive. The functionalization protocol transferred from GaN to GaN/AlGaN/GaN HEMT structures demonstrated that the macromolecular dipole potentials exerted by helical peptides modulate the carrier density in the polarization-induced two-dimensional electron gas, whereas a stronger alteration of the carrier density was achieved as for other semiconductor materials. These results suggested that the surface functionalization with bio-inspired peptide helices could have a large potential towards the macromolecular dipole engineering of wide band gap GaN semiconductors, possibly exceeding the limits of inorganic doping.

5. Supported Lipid Mono and Bilayers on GaN/AlGaN/GaN HEMT Structures

5.1 Introduction

Functional immobilization of biological systems on solid semiconductor based devices is an interdisciplinary challenge for the creation of novel hybrid sensor materials for numerous scientific and technological applications, such as the understanding of basic cell adhesion principles, signal transduction, high throughput screening assays and protein/DNA senor chips. An important step towards such hybrid systems is the combination of hard solids and soft biological matters by functionalization of solid surfaces with organic, biocompatible materials. The use of semiconductors as solid substrate material is advantageous for such hybrid systems, as it allows for a tracer less opto- electric sensing at low noise levels. Despite the successful demonstrations of several novel sensor platforms (Cui et al. 2001, Steinhoff, Hermann *et al.* 2003, Luber 2004, Steinhoff, Baur et al. 2005) and high sensitivity to detect traces of the analyte, only their presence could be detected in most cases. Quantitative sensing remains to be difficult, as control of the surface chemistry, i.e. lateral density, conformation, and orientation of functional molecules on the surface remains a major challenge. Based on so-called "supported membrane concepts" (Sackmann 1996) proposed by Tanaka et al., several membrane-based biosensors on bulk GaAs and ITO semiconductor electrodes were developed (Purrucker et al. 2001, Hillebrandt et al. 1999 and 2002, Gassull 2008) using ultrathin polymer supports, based on regenerated cellulose, to fine-tune membrane-substrate contacts (Tanaka and Sackmann 2005 and 2006). One strategy to achieve this is the use of phospholipid membranes incorporating specific anchor lipids (e.g. DGS-NTA), whose lateral distances can be controlled with nm accuracy by variation of its concentration. This approach ensures a natural environment for the non-denaturing immobilization of proteins in well-defined orientation (Sackmann 1996, Sackmann and Tanaka 2000). The combination of protein-anchored lipid membranes with sensor materials opens a wide range of biological applications. Due to its excellent chemical/electrochemical stability and high carrier density, wide band gap GaN/AlGaN/GaN HEMT structures offer high sensitivity in variations of surface potential and are thus a promising sensor material. Following the work of Frenkel et al. 2014 on bulk GaN electrodes in chapter 5.2, a complex supported lipid monolayer system for biosensoric applications was developed using phospholipid monolayers deposited on negatively doped GaN/AlGaN/GaN HEMT structures funcionalized with hydrophobic octadecyltrimethylsilane (ODTMS) monolayers (Figure 5.1a). Chelator lipids containing nitrilo-triaceticacid (NTA) headgroups were incorporated into the supported monolayer in

defined ratios to reversibly modify the membrane surface charge density. The NTA-lipids form chelator complexes with divalent metal ions (e.g. Ni^{2+}) and allow the coupling of recombinant proteins over histidine tags, such as green fluorescence proteins (GFP), allowing the reversible and highly sensitive detection of protein binding by this sensor platform.

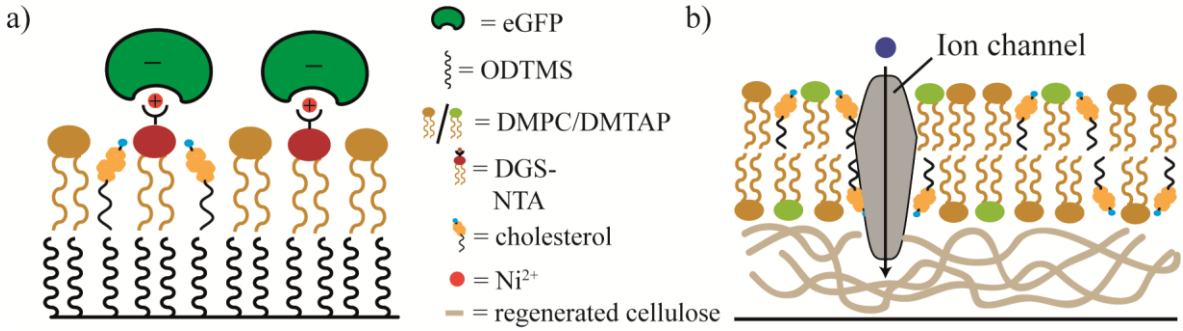

Figure 5.1: *Schematic representation of (a) reversible couping of charged proteins on supported monolayer membrane containing NTA chelator lipids and (b) polymer supported lipid bilayer membrane.*

Another strategy for modeling the interactions between cells and tissues, mediated by short- and long-range forces (e.g.van der Waals forces, electrostatic forces, steric or entropic forces, and hydration forces) (Derjaguin and Churaev 1987, Israelachvili 1985) is the design of biomimetic molecular assemblies with a reduced number of components to create simple physical models. Here, the deposition of model cell membranes and artificial extracellular matrix (ECM) onto planar substrates is a powerful strategy to quantitatively study their functions. The use of artificial ECM supports not only enables the accommodation of integral- and trans-membrane proteins without denaturation on solid substrates but creates hydrating pathways for material transport as well. Such supports further allow for the formation of highly resistive membranes, necessary to generate the ionic potential gradients occurring across natural cell membrane in order to investigate functions of integral proteins, such as ion channels. Various studies demonstrated that natural extracellular matrix materials like laminin, fibronectin, and hyaluronic acid (Fromherz 1991, Comper 1996) can accommodate cells and natural membranes on solid substrates without inducing apoptosis or denaturing of proteins. However, the physical properties of these natural macromolecules are not well defined. As an alternative, regenerated thin films of cellulose can be fabricated with nm accuracy in thickness and very small topographic roughness by deposition of synthetically modified cellulose and subsequent chemical regeneration to the original cellulose (Rehfeldt, Tanaka 2003). This interlayer has been reported to accommodate artificial and native cell membranes without notable defects (Gönnenwein et al 2004, Tanaka 2001,

Tanaka 2004). Chapter 5.3 details the use of regenerated cellulose interlayers on GAN/AlGaN/GaN HEMT structures as a sensor platform for the label free detection of membrane formation (Figure 5.1b).

5.2 Reversible Membrane Charge Sensor based on Supported Lipid Monolayers on GaN HEMTs

5.2.1 Monolayer Formation on ODTMS Support

To achieve a well defined formation of the above mentioned monolayer system, an ODTMS support on GaN is employed to provide a hydrophobic interface for lipid monolayer deposition. High hydrophobic behavior of the ODTMS coated GaN was confirmed for all samples by contact angle measurements (Figure 5.2a and b), where a water contact angle $\theta > 90°$ was obtained. A low rms roughness ($\sigma < 1$ nm) of the ODTMS coated GaN surface was further confirmed by AFM measurements (Figure 5.2d), determined from a 10 µm x 10 µm scanning area in contact mode, enabling the deposition of a lipid monolayer with low defect density.

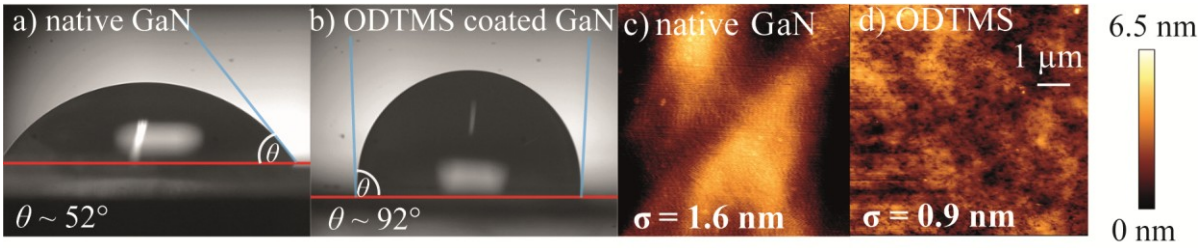

Figure 5.2: *Sessile drop contact angle of GaN (a) before and (b) after silanization with ODTMS. 10 µm x 10 µm topographic image of (c) native and (d) ODTMS coated GaN.*

In a next step the monolayer membrane formation and binding of his-eGFP proteins was investigated on a cover glass substrate by fluorescence microscopy by vesicle fusion of a DMPC/cholesterol/DGS-NTA lipid mixture of 63/35/2 mol% and 64.5/35/0.5 mol%, containing 0.2 mol% texas-red-DHPE respectively. Protein binding onto the membrane was tested for two DGS-NTA chelator lipid concentrations (0.5 mol% and 2 mol%). Assuming the molecular area of one lipid of 65 Å^2, these concentrations correspond to an intermolecular distance of d = 9 nm and 5.7 nm between the DGS-NTA lipids.. At 2 mol% DGS-NTA, this distance matches the average diameter of his-eGFP of d = 5.2 nm, determined by dynamic light scattering measurements. Thus, a complete coverage of the lipid monolayer with GFP can be achieved. Figure 5.3a shows the monolayer containing 2 mol% DGS-NTA prior to protein binding. Few defects and spots with higher intensity could be observed in the texas-red stained monolayer. This could be caused by undulations in the ODTMS support observed in AFM measurements (Figure 5.2c), causing local differences in the monolayer formation.

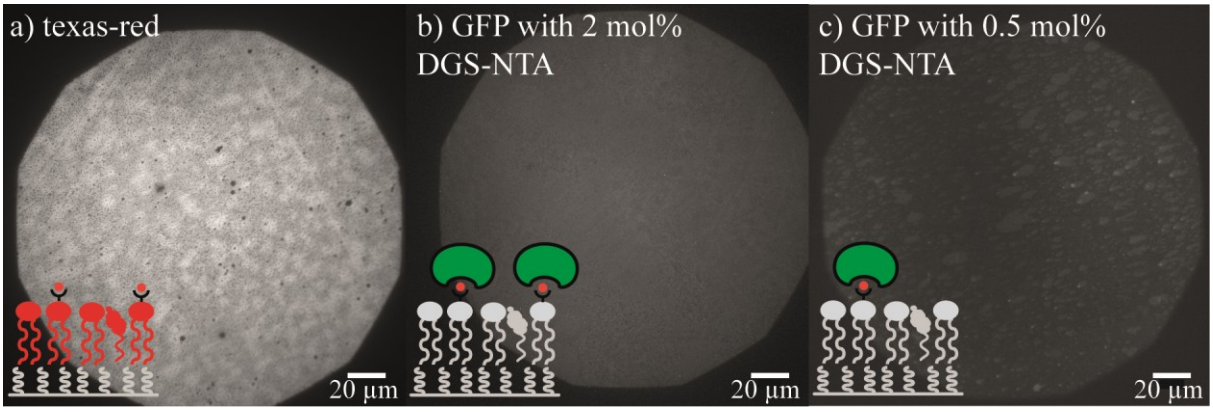

Figure 5.3: *Fluorescence images of a lipid monolayer of (a) DMPC/cholesterol/DGS-NTA (63/35/2 mol%) containing 0.2 mol% texas-red-DHPE, (b) DMPC/cholesterol/DGS-NTA (63/35/2 mol%) and (c) DMPC/cholesterol/DGS-NTA (64.5/35/0.5 mol%) after GFP binding.*

Nonetheless, after protein binding for 1 h with 0.25 µg/ml his-eGFP, a more homogeneous distribution in the GFP fluorescence for 2 mol% DGS-NTA was observed. As expected from the higher intermolecular distance and thus lower density of the DGS-NTA binding sites, more defects and inhomogeneities as well as lower fluorescence intensity was observed for 0.5 mol% DGS-NTA. The distribution of the GFP fluorescence signal though still suggests a high enough density to influence the HEMT surface potential due to GFP binding in a significant manner. The diffusion and self healing capability of these monolayer membranes was confirmed in previous accounts (Frenkel 2014 and 2015), yielding a mobile fraction of 88 % and the lateral diffusion coefficient of D = 0.77 $\mu m^2 s^{-1}$, which is comparable to values of lipid monolayers on other hydrophobic polymer supports (D = 1.0 - 1.5 $\mu m^2 s^{-1}$) (Sigl, Brink *et al.* 1997).

The lipid monolayer formation was further examined by high specular X-ray reflectivity (XRR) after vesicle fusion of a 63/35/2 mol% DMPC/cholesterol/DGS-NTA mixture on ODTMS coated native Si as well. Here, the thickness d, scattering length density SLD and roughness σ were determined prior to protein binding by employing a four slab model, representing the lipid headgroups, the lipid hydrocarbon chains, the ODTMS silane layer and silicon oxide layer. An additional slab representing the layer of bound protein was used for the reflectivity curve measured after 1 h incubation with 0.25 µM his-eGFP. The appearance of the board peak at $q_z \sim 0.3$ $Å^{-1}$ in the reflectivity graph prior to protein binding (Figure 5.4a, red circles) confirmed the formation of the monolayer on a larger scale (~ 1-2 mm^2).

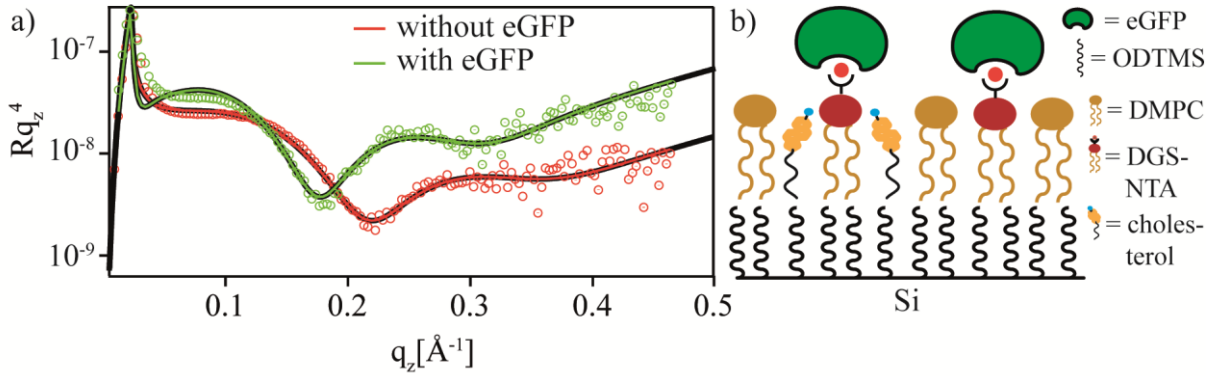

Figure 5.4: *(a) Reflectivity graphs normalized by q_z^4 of a DMPC/cholesterol/DGS-NTA (63/35/2 mol%) monolayer on ODTMS coated Si measured in HEPES buffer. The solid lines represent the fitting result (χ^2 = 0.015) of the experimental data of the monolayer before (red circles) and after eGFP binding (green circles). (b) Schematic representation of the layered structure.*

The obtained results for *SLD* and σ (Table 5.1) of the lipid head groups and hydrocarbon chains agree well with the results of a similar membrane, using 5 mol% DGS-NTA (Frenkel 2015). The combined thickness of the ODTMS layer and the lipid hydrocarbon chains as well was similar to the previously obtained results. Only the thickness of the lipid head groups was slightly smaller. Since the NTA-lipids posess a larger head group than other pohospholipids, the lower amount of NTA-lipids used in this monolayer could have caused the smaller observed thickness. The similar *SLD* however suggests that the formation of a well defined and dense monolayer could be achieved.

Table 5.1: *Best fit parameters (χ^2 = 0.010) of the 2 mol% DGS-NTA containing lipid monolayer on ODTMS coated Si in HEPES buffer.*

layer	**prior to eGFP binding**			**after eGFP binding**		
	d [Å]	SLD [10^{-6} Å^{-2}]	σ [Å]	d [Å]	SLD[10^{-6} Å^{-2}]	σ[Å]
his-eGFP	-	-	-	51	11.6	49
lipid head group	8.7	10.7	5.0	8.5	10.6	3.3
lipid alkyl chains	14.4	7.9	4.7	15.9	7.1	3.3
ODTMS	16.1	8.3	4.3	16.7	8.3	3.7
SiO_2	9.4	18.6	4.6	9.1	18.6	4.4

Upon protein binding the minimum position in the reflectivity graphs shifts from q_z ~ 0.21 Å^{-1} (red curve) to q_z ~ 0.18 Å^{-1} (green curve), indicating an increase in the total thickness due to the protein adsorption. As demonstrated by the obtained best fit parameters in Table 5.1, no remarkable changes in the thickness, *SLD*, and interface roughness of the lipid monolayer were caused by the complexation of eGFP, indicating that only adsorption of GFP onto the monolayer occurs. The obtained thickness of the eGFP layer of 51 Å agrees well with the expected value of around d ~ 50 Å for one GFP

molecule, determined by dynamic light scattering measurements. With this and the similar obtained *SLD* (SLD_{GFP} = 11.6·10^{-6} Å^{-2}) to the value calculated from the protein sequence and its molecular weight (*SLD* = 12.4·10^{-6} Å^{-2}), an almost saturated coverage of the lipid monolayer with eGFP can be confirmed. The large GFP interface roughness of 49 Å however suggests that the eGFP "layer" is not fully saturated. Analogous measurements on undoped GaN were not conclusive, since the lipid interface becomes too diffuse due to its larger rms roughness compared to Si.

5.2.2 Modulation of HEMT I-V Characteristics by Reversible Monolayer Charging and Recombinant Protein Binding

The deposition protocols tested on bulk GaN and Si substrates were transferred to the GaN/AlGaN/GaN HEMT structures (Figure 2.12) in order to explore the potential of this system for the recognition of processes occurring at the monolayer surface. Variation in membrane charges due to binding of charged proteins changes surface potential, which in turn incurs changes in the transistor carrier density and thus, its performance. These changes are monitored and quantified by recording the transistor transfer curves (I_{DS} vs. V_G) and output curves (I_{DS} vs. V_{DS}) at different charge states of the lipid monolayer. DGS-NTA groups in the deposited monolayers were reversibly charged and de-charged using Ni-buffer (2 mM $NiCl_2$) and EDTA-buffer (100 mM EDTA). An octahedral chelator complex is formed by the NTA groups with Ni^{2+} or other divalent cations, where the loading and unloading of the monolayer with Ni^{2+} causes a change in the molecular net charge from by 1 e^- (Beauchamp et al. 1969, Hillebrandt et al. 2002). Protein binding to the membrane was achieved by using eGFP with his-tags that further bind specifically to the Ni^{2+} in the Ni-NTA complex by replacing its H_2O ligands (Schmitt et al. 1994). This further causes changes in the monolayer charge, since the isoelectric point of his-eGFP is ~ 4.8 (Tanaka et al. 2007) and thus GFP is negatively charged at pH = 7.5. The immobilization of GFP onto the monolayer can then be broken by extraction and complexation of the bound Ni^{2+} (unloading) by EDTA (Figure 5.5).

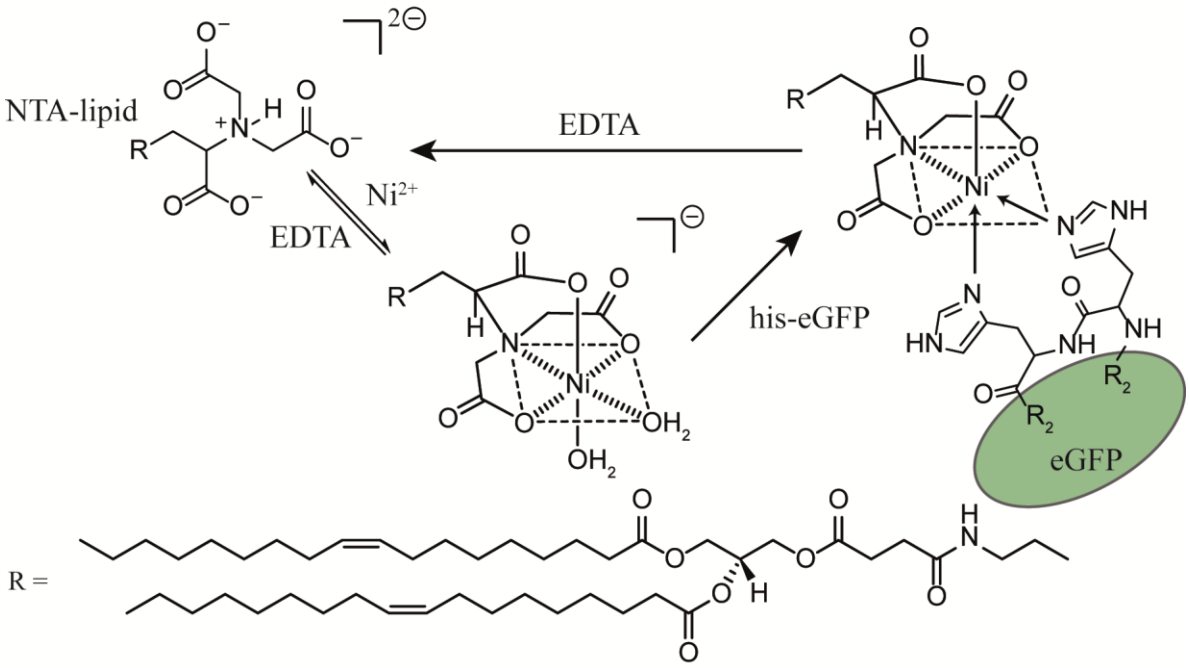

Figure 5.5: *Schematic flow of the loading/unloading of NTA lipids with Ni^{2+} and his-eGFP.*

The measurements were first performed with 2mol % DGS-NTA, since at 0.5 mol% DGS-NTA the eGFP-loaded and unloaded states were not distinguishable in previous repots (Frenkel 2014 and 2015). In Figure 5.6 the *I-V* characteristics of the DMPC/cholesterol/DGS-NTA (63/35/2 mol%) monolayer are presented at Ni-loaded (red), eGFP-loaded (green) and unloaded (blue) states. Prior to the first measurement the lipid monolayer was rinsed 15 min with Ni-buffer to ensure a full complexation of the DGS-NTA groups. All measurement steps were then performed after rinsing 15 min with HEPES buffer to avoid changes in surface potential due to different ion concentration in the buffers.

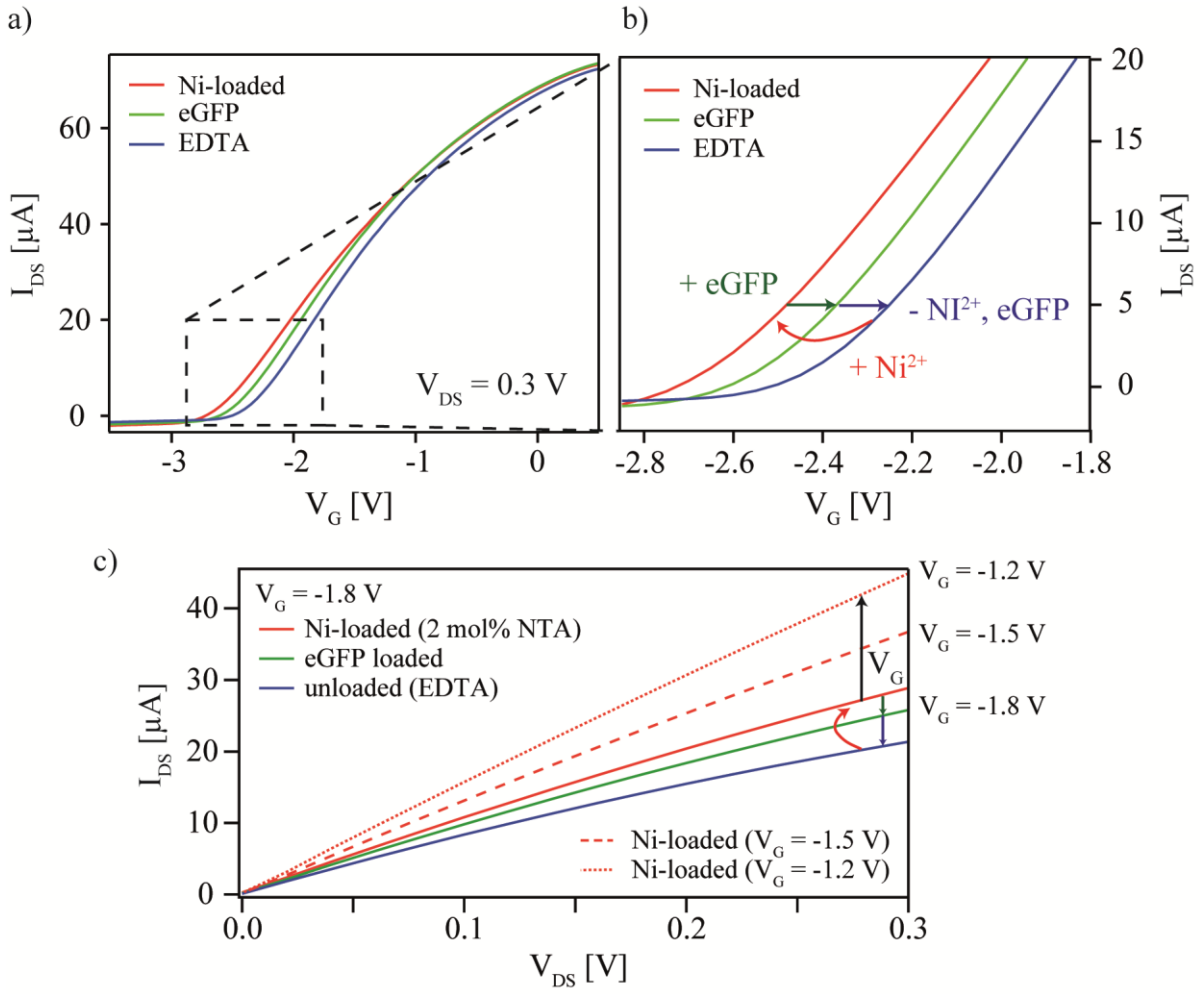

Figure 5.6: *(a) Transfer curves (I_{DS} vs. V_G) of the DMPC/cholesterol/DGS-NTA (63/35/2 mol%) monolayer on ODTMS coated HEMT at unloaded (blue), Ni^{2+}-loaded (red) and eGFP-loaded (green) states. (b) Magnification of the threshold region in the transfer curves. (c) Output curves (I_{DS} vs. V_{DS}) of the lipid monolayer at V_G = – 1.8 V for the different monolayer charge states and various applied gate voltages for Ni-loaded state.*

First, transfer curves of the HEMT were measured at constant V_{DS} of 0.3 V for the different monolayer charge states (Figure 5.6a and b). Threshold voltage V_{th} and transconductance g were determined from these curves by linear regression at V_G = – 2.1 V to V_G = – 1.8 V and are summarized in Table 5.2. At the Ni-loaded state a threshold voltage of $V_{th, Ni}$ = – 2.59 V was determined. After injection of GFP (0.25 µg/ml) for three hours at constant flow of 0.5 ml/min a distinct shift in threshold voltage to $V_{th, GFP}$ = – 2.48 V; $\Delta V_{th, GFP}$ = 0.11 V was observed, which increased further to $V_{th, EDTA}$ = – 2.37 V; $\Delta V_{th, EDTA}$ = 0.22 V after unloading the monolayer with EDTA (100 mM). An almost complete recharging of the NTA groups in lipid monolayer with Ni^{2+} could be further achieved, confirming the reproducibility of the monolayer charging (see Supplementary Information section 9.1.3). For all monolayer charge states similar g values were found, indicating that the resistance of the monolayer system stayed constant over duration of the

measurements, with no degradation of the lipid monolayer discerned. The change in V_{th} from the Ni-loaded state to the unloaded state, $\Delta V_{th,\,EDTA}$ = 0.22 V, can be understood by the change of net charges in NTA group. At the unloaded state and assuming complete dissociation the NTA-group carries a net charge of – 2 due to its free carbonate moieties. In the Ni-loaded state the net charge of the Ni-complex formed is – 1. Thus the surface potential of the lipid monolayer is negatively charged when unloading with EDTA, causing the change in carrier concentration, and with that V_{th} in the GaN HEMT. With the binding of eGFP though, the Ni-complex carries no net charge, but a weaker negative charging of the surface potential is still observed. This is attributed to the negative net charge of carried by eGFP itself at pH = 7.5.

Table 5.2: *Summary of threshold voltage V_{th} and transconductance g values at different monolayer charge states using 2 mol% DGS-NTA. The values were determined from linear regression of the transfer curves between V_G = – 2.2 and – 1.8 V.*

state	V_{th} [V]	g [µS]
Ni-loaded	– 2.59	36.1
eGFP loaded	– 2.48	37.4
unloaded (EDTA)	– 2.37	36.9

The changes in apparent V_G induced by loading and unloading of the membrane were determined from the transistor the output curves (I_{DS} vs. V_{DS}). In Figure 5.6c the output curves of the transistor with Ni-loaded monolayer are shown for different applied gate potentials V_G (red curves). Similar to the untreated transistor in Chapter 4 an increase in I_{DS} with increasing V_G was observed. For the eGFP-loaded and unloaded states a decrease in I_{DS} was observed at constant V_G = – 1.8 V, which corresponds to an apparent decrease in V_G of $\Delta V_{G,\,GFP}$ = – 0.1 V and $\Delta V_{G,\,EDTA}$ = – 0.24 V respectively. These values correspond well to the determined shifts in V_{th} determined from the transfer curves. However, the observed shifts were less pronounced than the previously reported shifts in flat band potential U_{fb} for eGFP binding (ΔU_{fb} = 0.44 V) and monolayer unloading (ΔU_{fb} = 0.81 V) determined from impedance measurements on bulk GaN electrodes (Frenkel 2014). This could be caused by the smaller deposition area of the gate region in the HEMT measurements. Still, the changes from the different charge states can be clearly distinguished, show the same tendency and a comparable ratio of the changes between the eGFP-loaded and unloaded state.

5.2.3 Resolution Limit of the Sensor

In the next step the limits of this system to sense changes in the surface charge density were tested by deposition of a monolayer containing 0.5 mol % DGS-NTA chelator lipids. Transfer curves of the monolayer were measured in Ni-loaded (red), eGFP loaded (green) and unloaded (blue) states at constant V_{DS} of 0.3 V as well. As expected, the shifts of the curves from changing the monolayer charge states observed in Figure 5.7a and b were not as pronounced as for the 2 mol% DGS-NTA containing monolayer. The lower amount of charged NTA groups in the monolayer express a reduced charge density at the HEMT surface. Thus, a reduced change in the surface potential upon loading and unloading is generated, leading to a reduced modulation of carrier density and change in V_{th} in the GaN HEMT.

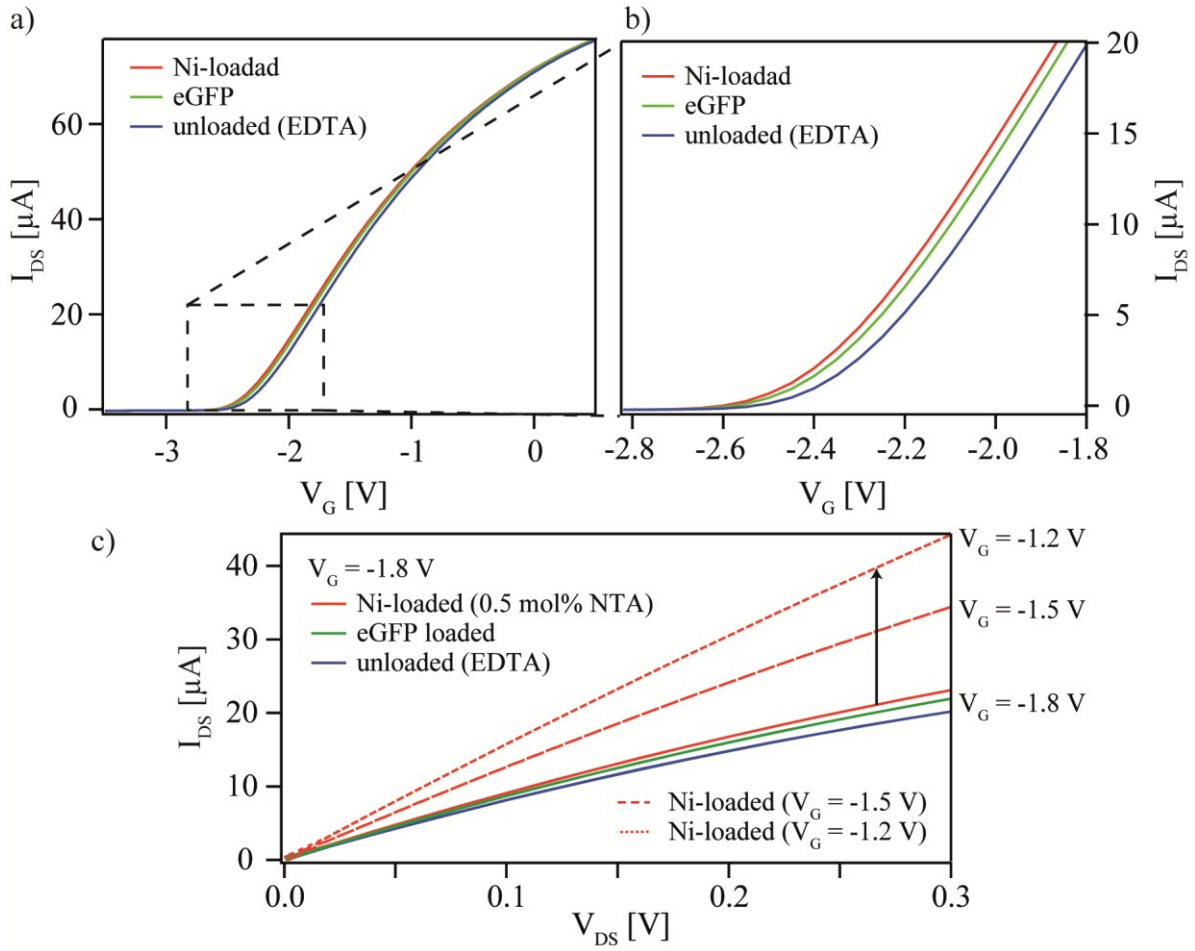

Figure 5.7: *(a) Transfer curves (I_{DS} vs. V_G) of the DMPC/cholesterol/DGS-NTA (64.5/35/0.5 mol%) monolayer on ODTMS coated HEMT at unloaded (blue), Ni^{2+}-loaded (red) and eGFP-loaded (green) states. (b) Magnification of the threshold region in the transfer curves. (c) Output curves (I_{DS} vs. V_{DS}) of the lipid monolayer at V_G = – 1.8 V for the different monolayer charge states and various applied gate voltages for Ni-loaded state.*

The changes in V_{th} and g upon protein binding and unloading of the monolayer with 0.5 mol% DGS-NTA were determined by linear regression at same V_G region (from V_G = – 2.1 V to V_G = – 1.8 V) as for the 2 mol% DGS-NTA containing monolayer (Table 5.3). The addition of eGFP over three hours at constant flow of 0.5 ml/min led to a slight shift in V_{th}; $\Delta V_{th,\ GFP}$ = 0.03 V from the Ni-loaded state. This change however is near the resolution limit of the HEMT determined from the variance in *I-V* characteristics (ΔV_{th} = 0.017 V) observed after repeated installations of the same transistor chip in the flow chamber (see Supplementary Information section 9.1.3), but could still be distinguished. The shift after unloading with EDTA; $\Delta V_{th,\ EDTA}$ = 0.08 V on the other hand is clearly discernible, showing that the change of the molecular net charge of $1e^-$ between Ni-loaded and unloaded states can be clearly determined at low charge densities. Further, no changes in transconductance g at the different monolayer charge states were determined as well (Table 5.3).

Table 5.3: *Summary of threshold voltage V_{th} and transconductance g values at different monolayer charge states using 0.5 mol% DGS-NTA. The values were determined from linear regression of the transfer curves between V_G = – 2.2 and – 1.8 V.*

state	V_{th} [V]	g [µS]
Ni-loaded	– 2.37	39.9
eGFP loaded	– 2.34	40.1
unloaded (EDTA)	– 2.29	39.9

As shown in Figure 5.7c, a decrease in I_{DS} state (red) upon protein docking (green) and Ni-unloading (blue) of the monolayer from the Ni-loaded state was observed. From this decrease at V_{DS} = 0.3 V the apparent change in V_G induced by the change in surface potential between the different monolayer charge states was determined to Delta $\Delta V_{G,\ GFP}$ = – 32 mV and $\Delta V_{G,\ EDTA}$ = – 77 mV EDTA after protein docking and unloading of Ni^{2+} respectively. These shifts were again similar to the determined $\Delta V_{th.}$ Here, the shift after unloading is almost two times larger than after eGFP binding. This trend was similarly observed for the 2 mol% DGS-NTA containing lipid monolayer, suggesting a good stability and repeatability of these measurements even at the low membrane charge density from 0.5 mol % DGS-NTA.

With an assumed molecular area per lipid of 0.65 nm^2 in the fluid phase (Lantzsch et al. 1996) and the amount of charged NTA lipids in the monolayer, the sensitivity of the HEMT to changes in surface charge density can be determined. In case of the monolayer incorporating 2 mol% DGS-NTA the change in molecular net charge by 1 e^- between the Ni-loaded and unloaded state yielded a sensitivity of ΔQ = 0.5 µCcm^{-2}. With 0.5 mol% NTA, a change in charge density from Ni-loading and unloading of ΔQ = 0.1 µC/cm^{-2}

could still be clearly resolved, which equates to a change of one elementary charge per 130 nm^2. Here, even the surface potential change in eGFP-loaded state could be distinguished, using GaN HEMT structures, which could not be shown in previous experiments on bulk GaN (Frenkel 2014). With ΔV_{th} from eGFP docking being approximately half of the value observed from complete unloading of the monolayer, a possible resolution close to ΔQ = 0.05 μC/cm^{-2} is suggested. This demonstrates the great sensitivity achieved by this GaN/AlGaN/GaN heterostructures, which expressed a considerably improved sensitivity compared to other semiconductor materials, such as ITO; ΔQ = 2.2 μC/cm^{-2} (Hillebrandt et al. 2002) and GaAs; ΔQ = 0.9 μC/cm^{-2} (Gassull et al. 2008).

One has to note that DGS-NTA is only completely deprotonated if pH ≥ pKa(NTA) = 9.73. At pH = 7.5 during these measurements only a minor fraction of NTA lipids will carry a net charge of – 2. Thus, the actual change in net charge upon complexation with Ni^{2+} is smaller than 1 e^-. This suggests that a much smaller change in the surface charge density occurs at this stage ans a significantly higher sensitivity towards the surface charge density is expected.With the degree of protolysis α for weak acids,

$$\alpha = \sqrt{\frac{Ka}{C}} \text{ and } pH = \frac{pKa - lg\,(c)}{2} \qquad (5.1) \text{ and } (5.2)$$

Where K_a is the acid dissociation constant and c the acid (NTA) concentration, the amount of completely dissociated DGS-NTA can be calculated to α = 0.6%.

5.3 Towards Detection of Integral- and Transmembrane Protein Function in Polymer Supported Membranes on GaN/AlGaN/GaN HEMTs

5.3.1 Surface Topography of the Cellulose Support

In order to create sensor platform for the investigation of membrane functions mediated by integral and trans-membrane proteins, such as material and energy transport, signaling and cell adhesion (Saier et al. 2009), a nature-like membrane model is needed. Here, hydrated cellulose polymer films were used on GaN heterostructures to mimic the extracellular matrix, creating hydration pathways between semiconductor and membrane and acting as cushion to avoid direct protein-semiconductor contact and denaturation. The versatility of regenerated cellulose films with flexibly adjustable thickness and wetting properties (Schaub et al. 1993) allows for the fabrication of polymer cushions with defined structural and mechanical properties. In previous studies it has been shown that human erythrocyte membranes and sarcoplasmic reticulum membranes (Tanaka et al. 2001) can be deposited on such cellulose polymers, using polymers with a dry thickness of approximately 5 nm

First, the successful deposition by spin coating of the trimethylsilyl-substituted cellulose (TMSC) and subsequent regeneration in HCl vapor was confirmed by contact angle measurements. Spin coating of the 2.7 g/l TMSC solution resulted in a strongly hydrophobic surface, as shown by the high contact angle $\theta \sim 90°$ observed in Figure 5.8a. The trimethylsilyl- moieties create a so called ‘hairy-rod’ polymer, rending the former hydrophilic cellulose backbone hydrophobic. After cleavage of these moieties with HCl vapor the water contact angle on the dried surface sharply decreases to 18° (Figure 5.7b), confirming the successful regeneration of the cellulose polymer.

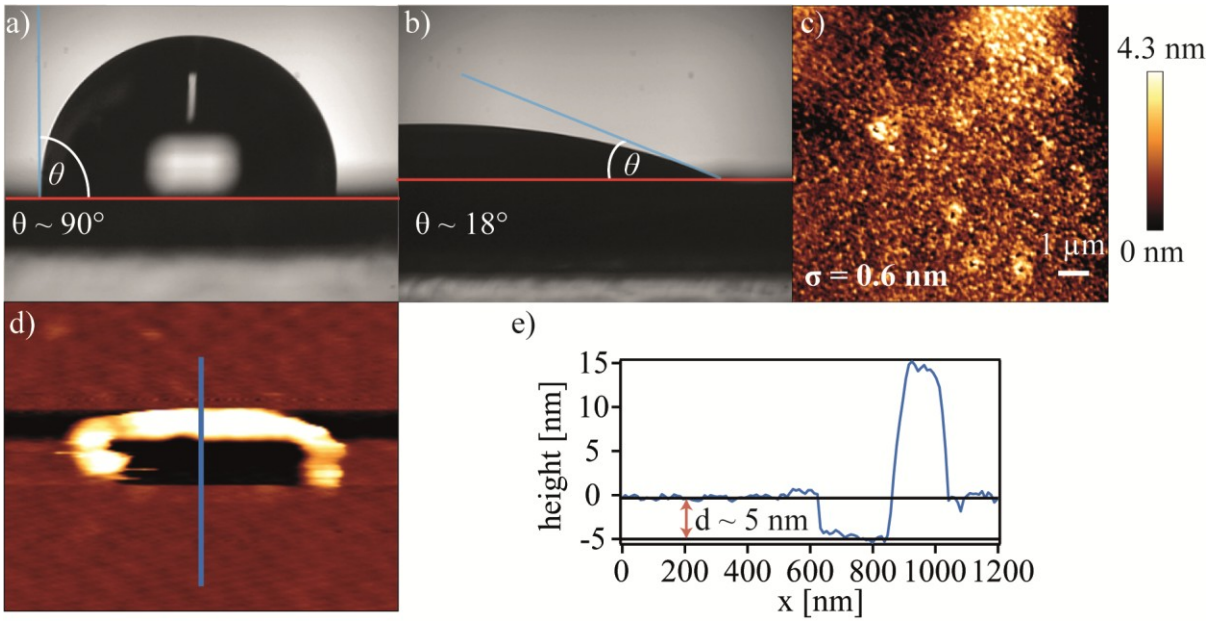

Figure 5.8: *Contact angle of (a) TMSC coated Si; θ ~ 90° and (b) contact angle after regeneration of cellulose; θ ~ 18°. (c) AFM image of dry cellulose on Si after regeneration, image size is 10 x 10 µm. (d) AFM image of the scratched surface, image size is 1.5 x 1.5 µm and (e) the corresponding height profile of the scratch indicated with the solid blue line. The height difference between the film surface and the scratch track (5 nm) suggests the formation of a peptide monolayer.*

The surface topography of the regenerated and dried film is shown in Figure 5.8c. The 10 µm x 10 µm areas, recorded by contact mode AFM show that a homogeneous coverage of cellulose with a low defect density was achieved. This was reflected by the low mean square roughness of $\sigma = 0.5 – 0.7$ nm obtained, which agrees well with values from previous reports (Rosetti et al. 2008) and supports the further formation of a homogeneous lipid membrane. In Figure 5.8d the scratch track produced by high force contact mode AFM in a small 0.5 µm x 0.5 µm area is shown. From the height difference between the cellulose film and the scratched area a thickness of the dry cellulose layer of $d = 5 – 6$ nm was determined, which was further confirmed by ellipsometry measurements.

5.3.2 Lipid Membrane Formation

To mimic and transduce membrane and membrane-protein functionalities, such as the creation of certain ionic concentration gradients and membrane potentials between cytosol and ECM by ion channels, into an electrical signal a high electrical resistance and thus low defect rate in the membrane is needed. The homogeneity of the membranes formed on the regenerated cellulose cushions was assessed by fluorescence microscopy for different lipid compositions and vesicle fusion and solvent exchange preparation

methods. Compositions of 55 mol%, 50 mol% and 40 mol% DMPC or DOPC as matrix lipid, 5 mol%, 10 mol% and 20 mol% positively charged DMTAP and 39.8 mol% cholesterol, including 0.2 mol% texas-red-DHPE were used. Membranes using DMPC as matrix lipid and 20 mol% DMTAP showed the most homogeneous distribution in the fluorescence intensity (Figure 5.9). The use of lower DMTAP concentrations led to the appearance of more inhomogeneities and even phase separation in some cases. Stronger interaction forces between the positively charged DMTAP and cellulose hydroxyl-moieties with increasing DMTAP ratio in the membrane cause an improved wettability of the cellulose polymer for the membrane. Membranes with 20 mol% DMTAP prepared by vesicle fusion further showed, at first, a similar intensity distribution as solvent exchange prepared membranes. For the latter membrane however an increase in inhomogeneities was observed over time, suggesting a better membrane stability gained from the vesicle fusion protocol. This is further expressed by the larger inhomogeneity observed at lower DMTAP ratios in the membranes prepared from solvent exchange (Figure 5.9, bottom).

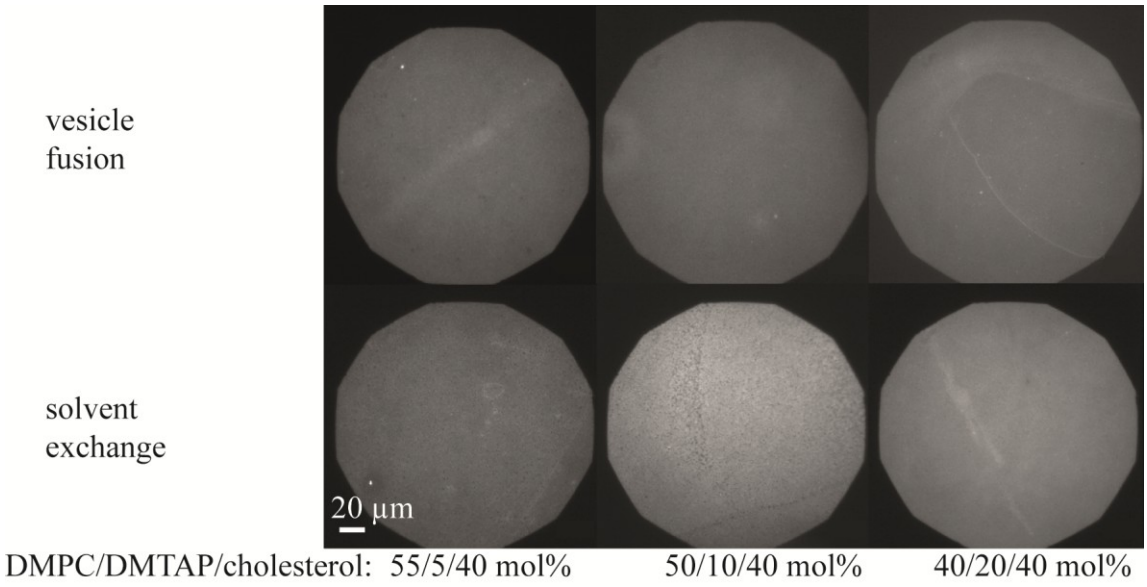

Figure 5.9: *Fluorescence images of 0.2 mol% texas-red-DHPE containing lipid membranes on regenerated cellulose with different ratios of positively charged DMTAP, deposited by vesicle fusion (top) and solvent exchange (bottom).*

Even though the DOPC membrane should possess a higher mobility, due to the two double bonds in the DOPC fatty acids reducing the hydrophobic interaction between the lipid tails, more inhomogeneities and phase separation at lower DMTAP concentrations were observed as well as a reduced stability of the membrane over time.

The mobility of the DOPC and DMPC membranes, as a measure for the capability of membranes to heal defects, was quantified by FRAP. Here, DOPC and DMPC membranes containing 20 mol% DMTAP were deposited by vesicle fusion, since these

membranes showed the most homogeneous coverage. Lateral diffusion coefficients *D* were determined from the intensity recovery after the fluorescence dye was bleached in a radius of 5 µm by a short pulse (200 µs) of high intensity laser light.

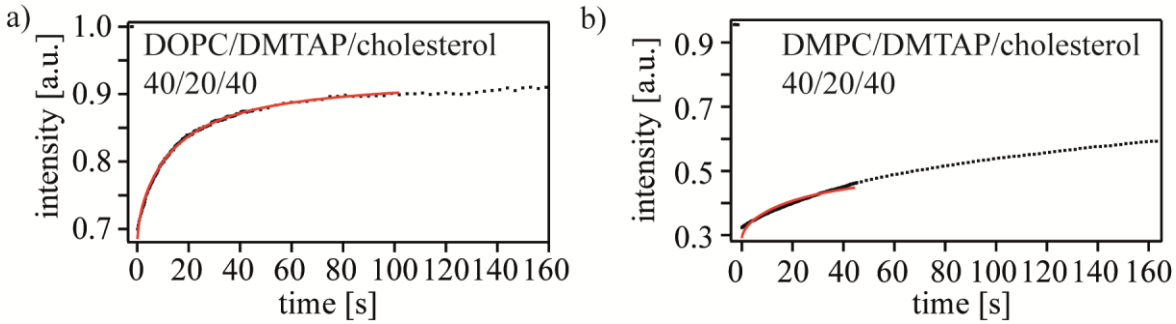

Figure 5.10: *Normalized FRAP intensity recovery of the regenerated cellulose layer after deposition of (a) 40/20/40 mol% DOPC/DMTAP/cholesterol membrane and (b) 40/20/40 mol% DMPC/DMTAP/cholesterol membrane with 0.2mol% Texas-Red.*

From the intensity recoveries shown in Figure 5.19, lateral diffusion coefficients of D_{DOPC} = 0.8 ± 0.2 µm^2/s and D_{DMPC} = 0.3 ± 0.1 µm^2/s with a mobile fraction 80 % and 40% were found for the DOPC and DMPC membrane respectively. Compared to similar experiments on a 10 nm cellulose cushion using a lipid bilayer containing 65/30/5 mol% DOPC/cholesterol/DMTAP (D = 1.4 µm^2/s) (Hillebrandt 2002) a slightly lower diffusion coefficients was observed for DOPC membrane. This is explained by the higher proportion of cholesterol used here, causing the membrane to form a liquid ordered phase with higher rigidity and thus a reduced lateral diffusion (Sigl et al. 1997). A further decrease in *D* and even fraction of mobile lipids was observed for the DMPC membrane. Since, in contrast to DOPC, the fatty acids in DMPC do not possess double bonds, stronger interaction forces between the lipid molecules are allowed, causing a tighter packaging of the lipid phase and further reducing the membrane mobility and fluidity. Although the self-healing capability is reduced, 40/20/40 mol% DMPC/DMTAP/cholesterol membranes deposited by vesicle fusion were used for further experiments, due to the improved homogeneity and stability compared to other lipid compositions.

The formation of membrane (40/20/40 mol%) was further investigated by XRR on regenerated cellulose coated native oxide Si substrates. First, the thickness, *SLD* and roughness of the hydrated cellulose layer were determined from the reflectivity graphs in Figure 5.11 prior to the membrane formation (blue), using a 2 slab model. This model included representations for the SiO_2 layer and the regenerated cellulose polymer that was hydrated in HEPES buffer. After membrane formation by vesicle fusion for 3 h the reflectivity graph was analyzed with 3 additional slabs for the lipid membrane (red),

describing the layer of the lower lipid head groups at the cellulose interface, lipid tails, and upper head groups at the lipid/water interface.

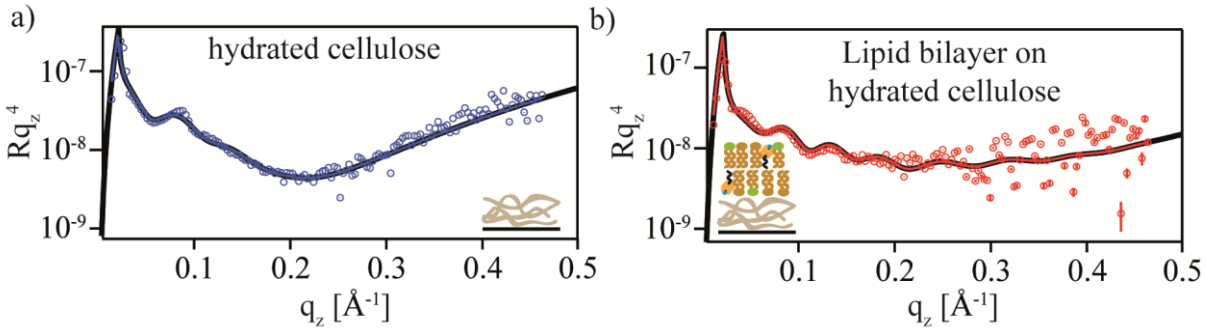

Figure 5.11: *Reflectivity graphs normalized by q_z^4 of the regenerated cellulose polymer on Si measured in HEPES buffer. The solid lines represent the fitting result ($\chi^2 < 0.02$) of the experimental data (a) before (green circles) and (b) after membrane deposition* (40/20/40 mol%) *(red circles). A respective scheme of the stratified model system is shown in the inset.*

The obtained best fit parameters (Table 5.4) for the regenerated cellulose layer prior to membrane deposition showed that the cellulose thickness increased approximately 2 times upon hydration compared to the dry state thickness, measured by ellipsometry and AFM. This swelling of the cellulose polymer under buffer conditions agrees well with previous accounts, where an increase by the factor of 1.5 – 2 in cellulose thickness was observed (Hillebrandt et al. 2002). This is further accompanied by an increase in roughness from σ = 6 Å determined by AFM to σ = 12.5 Å. The obtained *SLD* of the cellulose layer of $7.3 \cdot 10^{-6}$ Å^{-2} also agrees well with a similar spin coated film fabricated by Rosetti et al. (Rosetti et al. 2008).

By comparing the two reflectivity curves before (Figure 5.11a) and after membrane deposition (Figure 5.11b) one can clearly observe an increase in intensity at $q_z \sim 0.2$ Å^{-1}, suggesting the successful formation of the membrane. One has to note that the membrane formation was performed on a different sample.

Table 5.4: *Best fit parameters ($\chi^2 < 0.02$) of the regenerated cellulose polymer on Si, hydrated in HEPES buffer.*

layer	prior to membrane deposition			after membrane deposition		
	d [Å]	SLD [10^{-6} Å^{-2}]	σ [Å]	d [Å]	SLD [10^{-6} Å^{-2}]	σ [Å]
lipid head group	-	-	-	9.4	9.7	8.7
lipid alkyl chains	-	-	-	28.3	8.4	9.8
lipid head group	-	-	-	11.8	9.6	8.6
regenerated cellulose	110	7.3	12.5	129	9.3	4.8
SiO_2	16.0	18.6	6.7	16.7	18.6	4.1

Here, a similar swelling of the hydrated cellulose layer to d = 129 Å was observed, while the cellulose interface roughness decreased compared to the state prior to membrane formation. Compared to solid supported membranes (Frenkel 2015) higher roughness values across the whole lipid membrane were observed, due to the intrinsic higher roughness of the cellulose support. This suggests the 'healing' of defects in the cellulose layer by formation of the lipid membrane, as undulations and other defects in the cellulose polymer are filled by the membrane. The obtained *SLD* though were smaller for the lipid head groups and higher for the lipid alkyl chains. This could possibly be caused due to the increased fraction of cholesterol in the membrane which is incorporated in lipid tail region near the head/tail interface, thus increasing the alkyl SLD and lowering the head group density. These results clearly indicate that a successful membrane formation over large area was achieved with little defects.

5.3.3 Impact of Lipid Membranes on HEMT I-V-Characteristics

The potential sensory capability of this membrane model was evaluated by depositing the regenerated cellulose and membrane (40/20/40 mol% DMPC/DMTAP/cholesterol) on GaN/AlGaN/GaN HEMT gate regions. Changes in the electrical *I-V* characteristics were analyzed before and after the cellulose and membrane deposition by recording the HEMT transfer characteristics as the gate voltage (V_G) dependent drain-source current (I_{DS}) at a constant source-drain voltage V_{DS} = 0.3 V, as well as output characteristics as the V_{DS} dependent drain-source current (I_{DS}) at a constant V_G = – 1.5 V. First, the influence of the regenerated cellulose deposition was investigated. Transfer ($I_{DS} - V_G$) and output ($I_{DS} - V_{DS}$) curves of the GaN HEMT were recorded before (black) and after the deposition and hydration for 15 min of regenerated cellulose (blue) in standard HEPES buffer (Figure 5.12). The threshold voltage V_{th} and transconductance g values collected from the slope and linear regression at V_G = – 1.75 ± 0.5 V of the transfer curves in Figure 5.12a show only a minor deviation from the untreated state (black) of $V_{th,\ untreated}$ = – 2.27 V and

$g_{untreated}$ = 35.3 µS to $V_{th,\ cellulose}$ = – 2.25 V and $g_{cellulose}$ = 34.3 µS after cellulose deposition (blue).

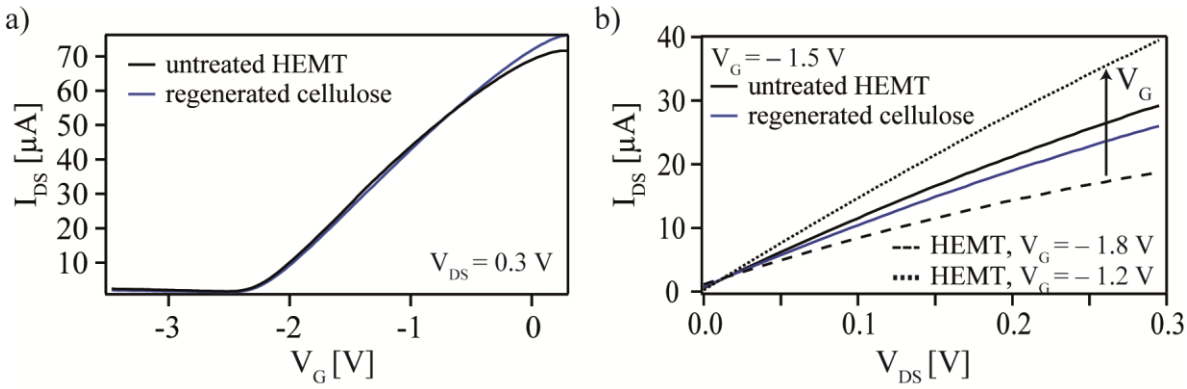

Figure 5.12: *Influence of regenerated cellulose deposition on I-V characteristics of the GaN HEMT. Comparison between the untreated GaN HEMT (black) and the cellulose coated HEMT (blue) shows only minor changes in (a) transfer (I_{SD}-V_G) curves measured at V_{SD} = 0.3 V and (b) output (I_{DS}-V_{DS}) curves measured at V_G = – 1.5 V.*

Surprisingly, slightly stronger changes in the output characteristics (Figure 5.12b) were observed. Here, from the drop in I_{DS} after cellulose deposition, the apparent change in V_G can be equated to $\Delta V_{G,\ cellulose}$ = 64 mV. Since the regenerated cellulose film becomes hydrated and swells in aqueous buffer (Hillebrandt et al. 2002, Rosetti et al. 2008), it acts electronically like an electrolyte layer. Most changes in surface dielectric structure incurred by cellulose deposition are thus screened by incorporation of water. The minor changes observed in *I-V* characteristics suggest that the regenerated cellulose film is almost completely hydrated.

In the next step lipid membranes (40/20/40 mol% DMPC/DMTAP/cholesterol) were further deposited by vesicle fusion on the HEMT gate region. To demonstrate the potential of this system towards the sensing of biological processes occurring at the membrane, the membranes were subjected to a flow (0.25 ml/min) of 5 µM phospholipase A_2 (Pla2) in Ca-buffer for 2 h. Transfer and output curves of the HEMT after deposition of cellulose (blue), lipid membrane (red) and Pla2 incubation (green) are presented in Figure 5.13.

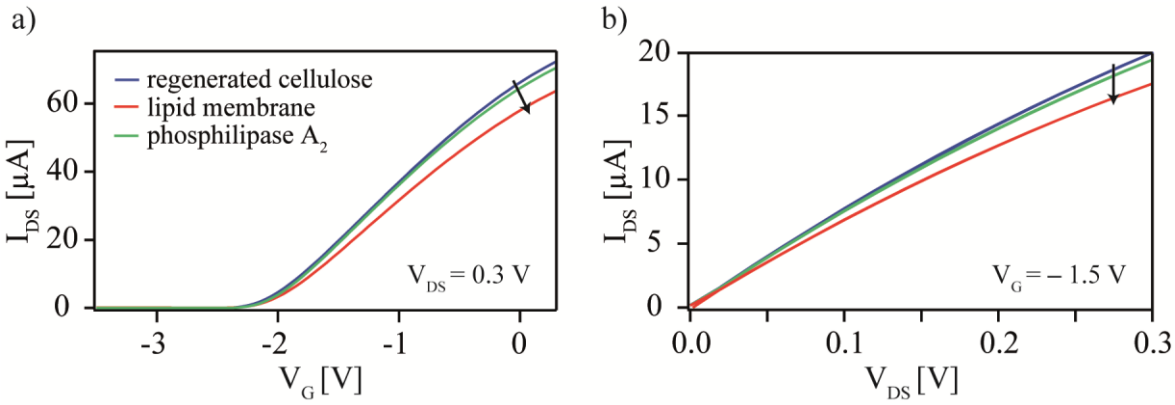

Figure 5.13: *(a) Transfer (I_{DS}-V_G) curves measured at V_{DS} = 0.3 V of the HEMT after cellulose (blue) and lipid membrane (40/20/40 mol% DMPC/DMTAP/cholesterol) (red) deposition and subsequent rinsing with 5 µM phospholipase A_2 (Pla2) in Ca-buffer for 2 h (green). Threshold voltage V_{th} and transconductance g values were obtained from linear regression at V_G = – 1.50 ± 0.25 V. (b) Output (I_{DS}-V_{DS}) curves measured at V_G = – 1.5 V of the cellulose (blue), membrane (red) and Pla2 (green) washed HEMT.*

As seen in the transfer curves in Figure 5.13a, membrane deposition resulted in a significant decrease in transconductance g from 33.9 µS after cellulose deposition to 30.1 µS (Table 5.5); Δg = – 3.8 µS, while V_{th} exhibited almost no changes. Since $g = \frac{\Delta I}{\Delta U} = 1/R$, the decrease in g due to membrane formation can be understood as a rise in resistance towards the gate potential, suggesting the successful formation of an electrical insulating membrane with a resistance of 0.26 MΩ. From the decrease in I_{DS} after membrane formation in Figure 5.13b, the apparent change in V_G that is "felt" by the GaN HEMT was estimated to $\Delta V_{G,\ membrane}$ = 75 mV. These changes were almost completely reversed after Pla2 incubation. Pla2 cleaves one alkyl tail of the lipid fatty acid, leading to a destabilization and loss of insulating property of the membrane. This clear change in *I-V* characteristics observed from the interaction of the enzyme with the membrane demonstrates the potential of this membrane sensor model for further experiments, where the incorporation of trans membrane proteins, such as ion channels, could lead to a selective change in the resistance generated by the lipid membrane for certain ion species.

Table 5.5: *Summary of threshold voltage V_{th} and transconductance g values the HEMT after deposition of regenerated cellulose, membrane (40/20/40 mol% DMPC/DMTAP/cholesterol) and after rinsing with 5 µM phospholipase A_2 (Pla2) in Ca-buffer. The values were determined from linear regression of the transfer curves between $V_G = -1.50 \pm 0.25$ V.*

state	V_{th} [V]	g [µS]
regenerated cellulose	– 2.08	33.9
lipid membrane	– 2.04	30.1
Pla2	– 2.06	33.8

The V_{th} levels observed after membrane deposition however were not consistent between multiple measurements. As shown in Figure 5.14a and summarized in Table 5.6, a drastic change in V_{th} of $\Delta V_{th} = -0.26$ V was also observed upon membrane formation, while the change in transconductance of $\Delta g = -3.3$ µS was consistent with the previous measurement. The consistent $\Delta g = -3$ to -4 µS observed further confirms the reproducibility of the decrease in g caused by the membrane. Similar to the previous measurement, the effect of the membrane on the *I-V* characteristics could be fully reversed by washing with isopropanol. This completely removed the deposited membrane and thus further suggests that the observed ΔV_{th} and Δg were caused by the formation of the lipid membrane.

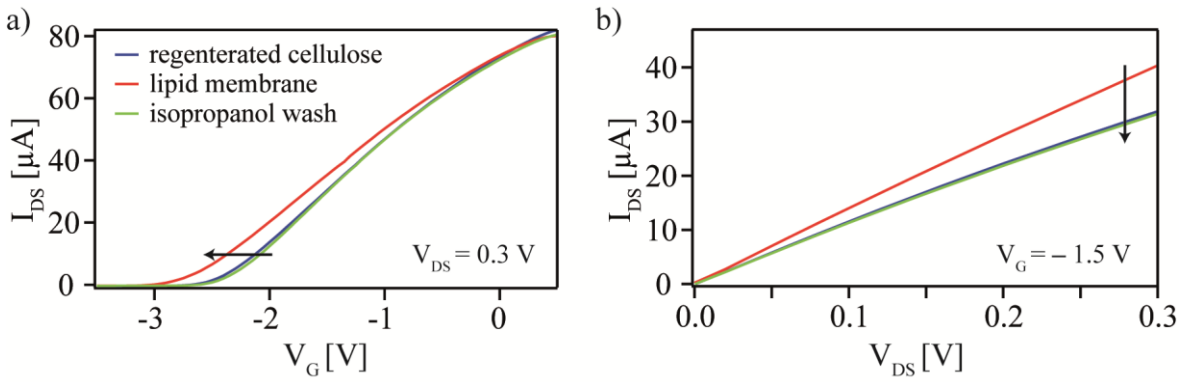

Figure 5.14: *(a) Transfer (I_{DS}-V_G) curves measured at V_{DS} = 0.3 V of the HEMT after cellulose (blue) and lipid membrane (40/20/40 mol% DMPC/DMTAP/cholesterol) (red) deposition and subsequent rinsing with isopropanol for 10 min (light green).*

Table 5.6: *Summary of threshold voltage V_{th} and transconductance g values the HEMT after deposition of regenerated cellulose, membrane (40/20/40 mol% DMPC/DMTAP/cholesterol) and after rinsing with isopropanol. The values were determined from linear regression of the transfer curves between V_G = – 1.50 ± 0.25 V.*

state	V_{th} [V]	g [µS]
regenerated cellulose	– 2.41	33.5
lipid membrane	– 2.67	30.2
isopropanol	– 2.35	34.8

The large ΔV_{th} suggests a change in surface potential of the HEMT occurred after membrane deposition. Influences from the membrane charges itself should not be sensed by the GaN HEMT due to the hydrated cellulose cushion between membrane and transistor. The Debye length λ_{D} can be given as a measure for the sensitivity of the HEMT to potential changes occurring not directly on its surface (Lu et al. 2014). It describes the characteristic distance at which the potential exerted by a local charge decays to 1/*e* and is given by:

$$\lambda_D = \sqrt{\frac{\varepsilon_0 \varepsilon_r k_B T}{2 N_A e^2 I}} \quad with \; I = \sum_{i=1}^{n} b_i z_i^2 \tag{5.3}$$

where T, k_{B}, N_{A} and e have their usual meaning, ε_0 is the permittivity of vacuum, ε_{r} the dielectric constant of the medium, here water (ε = 80) and I the ionic strength of the buffer, determined from its molar concentration b_{i} and charge number z_{i} of its i ion species.

Taking the standard HEPES buffer used in these measurements λ_{D} = 2.9 nm is obtained. The cellulose polymer used here is thicker (d_{dry} = 5nm) than λ_{D}, especially in its hydrated, swollen state, where its thickness is approximately 1.5 times higher than in its dry state (Hillebrandt et al. 2002, Rosetti et al. 2008). Hydrated cellulose that is saturated with water effectively screens the charges and dipoles in the membrane similarly to the bulk buffer, thus no effect on the surface potential should be observed from membrane deposition. The different ΔV_{th} observed however might by an uncontrollable change in surface potential between semiconductor, the electrolyte like cellulose polymer and membrane insulator.

5.4 Summary

Reversible modulation of surface charges was achieved by deposition of a supported lipid monolayer on ODTMS coated GaN heterostructures containing a defined amount of lipid anchors with NTA head groups (DGS-NTA (Ni)), allowing for the coupling of the histidine-tagged recombinant protein eGFP. After confirmation of the formation of a homogeneous ODTMS support with AFM and subsequent lipid monolayer formation and protein binding with XRR and fluorescence microscopy, clearly distinguishable changes in the GaN HEMT *I-V* characteristics and V_{th} were observed from protein complexation on the Ni-NTA groups and breaking of the complex with EDTA. The reversible change in V_{th} from loading and unloading of the monolayer with Ni^{2+} as well as protein binding demonstrated that a sensitivity towards the change of surface charge density and thus surface potential of $\Delta Q < 0.5$ μCcm^{-2} was achieved using 2 mol% NTA lipids in the monolayer. The use of 0.5 mol% DGS-NTA further demonstrated that a much higher sensitivity than most other semiconductor materials close to $\Delta Q \geq 0.05$ μCcm^{-2} can be reached with these GaN heterostructures.

In the next step the modulation of resistance towards V_G was demonstrated by lipid membrane deposition on GaN heterostructures coated with regenerated cellulose polymer support. After determination of well defined thickness and roughness of the regenerated cellulose layer by AFM, the deposition of lipid bilayers by vesicle fusion on this thin polymer support displayed the best homogeneity and stability with high molar ratio of positively charged lipid from fluorescence microscopy measurements. Consistent Δg of -3 to -4 µS in the *I-V* characteristics were achieved after membrane deposition resulting in an increase of the HEMT resistance towards the applied V_G. Further digestion of the membrane by Pla2 enzyme could be observed as well in the *I-V* characteristics. The observed changes in V_{th} however were inconsistent. The distinguished Δg upon membrane deposition demonstrates the potential of this membrane model on the GaN heterostructure for the incorporation of membrane proteins, such as ion channels, and the detection of their functionalities by the change in membrane resistance towards the applied V_G.

6. Towards Membrane Monolayer Models on OFET Biosensors

6.1 Introcuction

Biosensors based on organic field effect transistors (OFETs) are one of the more promising device applications in organic electronics. Due to their unique properties of sustainability, flexibility, lightweight and low energy consumption, as well as low production costs, OFETs have been extensively studied as one of the most promising building blocks for printable electronic devices such as displays (Yagi et al. 2008), sensors (Knopfmacher et al. 2014), and radio-frequency identification tags (Cantatore et al. 2014). However, biosensors based on OFETs are still not investigated extensively compared to other electrochemical biosensors. Research in OFETs and their advantages have been recently extended beyond electrical engineers and information displays to biomedical engineers and sensor applications (Lin and Yan 2012, Minami et al. 2014, Torsi et al. 2013, Hirschhaeuser et al. 2011), opening a way for the creation of novel biosensor device platforms. The key properties for OFETs to fabricate such devices are a high carrier mobility, low subthreshold swing and threshold voltage (V_{th}), together with an excellent compatibility of the organic semiconductor to solution- and low-temperature processes. Charge transport in field-effect transistors occurs at the interface between semiconductor and gate insulator. Thus, the minimization of structural and energetic disorders at the interface leads to an improved device performance. This can be achieved by the use of self-assembled monolayers (SAMs) as well as blends of insulating polymer and organic semiconductor (Smith et al. 2012, Lui et al. 2013, Hunter et al. 2014, Shiwaku et al. 2016) as an interfacial modification layer, resulting in lower subthreshold swing and controllable V_{th}. The carrier mobility of these often polycrystalline organic semiconductor materials however is limited by grain boundaries and defects (Verlaak et al. 2003). To overcome this limitation, a single crystal semiconductor thin film was developed by the group of Okamoto and Takeya et al. (Mitsui, Okamoto et al. 2014, Makita et al. 2017), using a combination of polymer blend methods and the continuous edge-casting method with a mixture of N-shaped π-conjugated octyl or nonyl substituted dinaphtho[2,3-*d*:2′,3′-*d*′]benzo[1,2-*b*:4,5-*b*’]dithiophene (DNBDT) and poly(methyl-methacrylate) as insulating polymer (Figure 6.1) (Soeda, Okamoto et al. 2016). The interaction of N-shaped π-stacks an hydrophobic alkyl chains produces an ultra-thin film composed of a single-crystalline organic semiconductor on the top of an amorphous insulating polymer layer, achieving a high hole mobility of $\mu = 16\,cm^2\,V^{-1}s^{-1}$, low threshold voltage of about − 5 V and low trap-density (Mitsui, Okamoto et al. 2014).

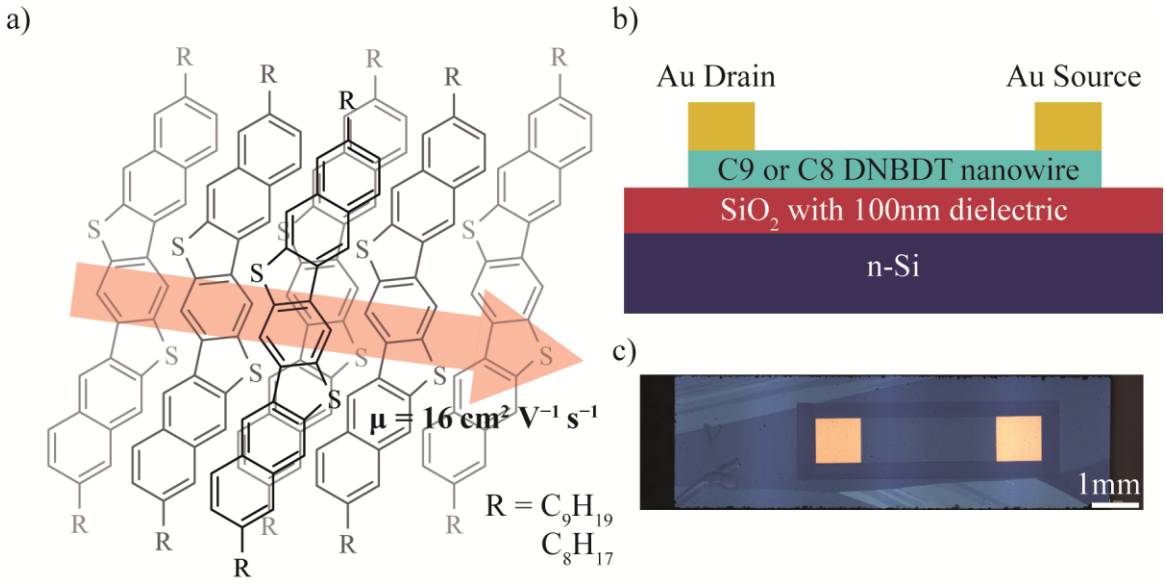

Figure 6.1: *(a) π-stacks formation in the N-shaped DNBDT single crystal film. (b) Schematic OFET structure. The C9-DNBDT film is edge casted on n-type Si with a 100 nm insulating polymer dielectric. (c) Top view of the DNBDT OFET.*

The well ordered crystalline structure of the alkyl chains in the DNBDT film creates a hydrophobic interface and the possibility to facilitate monolayer membrane models. This chapter details the exploration of biosensoric applications of this OFET system as support of membrane monolayer systems containing phospholipids and DGS-NTA chelator lipids for the reversible anchoring of proteins.

6.2 Structural Characterization of the Organic Semiconductor Material

Prior to membrane deposition topographic images were taken of the C8- and C9-DNBDT semiconductor surface in an area of 25 µm x 25 µm by contact mode AFM. The bulk C8- and C9-DNBDT samples were provided by Prof. Dr. T. Okamoto and Prof. Dr. J. Takeya (Univ. Tokyo) on glass and silicon substrates respectively. Figures 6.2a – c show that large, lamella-like crystalline layers of the organic semiconductor DNBDT could be created by the drop-casting procedure. The rms roughness collected from an 25 µm x 25 µm area is 2.6 Å for the C8-DNBDT semiconductor. This value is dependent from the scan area, and the uniformity of the layer. As shown in Figure 6.2b larger scale defects could be observed with an increased surface roughness of 7.1 nm. Several smaller structures in the semiconductor layer were observed with discrete step heights of approximately 3 nm (Figure 6.2d1), which possibly corresponds to the length of a C8-DNBDT molecule in a near upright orientation. Other discrete step heights of up to 8 nm were observed, suggesting the crystallization of C8-DNBDT molecules in multilayers.

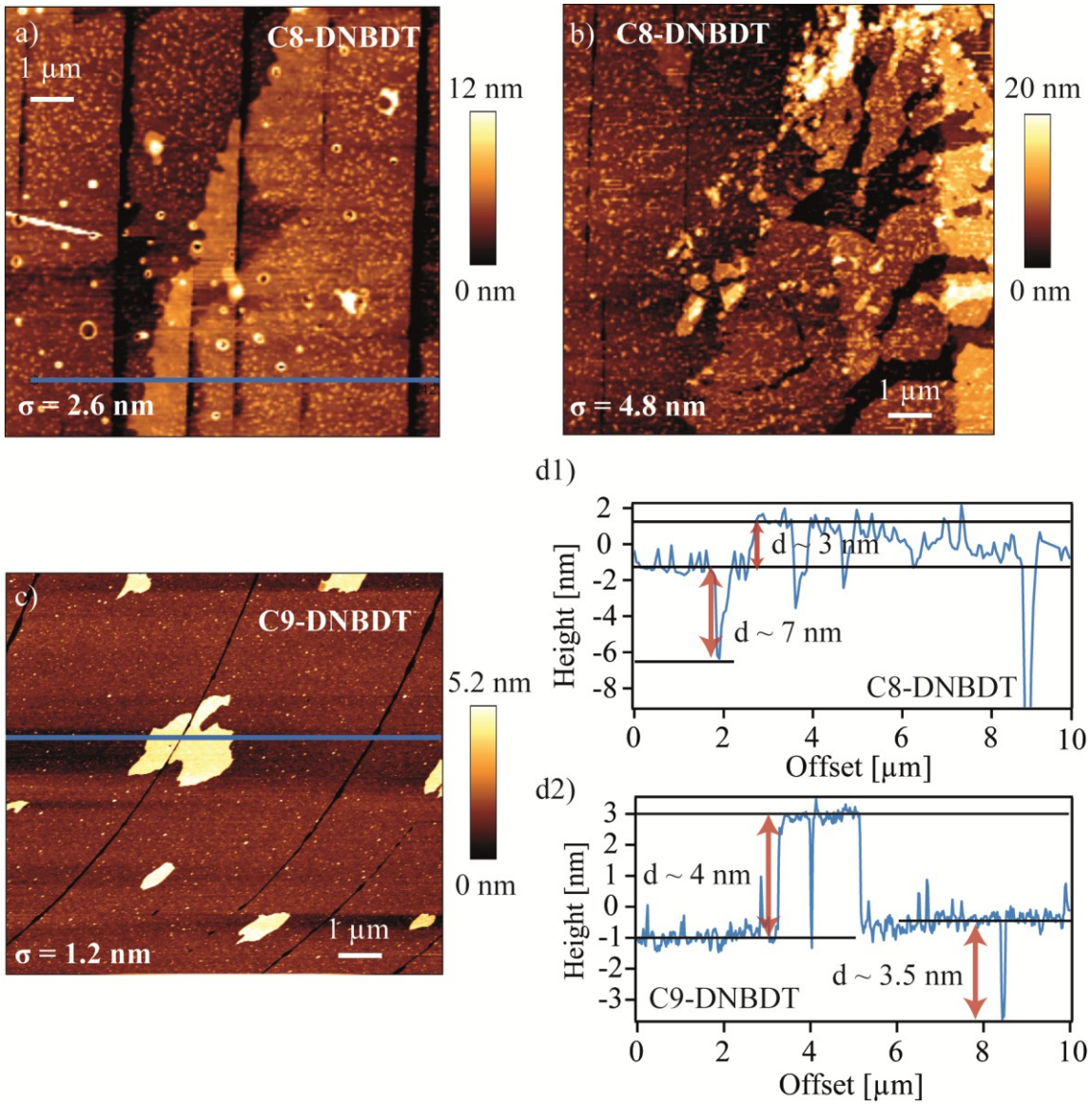

Figure 6.2: *(a) and (b) AFM images of the as received C8-DNBDT semiconductor with a scan area of 10 µm x 10 µm. Height map is given with a relative color scale. (c) Height tack of (d1) C8-DNBDT and (d2) C9-DNBDT indicated by the blue line in Figure 1a and c respectively.*

The C9-DNBDT material on the other hand showed a more homogeneous coverage with an rms roughness of 1.2 nm (Figure 6.2c), suggesting the formation of considerable fewer defects compared to C8-DNBDT. Discrete step heights in the height track (Figure 6.2d2) of 3.5 – 4 nm were observed, which correspond well to the values obtained for the similar C10-DNBDT previously reported (Mitsui, Okamoto et al. 2014). Some 4 nm high artifacts and islets were observed as well, suggesting a small degree of multilayer formation also occurring for the C9 semiconductor. To determine the thickness of the film more precisely on a larger scale, XRR measurements were performed.

First the reflectivity graph of the as received C8-DNBDT on glass substrate was investigated in aqueous buffer (HEPES), using a one slab model for the semiconductor layer (Figure 6.3a). The obtained best fitting parameters of the layer thickness *d*, scattering length density *SLD* and interface roughness σ are summarized in Table 6.1.

Table 6.1: *Best fit parameters (χ^2 = 0.02) of the as received C8-DNBDT organic semiconductor in aqueous buffer.*

layer	thickness [Å]	SLD [10^{-6} Å^{-2}]	roughness [Å]
C8-DNBDT	20.2	11.9	6.2

The obtained C8-DNBDT thickness d_{C8} = 20 Å is comparable to the AFM result for the discrete step height for one C8-DNBDT layer. Compared to the thickness of the previously reported similar C10-DNBDT (d_{C10} = 41 Å) (Mitsui, Okamoto et al. 2014) however, a slightly lower thickness than expected was obtained. Sharp edges and inhomogeneities seen in AFM images and the high roughness possibly led to an underestimation of thickness by XRR. The RMS roughness of 6.2 Å collected over a large beam footprint of ~ 2 mm^2 although, suggests the formation of a "molecularly" smooth film, while the *SLD* of C8-DNBDT (11.9 · 10^{-6} Å^{-2}) is reasonable compared to the value expected from a similar, chrysene-like crystal with a calculated *SLD* of 11.4 · 10^{-6} Å^{-2}.

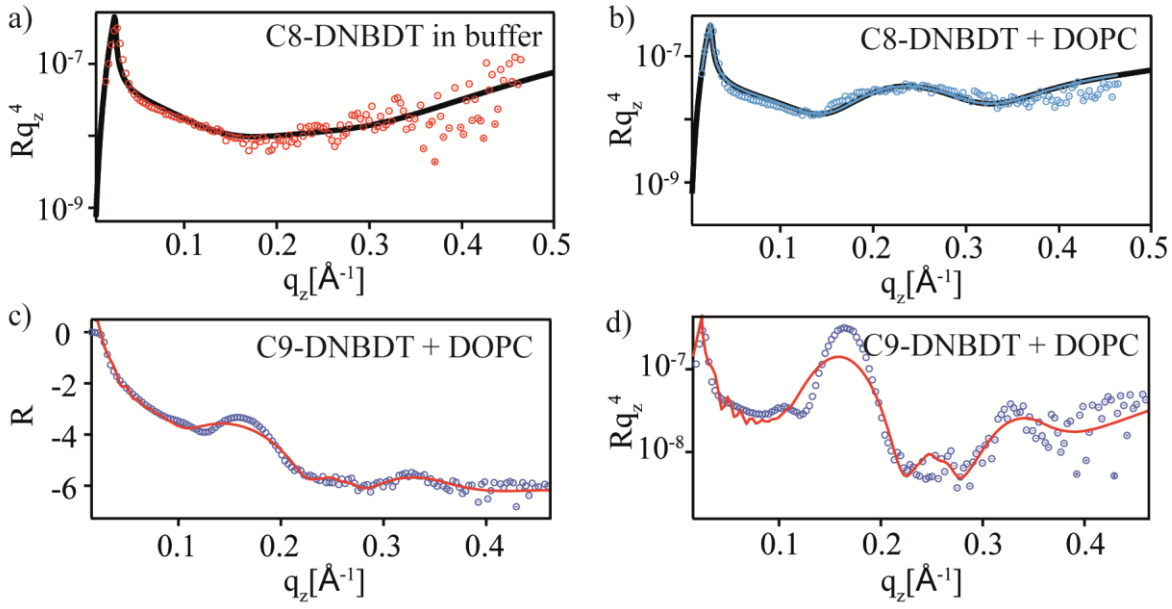

Figure 6.3: *Fresnel plots normalized by q_z^4 of (a) as received C8-DNBDT organic semiconductor and (b) C8-DNBDT after deposition of a DOPC monolayer in HEPES buffer. (c) Logarithmic reflectivity curve and (d) Fresnel plot normalized by q_z^4 of C9-DNBDT after deposition of a DOPC monolayer in HEPES buffer.*

Figure 6.2b shows the C8-DNBDT semiconductor after DOPC monolayer deposition. A three slab model was employed including slabs for the C8-DNBDT layer, lipid alkyl chains and head groups, with the best fit parameters are summarized in Table 6.2. The appearance of the broad peak at q_z = 0.25 $Å^{-1}$ suggests the successful formation of the monolayer.

Table 6.2: *Best fit parameters (χ^2 = 0.02) of C8-DNBDT after vesicle fusion in aqueous buffer.*

layer	thickness [Å]	SLD [10^{-6} $Å^{-2}$]	roughness [Å]
lipid head group	9.4	10.5	6.9
lipid alkyl chains	15.2	7.4	7.9
C8-DNBDT	27.3	11.3	3.3

The total thickness of the lipid monolayer d_{DOPC} = 24.6 Å is reasonable, while the values SLD of the head groups and hydrocarbon chains agree well with the previous studies (Frenkel 2015). The best fit results implied a slight increase in the thickness of C8-DNBDT (Δd = 7 Å) and a decrease in the semiconductor interface roughness, which suggests that the local defects (Fig. 6.2) were healed by hydrocarbon chains of lipid molecules.

XRR measurements for C9-DNBDT were performed on silicon substrate. This and higher the higher thickness of the organic semiconductor layer observed by AFM enables an improved structural characterization of the C9-DNBDT layer. Thus, C9-DNBDT was analyzed by a four slab model including additional representations for the C9 chains at the Si interface, separate DNBDT π-core system, the combined C9 and lipid alkyl chains and the lipid head groups (Table 6.3).

Table 6.3: *Best fit parameters (χ^2 = 0.05) of C9-DNBDT after vesicle fusion in aqueous buffer.*

layer	thickness [Å]	SLD [10^{-6} $Å^{-2}$]	roughness [Å]
lipid head group	10.7	13.3	4.3
lipid alkyl chains + C9 Chains	24.9	7.6	9.5
DNBDT	25.3	12.6	3.3
C9 Chains	11.6	7.6	6.7

The appearance of the sharp peak at q_z = 0.15 $Å^{-1}$ (Figure 6.3c-d) could not be completely accounted for by the fit. Additional refraction and reflection events at the multilayer islets, observed by AFM, possibly cause a sharper peak and the divergence in the fit.

Nonetheless, reasonable thickness values for C9-DNBDT were obtained, which are comparable to the results from AFM measurements. For the lipid membrane similar thickness values as for C8-DNBDT were obtained as well.

Higher SLD, thickness and roughness values of the lipid head groups suggest that an increased uniformity and density of the DOPC membrane is achieved on C9-DNBDT. The observed increase in SLD and *d* of the DNBDT layer compared to the C8-semiconductor, while σ stays constant, suggests a tighter packaging of the semiconductor phase. This is possibly achieved by an improved immobilization and suppression of thermal fluctuation and thus increased stability of the film due to the stronger hydrophobic interaction of the longer C9 alkyl chains. However, an increased roughness at the interface between lipid alkyl chains and C9-DNBDT was determined, which could be caused by the appearance of larger islets, as seen in AFM measurements.

6.3 Homogeneity and Fluidity of the Lipid Monolayer

To further investigate the membrane formation and its self healing properties, a lipid monolayer using DOPC (2 mg/ml) with 0.2 mol% texas-red-DHPE was deposited by vesicle fusion on a cover slip coated with C8-DNBDT. By recording fluorescence images of the deposited membrane the quality and homogeneous distribution of fluorescence intensity was verified. Using FRAP the fluidity of the membrane was quantified by determination of the lateral diffusion coefficient *D* of lipids. The membrane deposition on C9-DNBDT was not investigated, since only the C8-DNBDT samples were provided on glass substrates. The inset in Figure 6.4a shows that a homogeneous coverage with a DOPC monolayer on C8-DNBDT is achieved with little defects, supporting the "healing" of defects by the lipid monolayer observed by XRR. This is aided by the high lateral diffusion coefficients of the membrane, determined by FRAP measurements with a bleach spot with the radius of 5.75 µm. From 3 independent measurements a diffusion coefficient of $D_{DOPC} = 1.6 \pm 0.1$ µm^2/s was obtained for the DOPC membrane. This value is comparable to the values on hydrophobic polymer supports of $D = 1.0 – 1.5$ µm^2/s (Sigl et al. 1997). The high homogeneity and fluidity of the membrane achieved confirm that the well ordered layers of octyl chains in the C8-DNBDT crystals can be employed as an excellent support for lipid membranes. Membrane formation was stable and showed little defects for at least three cycles of membrane deposition and removal with isopropanol on the same sample.

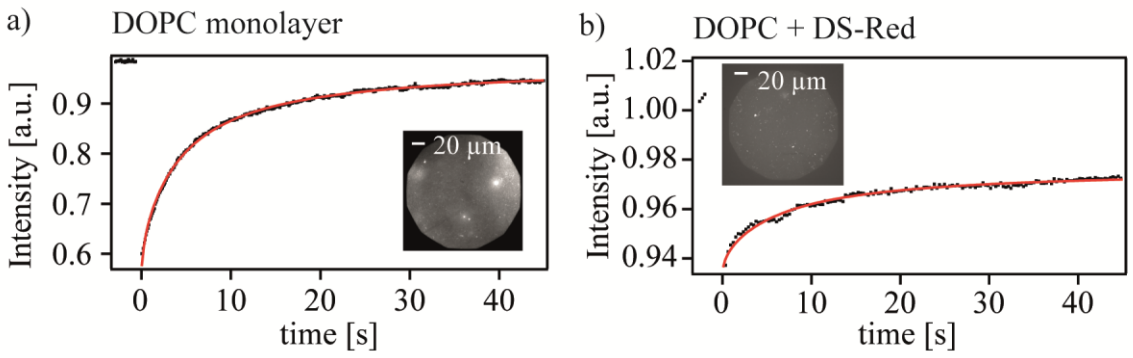

Figure 6.4: (a) *FRAP and Fluorescence image (inset) of C8-DNBDT with DOPC monolayer containing 0.2 mol % texas-Red. b) Homogeneity and mobility of the recombinant proteins anchored on the lipid monolayer. FRAP and Fluorescence image (inset) of C8-DNBDT with lipid DS-Red stained lipid monolayer containing 2 mol % DGS-NTA.*

To determine the mobility of anchored recombinant proteins in the membrane, 2 mol% DGS-NTA was incorporated in the DOPC vesicles. His-tagged DS-red monomers were added to the sample after vesicle fusion and incubated for further 30 min at 38°C. Here DS-red was used since its excitation wavelength ($\lambda_{ex,DS\text{-}red}$ = 561 nm) does not conflict with the auto fluorescence of C8-DNBDT ($\lambda_{ex,C8\text{-}DNBDT}$ = 488 nm) (see Supplementary Information section 9.1.4). Assuming a homogeneous distribution of DGS-NTA, 2 mol% in the lipid phase correspond to an intermolecular distance of 5.7 nm (Frenkel 2015). With the diameter of a DS-red monomer of ~ 6 nm, this constitutes to a full coverage of the surface. The inset in Figure 6.4b indeed shows a mostly homogeneous distribution of DS-red in on the membrane, however with few aggregates formed and a lower intensity than the membrane with texas-red-DHPE. The observed diffusion coefficient $D_{DS\text{-}red}$ = 1.5 ± 0.3 µm^2/s is similar to the pure DOPC membrane and suggests that the binding of recombinant proteins imposes no restriction to the membrane fluidity and self healing properties. However, some restriction in the lateral diffusion of lipids is seen from the decrease in mobile fraction. Compared to the pure DOPC membrane, with approximately 90 % mobile lipids, the mobile fraction of immobilized DS-red proteins is only 63 %. This restricted mobility is possibly caused by the high surface coverage achieved with 2 mol% DGS-NTA, causing a tighter conformation of DS-red proteins on the surface and a higher degree of immobilization.

6.4 I-V Characteristics

The base operation of the provided transistor structures of both C8- and C9-DNBDT on Si substrates (Figure 6.1b) in aqueous medium was investigated before membrane deposition. Threshold voltage V_{th} and transconductance g values were extracted from linear regression in the measured transfer curves between V_G = – 5 V and 5 V for C8-DNBDT and between V_G = – 15 V and – 20 V for C9-DNBDT and are summarized in Table 6.4. The Performance of the C8-compound was first tested in air by using three contact pins with one acting as a back gate contact and the other two as source and drain contacts. Even in air C8-DNBDT expressed instability between subsequent measurements, in the observed threshold voltage ($\Delta V_{th,-20V}$ = 11 V), especially at the applied drain voltage of – 20 V (Figure 6.5a). This change in V_{th} interestingly is much less pronounced at V_{DS} = – 10 V, with only $\Delta V_{th,-10V}$ = 2 V observed. The transconductance though, was not strongly affected and was comparable between the two measurements for both applied drain voltages. Compared to the values of a similar compound (Mitsui, Okamoto et al. 2014) much higher V_{th} and lower currents $I_{DS, max}$ at V_G = – 20 V than expected were contained. This suggests a possible degradation of the semiconductor layer even in air, which could be caused by large scale defects observed for C8-DNBDT.

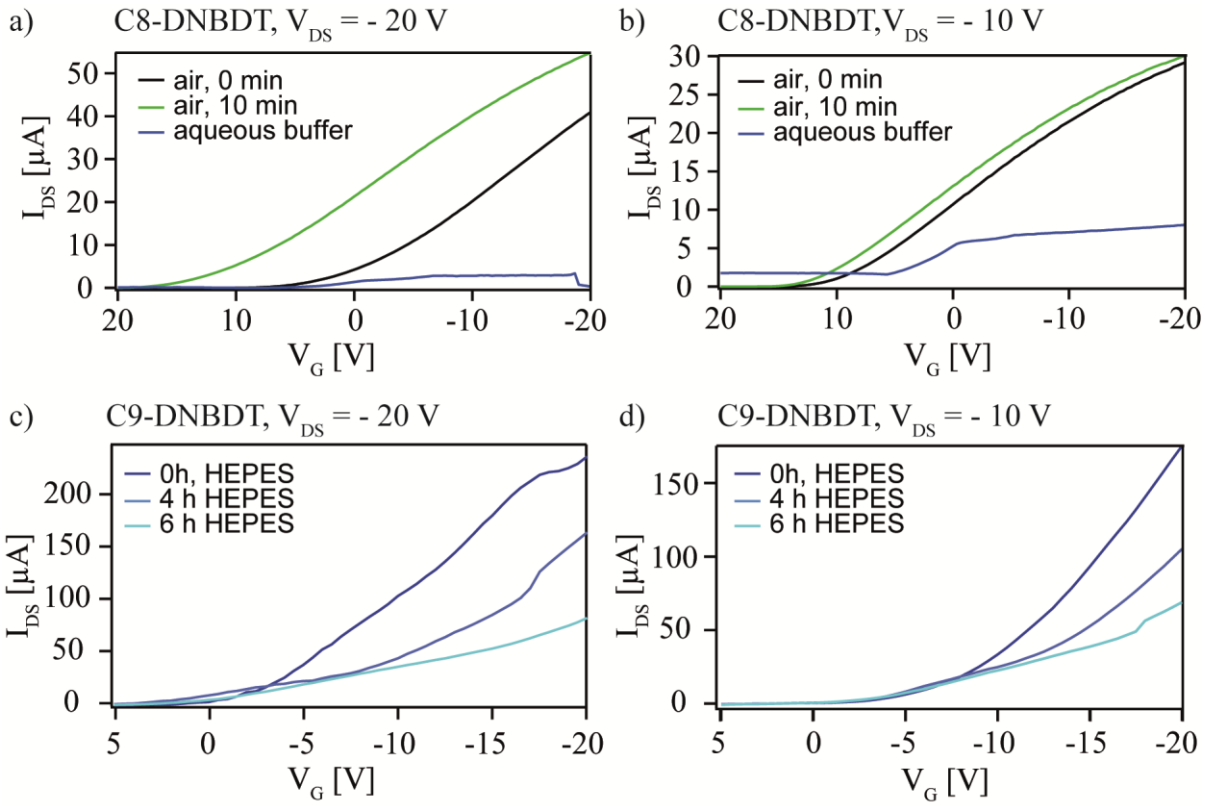

Figure 6.5: *Transfer curves of C8-DNBDT at (a) V_{DS} = – 20 V and (b) V_{DS} = – 10 V in air and aqueous buffer (HEPES). Transfer curves at (c) V_{DS} = – 20 V and (d) V_{DS} = – 10 V of C9-DNBDT in aqueous buffer. I_{DS} after subtraction of leak current are shown.*

Further measurement of the C8-DNBDT transistor in HEPES buffer led to an almost complete loss in conductance. This loss of conduction could be caused by partial dissolution of the semiconductor phase and water penetration into defects, creating a conduction path between gate and drain electrode and thus disrupting the transistor operation. Due to the already high variation of the transistor output in air and strong decrease of conduction in aqueous buffer, lipid membranes were not deposited on the C8-DNBDT samples.

Table 6.4: *Summary of threshold voltage V_{th} and transconductance g extracted from linear regression between V_G = – 5 V and 5 V for C8-DNBDT and between V_G = – 15 V and – 20 V for C9-DNBDT.*

measurement	g [µS] (–10V)	V_{th} [V] (–10V)	g [µS] (–20V)	V_{th} [V] (–20V)
C8-DNBDT air, 0 min	1.1	9.5	2.1	0.3
C8-DNBDT air, 10 min	1.1	11.6	1.9	11.5
C9-DNBDT 0h, HEPES	16.6	– 9.5	14.9	2.6
C9-DNBDT 4h, HEPES	10.7	– 10.3	12.5	– 7.1
C9-DNBDT 6h, HEPES	6.8	– 9.8	4.7	2.5

From the better quality of the organic semiconductor film determined by AFM and XRR, an improved operation in the transistor *I-V* characteristics is expected for C9-DNBDT. Indeed the transistor performance of C9-DNBDT could be confirmed in buffer conditions, as shown in Figure 6.5c and d. Higher currents $I_{DS,\,max}$ at $V_G = -20$ V than for C8-DNBDT in air were obtained, confirming the increased quality of the of the C9 organic semiconductor film. Large leak currents (I_G) up to 100 µA were observed (see Supplementary Information section 9.1.4) even after careful insulation of the source and drain contacts from the surrounding electrolyte. This however causes most of the observed current to run between the source and gate electrodes and not to rech the drain electrode. These currents were subtracted from I_{DS} shown in Figure 6.5. The obtained I_{DS} current levels at the source electrode and V_{th} at $V_{DS} = -10$ V (Table 6.4) were comparable to similar C10 compound previously reported (Mitsui, Okamoto et al. 2014). V_{th} were largely constant over several hours as well, but displayed a large shift between the two drain voltages applied. Degradation in the transistor performance over time however was also observed, primarily in the decrease in $I_{DS,\,max}$ and thus transconductance *g*. Transconductance values decreased approximately 60% over 6h at both applied drain voltages. This can also be explained by partial dissolution of the semiconductor phase at the lamella like crystal edges, increasing the barrier for conduction and leading to a reduction in electron mobility in the semiconductor crystal. Thus an increase in resistance and decrease in transconductance is observed. In further experiments the stabilization of the C9-DNBDT semiconductor by membrane deposition will be investigated.

6.5 Summary

The C9-DNBDT semiconductor showed the most promise as membrane support from high film homogeneity measured in AFM as well as high semiconductor layer and lipid membrane density determined by XRR. Further, repeatedly high membrane uniformity and mobility of a DOPC membrane could be achieved on C8-DNBDT. The *I-V* characteristics of C8-DNBDT however showed too large instabilities in V_{th} and drastically reduced conductivity in aqueous buffer for further investigation. For C9-DNBDT though, the transistor operation could be confirmed in buffer conditions. Here, determined V_{th} were largely stable, but transconductance values decreased approximately 60% over 6h, showing the necessity for stabilization of the semiconductor phase in aqueous medium. This could be achieved by covalently linking the semiconductor SAM to the surface or introduction of thin stabilizing coating or possibly membrane deposition.

7. Conclusions

In this thesis new electrochemical biosensor systems were fabricated to transduce biological functions of lipid membrane systems and bio-inspired molecules into electrical readouts.

In Chapter 4, a new strategy for the modulation of electronic band structures of GaN semiconductors and GaN/AlGaN/GaN HEMT heterostructures was examined using the macromolecular dipole potentials induced by synthetic α-helical peptides. Functionalization steps of the substrates with aminosilane (APTES) and formyl terminated peptides (F8OME, Boc8F and F8Fc) were first optimized on bulk GaN electrodes. The same functionalization protocol was then transferred onto GaN heterostructures. First the surface topography before and after peptide grafting was examined. A rise in rms roughness from σ = 3 Å before grafting to σ = 5 – 6 Å after grafting was determined for all peptides by contact mode AFM in an 1.5·1.5 μm^2 area, confirming that the deposition of peptides did not lead to a significant roughening of substrates. Thicknesses of 13 Å, 15 Å and 18 Å were determined from AFM scratching for F8Fc, F8OMe and Boc8F respectively, further confirming the formation of a peptide monolayer. Additionally, XPS spectra were taken before and after each functionalization step, exhibiting a decrease in peak intensity for both Ga3d and N1s after subsequent formations of the APTES and peptide layers. Presence of the Fe2p peak from the ferrocene moiety was detected as well for the F8Fc peptide. Fine structures of the stratified layers were further obtained by XRR within Ångström accuracy, yielding the peptide layer thickness of d_{F8Fc} = 14.8 Å, d_{F8OMe} = 16.4 Å and d_{Boc8F} = 16.9 Å, which agree well with results from AFM scratching. These obtained peptide thicknesses were lower than their theoretical length, suggesting a tilted conformation of the peptide helix with tilt angles determined to θ_{F8Fc} = 55.3°, θ_{F8OMe} = 30.3° and θ_{Boc8f} = 35.5°. The areas occupied by one peptide molecule could be estimated as well from the XRR results to A_{F8Fc} = 185 $Å^2$, A_{F8OMe} = 174 $Å^2$ and A_{Boc8F} = 134 $Å^2$.

In the next step, the electrochemical properties of the grafted peptide layer was investigated on bulk GaN electrodes with a doping ratio of $N_D = 1 \cdot 10^{20}$ cm^{-3} to ensure a high detection sensitivity. Electrochemical impedance spectroscopy was employed over a wide frequency range (100 kHz – 50 mHz) to discriminate changes in the resistive and capacitive contributions in the semiconductor upon peptide grafting. Using equivalent circuit models variation in the space-charge capacitance C_{SC}, peptide layer capacitance C_{pep}, phase transfer resistance R_{PT} and Warburg impedance W were determined, as well as the flat band potential U_{FB} from Mott-Schottky analysis. A linear behavior in the Mott-Shottky plots was observed for all peptides, ensuring that the semiconductor operates in

the depletion region, where it is highly sensitive towards capacitance changes. Here, the GaN semiconductor exhibited a change in C_{SC} dependent on the direction of the peptide dipole potential. Both F8OMe and F8Fc peptides, whose dipole moments point towards the GaN interface, caused an similar increase in C_{SC} from $C_{SC(APTES)}$ = 3.88 μFcm^{-2}, prior to peptide grafting, to $C_{SC(F8OMe)}$ = 4.33 μFcm^{-2} and $C_{SC(F8Fc)}$ = 4.39 μFcm^{-2}. For the Boc8F peptide conversely, the dipole moment direction is inverted and a decrease in C_{SC} to $C_{SC(Boc8F)}$ = 3.26 μFcm^{-2} was observed. This dependency on the dipole direction was also reflected in the changes in U_{FB} that were determined to $\Delta U_{FB,F8Fc}$ = 0.23 V, $\Delta U_{FB,F8OMe}$ = 0.21 V and $\Delta U_{FB,Boc8F}$ = – 0.12 V. Additionally, Cyclic voltammetry confirmed the possible electron transfer through the peptide layer for the F8Fc peptide by the appearance of distinct oxidation peaks at U = – 0.16 V. The anodic reduction peaks however could not be clearly discerned at lower scan speeds. The standard electron transfer rate constant k_{et}^{0} = 0.91 s^{-1}, determined by chronoamperometry meanwhile suggested that the electron transfer can occur via an inelastic hopping mechanism along the peptide helix.

Finally, the grafting protocol was transferred onto GaN/AlGaN/GaN heterostructures Transfer and output curves were measured after each functionalization step to record changes in the transistor *I-V* characteristics. For this threshold voltage V_{th} and transconductance *g* values were determined from the linear region in the transfer curves. Similar to the changes in U_{FB}, an increase in V_{th} of ΔV_{th} = 140 for F8Fc, ΔV_{th} = 160 mV for F8OMe and a decrease of ΔV_{th} = – 140 mV for Boc8F were observed upon peptide grafting, caused by the different polarity of the dipole potential exerted by the peptide helix. From the transistor output curves these dipole potentials could be determined to $\Delta V_{G(F8Fc)}$ = – 0.16 V, $\Delta V_{G(F8OMe)}$ = – 0.29 V and $\Delta V_{G(Boc8F)}$ = + 0.28 V, allowing in turn the calculation of the macromolecular dipole moments exerted perpendicular to surface by the peptides to ρ_{F8OMe} = – 8.1 D, ρ_{Boc8F} = 7.1 D, and ρ_{F8Fc} = – 5.5 D. These measurements demonstrated that a higher sensitivity towards the molecular dipole moment could be reached on GaN heterostructures than for other semiconductor materials.

In Chapter 5.2, GaN heterostructures were functionalized with planar ODTMS supported lipid membranes to create a novel electrical sensor platform for the detection of the reversible recombinant protein binding on lipid monolayers. Using a defined amount of lipid anchors with NTA head groups (DGS-NTA (Ni)), which allows for the complexation of histidine-tagged recombinant proteins (e.g. eGFP), this system enables the transduction of the surface charge density variations ΔQ, induced by reversible complexation/de-complexation of chelator lipids and histidine-tagged proteins, into changes in the HEMT *I-V* characteristics. First the deposition of the ODTMS support with

low roughness σ = 0.9 nm was verified by AFM on bulk GaN substrates. The formation of a well defined and homogeneous lipid monolayer further confirmed by XRR and fluorescence microscopy on Si and glass substrates respectively. This monolayer system was then transferred on the GaN heterostructure and its *I-V* characteristics recorded at the different monolayer charge states (Ni-loaded, eGFP-loaded and unloaded).

For the lipid monolayer containing 2 mol% NTA lipids, the threshold voltage V_{th} determined from the linear region in the transfer curves exhibited a clear increase from the Ni-loaded state; $V_{th,\ Ni}$ = – 2.59 V upon complexation of eGFP; $V_{th,\ GFP}$ = – 2.48 V, while the transconductance *g* was constant throughout all measurements. The dissolution of the Ni-histidine-complex by EDTA showed a further increase in V_{th} to $V_{th,\ unloaded}$ = – 2.37 V. While the reversibility of the Ni loading/unloading has been shown, the reproducibility of the protein docking has yet to be verified.

Using 0.5 mol% NTA lipids, the switching between Ni-loaded; $V_{th,\ Ni}$ = – 2.37 V and Ni-unloaded states; $V_{th,\ unloaded}$ = – 2.29 V were still distinguishable. However, only a minor increase in V_{th} after eGFP complexation to $V_{th,\ GFP}$ = – 2.34 V that is near the thermal fluctuation in the *I-V* characteristics was observed. With this amount of NTA lipids it could be demonstrated that a sensitivity of ΔQ < 0.1 μCcm^{-2} can be reached, which corresponds to the sensitivity to a change in one elemental charge in less than 130 nm^2. The high sensitivity achieved demonstrates the further potential of this GaN HEMT sensor platform for other processes occurring at the membrane, such as antibody/antigen recognition and cell-cell interactions.

In Chapter 5.3 the deposition of lipid membranes on GaN heterostructures coated with regenerated cellulose polymers was explored, in order to fabricate a sensor platform for the study of membrane and membrane protein functionalities. The use of the regenerated and hydrated cellulose polymer as a membrane support allows for the incorporation of trans- and integral membrane proteins in a nature like environment. First, the deposition protocol of the regenerated cellulose was optimized on Si substrates. A thickness *d* of 5 nm and hydrophilic surface with low roughness σ = 0.6 nm was confirmed by AFM, contact angle and ellipsometry measurements.

Lipid bilayer deposition on the hydrated cellulose was investigated by fluorescence microscopy with different lipid compositions and deposition methods, where membranes deposited by vesicle fusion and containing 40/20/40 mol% DMPC/DMTAP/cholesterol exhibited the highest homogeneity and stability. Diffusion coefficients of D_{DMPC} = 0.3 ± 0.1 μm^2/s were determined by FRAP for this membrane with a mobile fraction of 40%, indicating that the deposition of a dense membrane, which is limited in its self-healing properties, was achieved.

The impact of the membrane deposition on the GaN HEMT *I-V* characteristics was investigated in the next step. Here, consistent decreases in transconductance Δg of – 3 µS to – 4 µS were determined from the slope of the linear region in the HEMT transfer curves after membrane deposition by vesicle fusion. Further, interaction of enzymes with the membrane could be demonstrated by the digestion of phospholipids in the membrane by phospholipase A_2. After incubation with phospholipase A_2 the effects from the membrane deposition on the *I-V* curves was completely reversed. V_{th} after membrane formation however was inconsistent over multiple measurements. Nonetheless, these results demonstrate the first steps towards a sensor for the investigation of integral or trans membrane protein functions, such as ion channels. The incorporation of such proteins could lead to a modulation of Δg, depending on different ion species present in the buffer.

In chapter 6 the first steps towards a new class of biosensors utilizing novel organic semiconductor substrates provided by Prof. Dr. T. Okamoto and Prof. Dr. J. Takeya (Univ. Tokyo) is explored. N-shaped DNBDT molecules with octyl- (C8) and nonyl- (C9) alkyl chains self assemble into a highly conductive single crystalline layer. As observed by AFM a lamella like structure of the single crystals is formed, where, as evidenced by the higher roughness, a higher defect rate for C8-DNBDT (σ = 2.4 nm) was observed than for the C9 semiconductor (σ = 1.2 nm). Successful lipid monolayer formation over a wide area could be confirmed by XRR for both materials, whereas an increased *SLD* of the lipid head groups was determined for the C9-semiconductor, suggesting an improved monolayer density on this material. The homogeneity and fluidity of DOPC monolayers were verified by FRAP, yielding a high lateral diffusion coefficient of D_{DOPC} = 1.6 ± 0.1 µm^2/s and the mobile fraction of 90 %. The immobilization of DS-red monomers onto this monolayer led to no clear impact on the lateral diffusion ($D_{DS\text{-}red}$ = 1.5 ± 0.3 µm^2/s). However, a smaller mobile fraction of 63 % was detected for the immobilized proteins than for the pure lipid monolayer.

First tests to measure the *I-V* characteristics of C8-DNBDT in aqueous buffer resulted in the disruption of its conductive behavior. For C9-DNBDT, operation in aqueous buffer could be confirmed with relatively stable V_{th}. The transconductance of the transistor however decreased approximately 60% over 6h, indicating a degradation of the semiconductor material. These result indicated the need for further stabilization of the organic semiconductor layer in water.

In conclusion, novel hybrid bioelectronic materials could be fabricated by the combination of GaN-based semiconductor and heterostructures devices with biomimetic or biological systems, such as supported membranes and peptide monolayers, demonstrating high sensitivities towards changes in their electronic environment. These

materials proved to be a promising tool for the transduction and quantification of functions and processes in biological systems into an electronic readout.

8. Appendix I

8.1 Structural Characterization of Aptasensors on Graphene Oxide

Structural analysis of two different apatsensors for protein recognition, provided by Dr. Yuko Ueno and NTT Research Laboratories (Japan), was performed by XRR to confirm the mechanism of the sensor. The provided aptasensors were grafted with a pyrene linker onto a graphene oxide coated silicon wafer (Figure 8.1) and further consist of a specific single stranded aptamer sequence with a fluorescence dye coupled to it. In this state the fluorescence of the dye is quenched by the close proximity of the dye to the graphene oxide surface. Upon addition of the corresponding protein or aptamer sequence specific to the one used in the sensor the fluorescence signal is observed. As proposed by Ueno et al. the hybridization of the aptamer in the sensor causes the detachment of the dye from the surface and thus enabling the fluorescence (Furukawa, Ueno 2013, Ueno 2015).

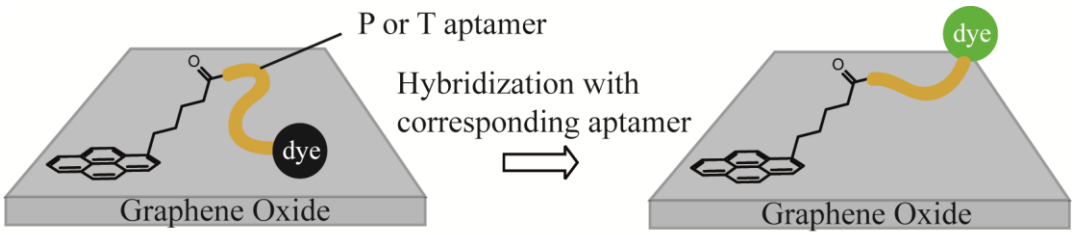

T-aptamer:
5‘-GGTTGGTGTGGTTGG-3‘(15 units)

P-aptamer:
5‘-TTTTTTTTTTCGATAAACTACCGCTCGAATTAATTT-3‘ (37 units)

Figure 8.1: *Schematic illustration of the aptasensor on graphene oxide. Before hybridization the single stranded aptasensor is collapsed and the fluorescence dye is quenched by the graphene oxide. After hybridization with the corresponding strand, the dye is lifted up and the fluorescence signal is observed.*

The two aptamer sequences used for the analysis of structural changes upon hybridization are abbreviated with T for the sequence with 15 nucleic acids and P for the sequence with 37 units (Figure 8.1). Both aptamer sequences were used without fluorescence dyes.

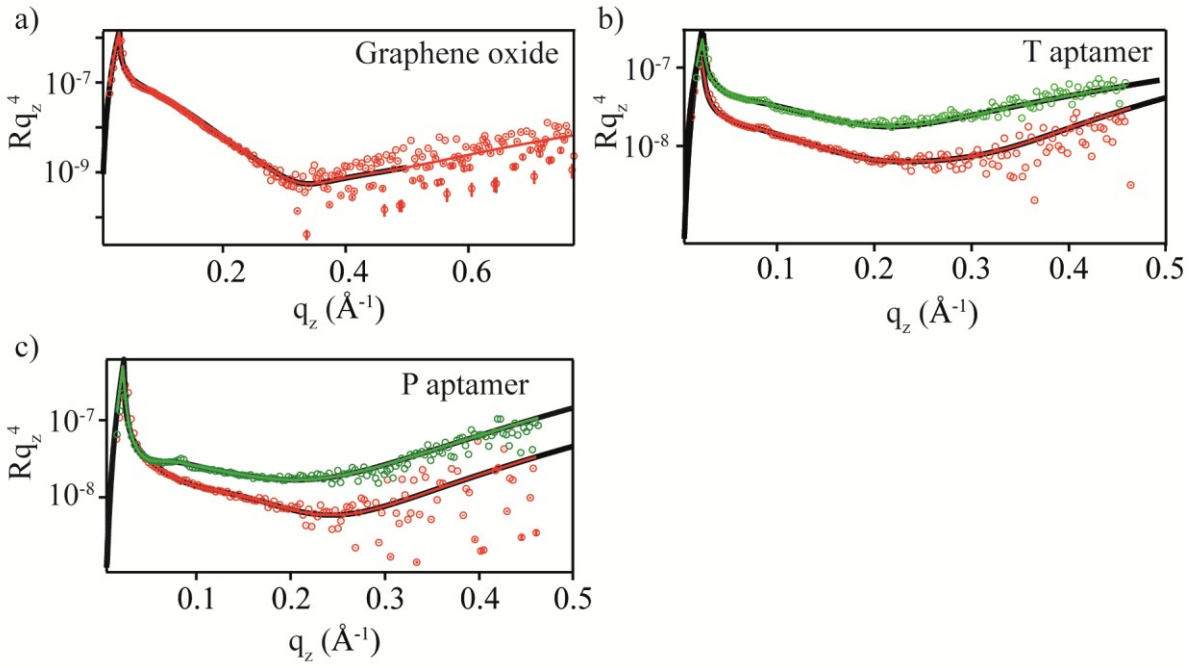

Figure 8.2: *XRR curves in Fresnel plot of (a) the graphene oxide on Si in air, (b) T aptamer before (red) and after (green) hybridization and (c) P aptamer before (red) and after (green) hybridization in aqueous buffer. Symbols represent the experimental data and the solid lines the fitting result respectively.*

Thickness d, scattering length density (SLD) and roughness σ parameters were determined by XRR for the graphene oxide layer without aptasensor and with the grafted aptasensor before, as well as after hybridization using the slab model for each layer. Figure A.B shows that the data could be well fitted with a two slab model for the native SiO_2 and graphene layers and a three slab model for the additional aptamer layer. The best fit parameters are summarized in Tables 8.1 – 8.5. The native SiO_2 thickness for all samples was 12 – 13.5 Å, while the obtained roughness was 3.5 – 4.5 Å. For the graphene layer a thickness of 8.3 Å with roughness of 6.6 Å was obtained (Table 8.1), suggesting a mostly uniform layer. The SLD of $14.7 \cdot 10^{-6}$Å^{-2} is in a good agreement with the SLD estimated from the density of natural graphite ($17.8 \cdot 10^{-6}$Å^{-2}).

Table 8.1: *Best fit parameters ($\chi^2 < 0.02$) for graphene oxide layer on Si in air*:

layer	thickness [Å]	SLD [10^{-6}Å^{-2}]	roughness [Å]
graphene oxide	8.3	14.7	6.6
native SiO_2	12.8	18.9	3.5

Comparable parameters for the graphene layer were also obtained for the samples with deposited aptamer. The SLD obtained for the T aptamer before hybridization ($SLD_{T,ss}$ = $7 \cdot 10^{-6}$Å^{-2}) agrees well with half of the value expected for double stranded DNA

($11.6 \cdot 10^{-6}$ Å^{-2}) (Erokhina 2007). Assuming the length of 3.4 Å per nucleic acid the expected length for the short T aptamer (15 units) is about 51 Å. However, the obtained thickness $d_{T,ss}$ = 6.5 Å (Table 8.2) of the layer is significantly lower. This can be explained by the persistence length of 2.2 nm of single stranded DNA (Chi 2013) lower than the theoretical length of the aptamer, causing the collapse of the aptamer to the surface.

Table 8.2: *Best fit parameters ($\chi^2 < 0.02$) for the single strand (ss) T aptamer in aqueous buffer (10 mM PBS, 100 mM NaCl, pH 7):*

layer	thickness [Å]	SLD [10^{-6} Å^{-2}]	roughness [Å]
T aptamer (ss)	6.5	7	5.3
graphene oxide	8.4	14.8	4.1
native SiO_2	13.5	18.9	3.5

After hybridization by incubation for 4h at 37 °C with a 50µg/ml solution of the complementary T aptamer to the double stranded aptasensor, a clear change in the curve profile can be seen (Figure 8.2b and c), suggesting a significant change in the aptamer layer.

Table 8.3: *Best fit parameters ($\chi^2 < 0.02$) for the double stranded T aptamer after hybridization in aqueous buffer (10 mM PBS, 100 mM NaCl, pH 7):*

layer	thickness [Å]	SLD [10^{-6} Å^{-2}]	roughness [Å]
T aptamer (ds)	21.2	11.4	28.3
graphene oxide	8.4	12.8	6.9
native SiO_2	12.9	18.9	3.5

A major increase in thickness to 21.2 Å and roughness to 28.3 Å with a rise in SLD, which is in a good agreement with the expected SLD of a double stranded DNA, is observed (Table 8.3). These findings confirm the successful hybridization of the aptasensor and suggest a change in layer conformation and detachment of the aptasensor from the surface. With the persistence length of ~50 nm (Manning 2006) for the double stranded DNA, that is far larger than the estimated length of the aptasensor, the hybridized aptasensor is more rigid and takes up a rod-like, tilted conformation. The estimated tilt angle from the theoretical and obtained layer thickness is 65° from the surface normal.

A similar trend is observed for the longer P aptamer (37 units) with a theoretical length of 125 Å. In case of the single stranded aptasensor before hybridization the obtained thickness and SLD is about twice as high as for the shorter T aptamer (Table 8.4).

Additionally a significantly larger roughness of 16.2 Å is observed as well. While the low thickness of 13.7 Å compared to the expected aptamer thickness suggests the collapsed state of the aptasensor, the increased SLD and roughness could be caused by the formation of aptamer stacks. As the P aptamer length far exceeds the persistence length of the single stranded DNA, the aptamer chain can take a random orientation and conformation.

Table 8.4: *Best fit parameters (χ^2 < 0.02) for the single strand (ss) P aptamer in aqueous buffer (10 mM PBS, 100 mM NaCl, pH 7):*

layer	thickness [Å]	SLD [10^{-6}Å^{-2}]	roughness [Å]
P aptamer (ss)	13.7	11.9	16.2
graphene oxide	8.5	12.4	4.6
native SiO_2	12.2	18.9	4.6

Upon hybridization a similar strong increase in the aptamer thickness to 60 Å and a similar roughness of 23.3 Å to the T aptamer is observed (Table 8.5). This confirms the detachement of the aptasensor from the surface, as the aptamer chain becomes more rigid. The tilt angle fron the surface normal of the double stranded T aptamer is estimated to 61°.

Table 8.5: *Best fit parameters (χ^2 < 0.02) for the double stranded P aptamer after hybridization in aqueous buffer (10 mM PBS, 100 mM NaCl, pH 7):*

layer	thickness [Å]	SLD [10^{-6}Å^{-2}]	roughness [Å]
P aptamer (ds)	60	11.2	23.3
graphene oxide	8.6	12.0	7.0
native SiO_2	12.0	18.9	3.5

The proposed mechanism of the detachment of the aptasensor upon hybridization with the corresponding aptamer can be confirmed from the increase in thickness and roughness after hybridization for both investigated aptamers. Fit parmeters after hybridization suggest a tilted conformation of the aptamers with a tilt angle of ~60°.

8.2 Electrochemical Analysis of a Liquid Crystalline Ion Selective Membrane on GaN

The electrochemical analysis for the ion selective membrane samples, kindly provided by Prof. Takashi Kato (Tokyo University), was performed with impedance spectroscopy and chronoamperometry on the bulk GaN semiconductor (N_d(Ge) = $5 \cdot 10^{19}$ cm^{-3}). The membrane deposited on GaN consists of wedge-shaped liquid crystal molecules with a small triethyl-amino head-group and larger hydrophobic body. This molecule polymerizes into bicontinuous cubic phase (Cub_{bi}) through nanosegregation between its ionic and non-ionic parts, and forms ionic nanochannels (Henmi, Kato 2012, Sakamoto 2018). The formed nanochannels have a pore size of ~ 0.6 nm and its walls are formed by triethyl-amino head-groups. This membrane shows high ion selectivity, where the permeation of monovalent anions is inhibited compared to divalent anions. For instance, with a thickness of 50 – 100 nm of the polymerized liquid-crystalline molecule, a rejection rate of 58 % for chloride ions and 33 % for sulfate ions was reported by Kato et al. (Henmi, Kato 2012). To investigate the anion selectivity of this membrane between mono and divalent anions, $MgSO_4$ (10 mM HEPES with 10 mM $MgSO_4$, pH = 6.5) and $MgCl_2$-Buffer solutions (10 mM HEPES with 10 mM $MgCl_2$, pH = 6.5) were used. Impedance spectra were first recorded at U_{bias} = ± 400 mV to simulate the working pressure of 0.75 MPa used by Kato et al. At U_{bias} = + 400 mV the membrane coated GaN electrode is negatively charged and the electric field between reference electrode and the GaN electrode causes cations to diffuse to the membrane and an cation pressure of 0.75 MPa. At U_{bias} = – 400 mV anions diffuse to the membrane, allowing the investigation of the anion selectivity. Ten measurements were taken for each salt and bias potential condition with additionally 10 min of bias potential applied before each measurement. To avoid hysteresis, the membrane was exposed to the continuous flow of deionized water for 1 h between the measurement cycles.

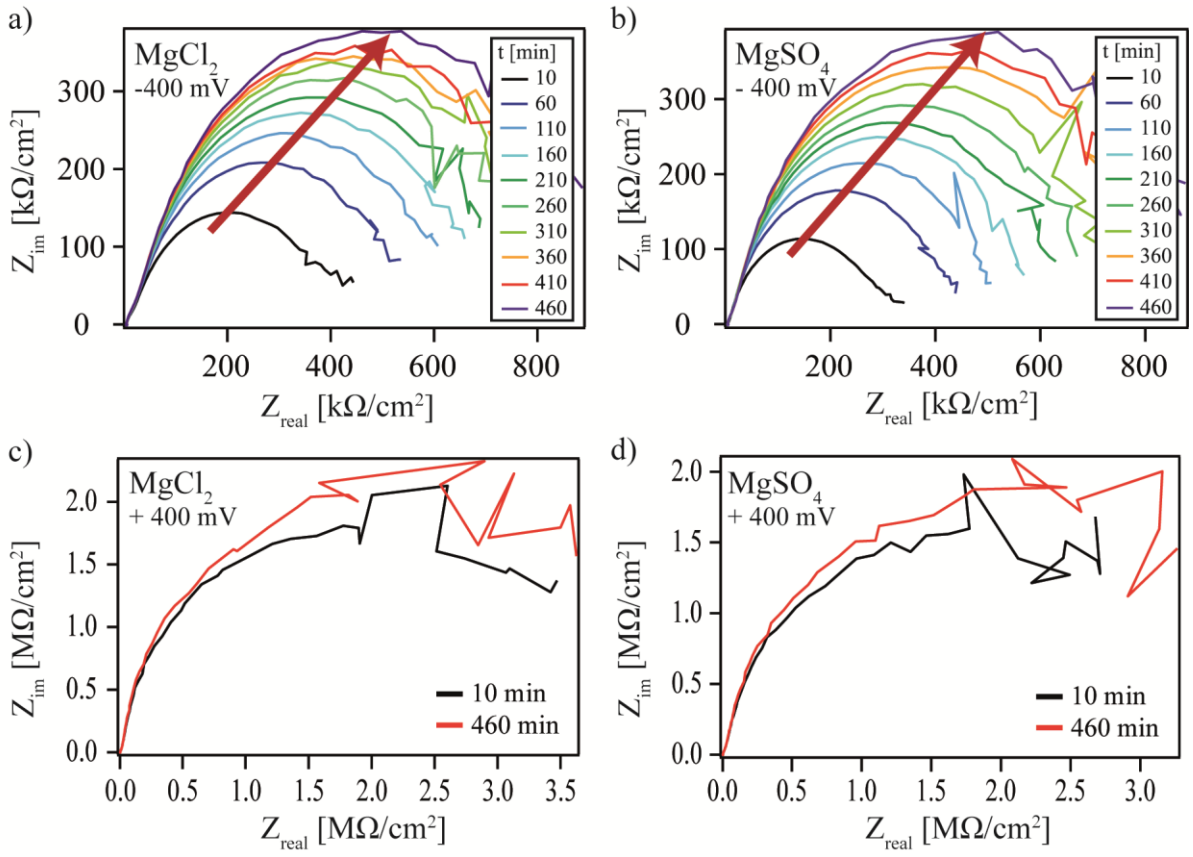

Figure 8.3: *Nyquist plot of the raw impedance data showing (a) a steady change in the spectra at negative applied bias potentials and (b) almost no change at positive U_{bias}.*

Figure 8.3 shows the Nyquist plots of the impedance spectra recorded over 7 h for both salt buffers used. At U_{bias} = + 400 mV no distinct changes in impedance observed, suggesting no permeation of cation into the membrane. At U_{bias} = – 400 mV however, a continuous change in the spectra is observed, confirming the permeation of anions into the membrane. All spectra were fitted with the equivalent circuit model 3 (see Figure 2.7, section 2.2.7) to investigate changes in semiconductor space-charge capacitance C_{SC}, membrane capacitance C_m, Warburg Impedance W and diffusion coefficient D through the membrane due to ion permeation. For the applied U_{bias} = – 400 mV, the changes in these parameters are depicted in Figure 8.4.

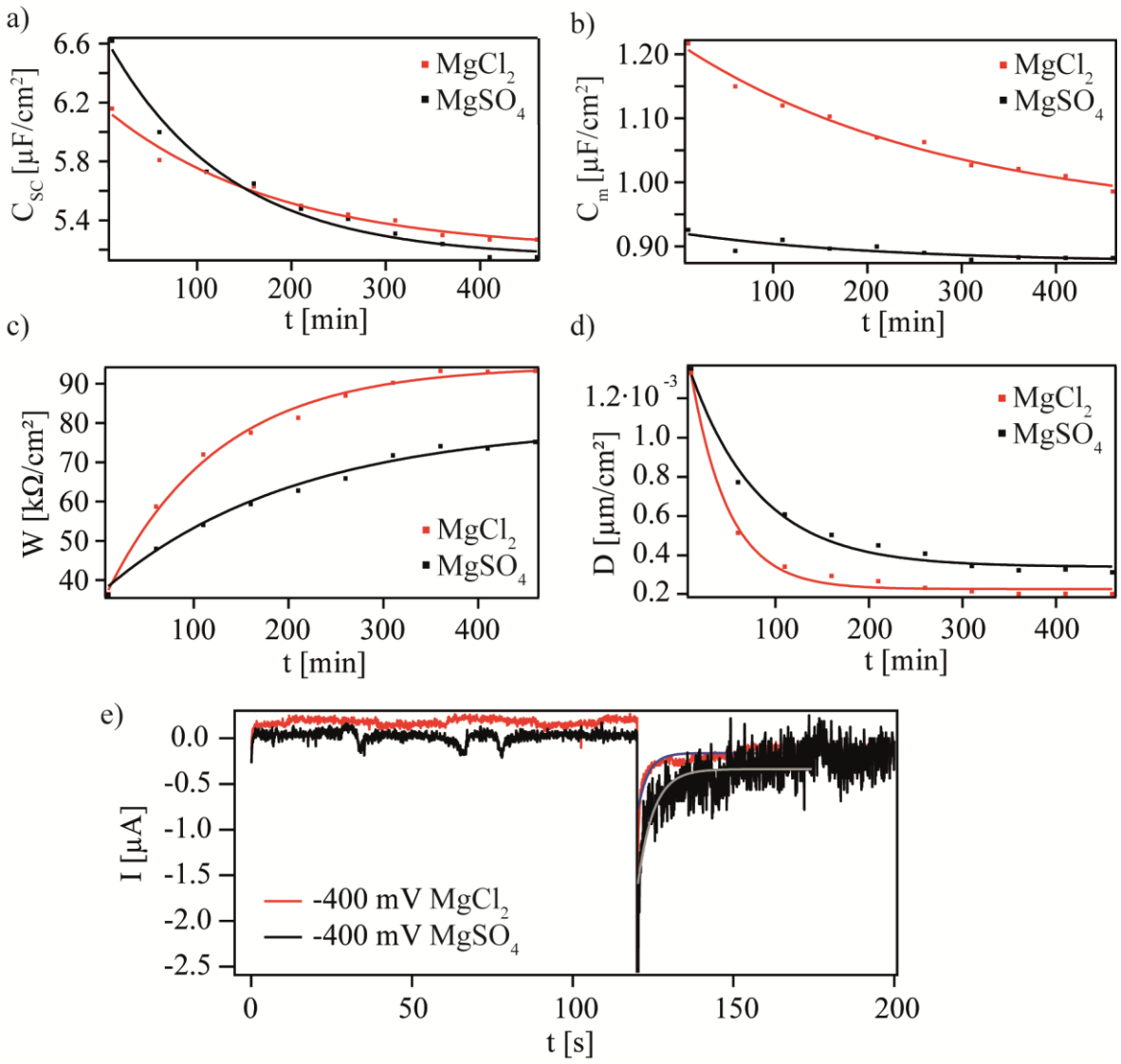

Figure 8.4: *Time dependent changes in (a) space-charge capacitance C_{SC}, (b) membrane capacitance C_m, (c) Warburg impedance W and (d) diffusion coefficient D, and chrono-amperometry of 10 mM $MgCl_2$ (red) and 10 mM $MgSO_4$ (black) at – 400 mV U_{bias}.*

For both sulfate and chloride a change in C_{SC} due to the permeation of ions through the membrane and accumulation at the GaN interface is observed (Figure 8.4a). The decrease in C_{SC} reaches a saturation level at 5.3 µF/cm^2 after 7 h. The change in C_{SC} is faster for sulfate ($\tau_{SO4,\ Csc}$ = 128 min) than for chloride ions ($\tau_{Cl,\ Csc}$ = 182 min), while C_m stays almost constant for SO_4^{2-} (Figure 8.4b), suggesting a faster permeation of SO_4^{2-} through the membrane. In contrast a decrease in C_m is observed for chloride ions, suggesting a more pronounced accumulation of chloride ions inside the membrane instead of permeation as seen for SO_4^{2-}. These findings support the observed anion selectivity of divalent anions over monovalent ions by Kato et al. There the selectivity is proposed to be caused by a stronger specific interaction of monovalent anions (Cl^-) with the nanochannel

walls (Henmi, Kato 2012). The Warburg element *W*, acting as resistance towards ion diffusion through the membrane, is at first similar for both salts (Figure 8.4c), but increases faster for Cl^- ($\tau_{Cl,W}$ = 118 min) with about half the characteristic time constant τ than for SO_4^{2-} ($\tau_{SO4,W}$ = 202 min). After 7 h a higher saturation level is reached for Cl^-. Due to the higher accumulation rate of Cl^- in the membrane the diffusion barrier of the Warburg impedance increases faster, causing the inhibition of further diffusion. With

$$Z_W \equiv W(\sigma_w) = \left(\sigma_w + \frac{1}{\sigma_w}\right)\omega^{-1/2}\,,\ \sigma_w = \frac{4RT}{\sqrt{2}n^2F^2A\rho}\,\frac{1}{\sqrt{D}} \qquad (2.48, 2.49)$$

the diffusion coefficients *D* of ions through the membrane were calculated (Figure 8.4d). A similar trend is seen as for *W*, where *D* decreases almost twice as fast for Cl^- ($\tau_{Cl,D}$ = 40 min) than for SO_4^{2-} ($\tau_{SO4,D}$ = 74 min). The diffusion coefficient *D* decays form $1.3\cdot10^{-3}$ $\mu m^2/s$ for both anions to $0.3\cdot10^{-3}$ $\mu m^2/s$ for SO_4^{2-} and $0.2\cdot10^{-3}$ $\mu m^2/s$ for Cl^- in 7 h. After the initial measurement *D* for Cl^- is always smaller than for SO_4^{2-}, further supporting the inhibition of Cl^- transport through the membrane compared to SO_4^{2-}. At U_{bias} = + 400 mV (cation transport) in contrast no sign of Mg^{2+} transport through the membrane could be detected, since C_{SC} remained constant at 2.2 $\mu F/cm^2$ over 7 h. Additionally large Warburg impedances ($W(MgSO_4)$ = 176 $k\Omega/cm^2$, $W(MgCl_2)$ = 137 $k\Omega/cm^2$) were observed, with the corresponding diffusion coefficients ($D(MgSO_4)$ = $2.5\cdot10^{-5}$ $\mu m^2/s$, $D(MgCl_2)$ = $4.2\cdot10^{-5}$ $\mu m^2/s$) that are one (after 7 h) to two (at the first measurement) orders of magnitude smaller than the values for anions. This suggests a very strong inhibition of Mg^{2+} diffusion into the membrane. In total the diffusion coefficients in the membrane are 6 (anions) to 8 (cations) orders of magnitude smaller than in bulk solutions ($D \sim 10^3$ $\mu m^2 s^{-1}$) (Poisson and Papaud 1983). Throughout all measurements membrane capacitances of C_m = 1.1 - 1.5 $\mu F/cm^2$ were observed. With,

$$C_m = \frac{\varepsilon_0 \varepsilon_m}{d_m} A \qquad (2.47)$$

the reported membrane thickness d_m = 50-100 nm, the permittivity of vacuum ε_0 and electrode area A = 0.5 cm^2 the dielectric constant of the membrane ε_m can be estimated to ε_m = 101 - 248. Thus, the membrane shows a larger dielectric constant than bulk water (ε = 80), that can be explained by the higher ion density inside the membrane nanochannels due to the permeation and accumulation of anions.

Chronoamperometric measurements were performed by applying U_{bias} = – 400 mV at t = 2 min, that was sustained for 1 h. For both anions the current level does not go back to the initial level even after 1 h, further suggesting the irreversible ion deposition in the membrane. The time constant τ of current recovery of SO_4^{2-} (τ_{SO4} = 4.8 s) is by a factor of 1.5 larger than Cl^- (τ_{Cl} = 3.2 s), implying that the transport of SO_4^{2-} is sustained over a

longer period. For U_{bias} = + 400 mV the current dropped back to the initial current level at U_{bias} = 0 mV within the first few seconds. The current signal in this case is only caused by capacitive effects at the electrode surfaces, thus further confirming that no permeation of cations through the membrane is occurring.

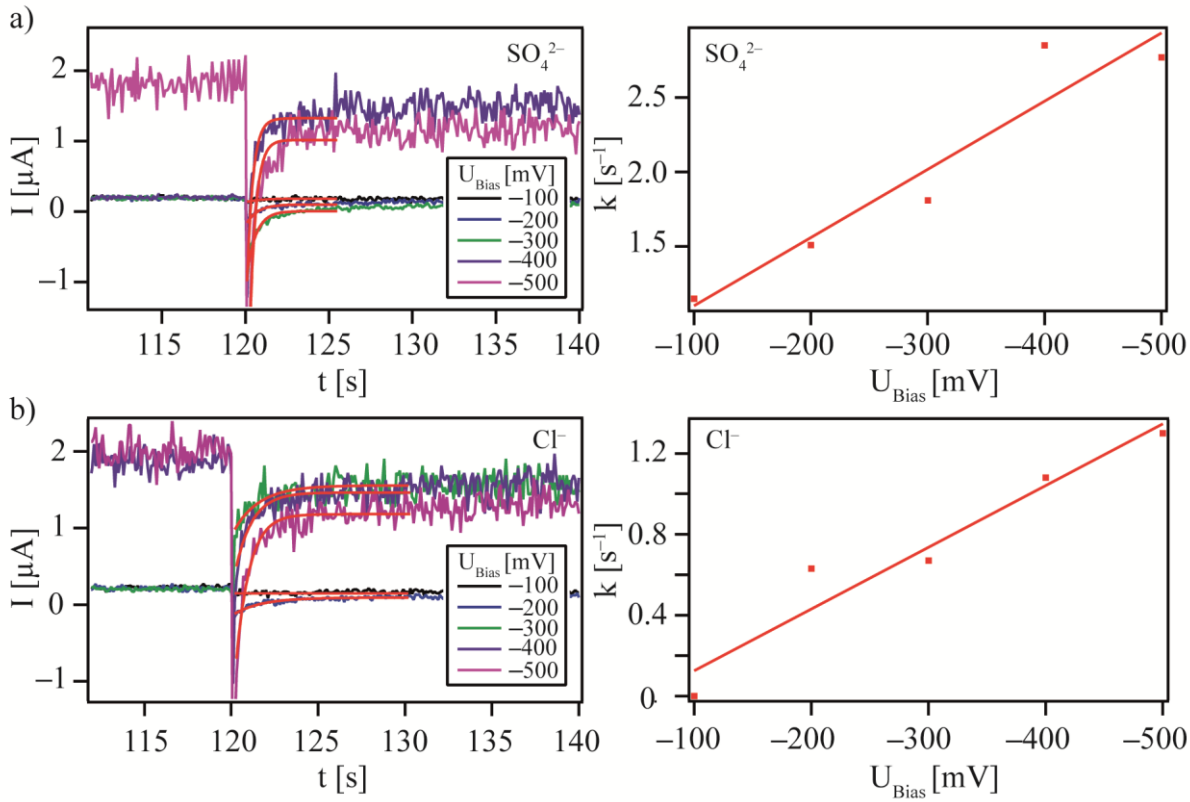

Figure 8.5: *Chronoamperometry (left) of the ion selective membrane on GaN (N_d(Ge) = $1{\cdot}10^{19}$ cm^{-3}) with 10 mM $MgSO_4$ (a) and 10 mM (b) $MgCl_2$ at bias potentials from – 100 mV to – 500 mV, applied at t = 120 s. The graphs on the right depict the transfer rates k through the membrane dependent on the applied U_{bias}.*

Further variation in the applied bias potential from – 100 mV to – 500 mV (Figure 8.5) showed a linear dependency of the transfer rate *k* through the membrane, confirming that the response function is diffusion controlled and well represented by Cottrell equation:

$$I(t) = nFAc_o\sqrt{\frac{D}{t}} \tag{2.59}$$

The standard electron transfer rate constant is obtained by linear extrapolation to U_{bias} = 0 V to k_{et}^0 = 0.18 s^{-1} for Cl^- and an almost three times larger rate of k_{et}^0 = 0.64 s^{-1} for SO_4^{2-}, further confirming the faster sulfate transport through the membrane.

From this data the selective transport of anion vs. cation could be confirmed. From the 1.5 – 2 times faster ion permeation and slower increase of *W* and decrease in *D* for SO_4^{2-}, the selectivity of anions (SO_4^{2-} vs. Cl^-) could be confirmed, while the stronger increase in C_m for Cl^- suggests a stronger interaction of monovalent anions with the membrane nanochannels. The 1.5 – 2 times difference in τ between SO_4^{2-} and Cl^- are also in a good agreement with the observed rejection rates of Kato et al. The faster transport of SO_4^{2-} was clearly detected by chronoamperometry as well, suggesting the irreversible deposition of anions at the GaN/membrane interface.

9. Appendix II

9.1 Supplementary Information

9.1.1 Surface topography of F8OMe, Boc8F and F8Fc

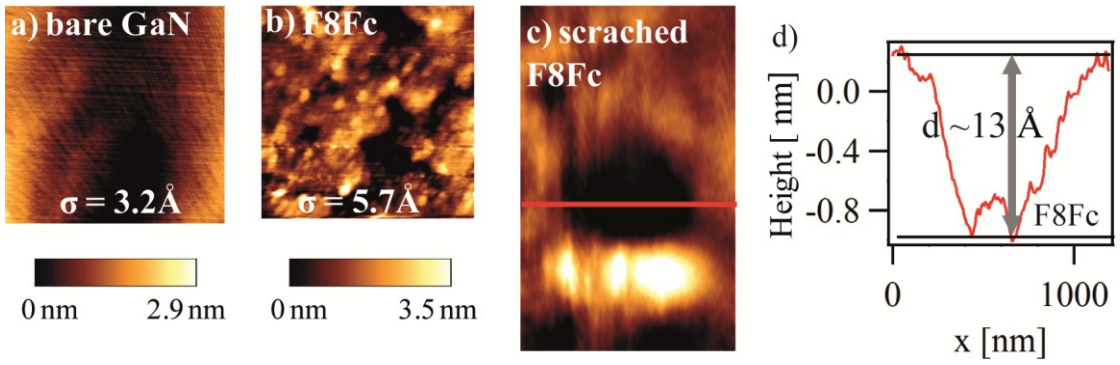

Figure 9.1: *AFM images of a bare, untreated GaN substrate (a) and after the deposition of F8Fc (b). The obtained rms roughness values from the 1.5 µm × 1.5 µm scan area are presented in insets. (c) AFM image of the 0.25 µm² scratch area and (d) Height profile of the scratch indicated with the solid red line. The height difference between the film surface and the scratch track (13 Å) suggests the formation of a peptide monolayer.*

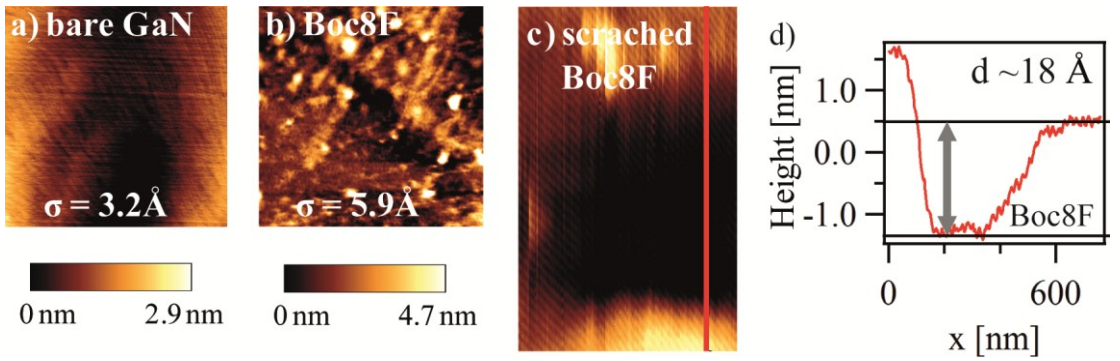

Figure 9.2: *AFM images of a bare, untreated GaN substrate (a) and after the deposition of Boc8F (b). The obtained rms roughness values from the 1.5 µm × 1.5 µm scan area are presented in insets. (c) AFM image of the 0.25 µm² scratch area and (d) Height profile of the scratch indicated with the solid red line. The height difference between the film surface and the scratch track (18 Å) suggests the formation of a peptide monolayer.*

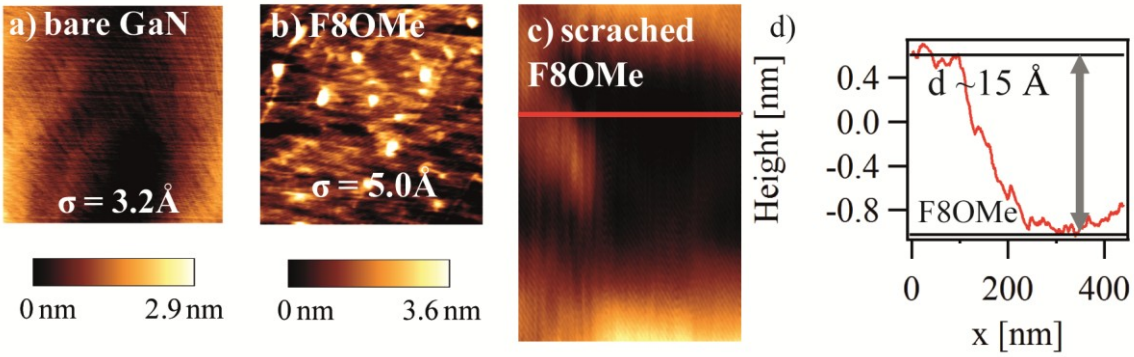

Figure 9.3: *AFM images of a bare, untreated GaN substrate (a) and after the deposition of F8OMe (b). The obtained rms roughness values from the 1.5 µm × 1.5 µm scan area are presented in insets. (c) AFM image of the 0.25 µm² scratch area and (d) Height profile of the scratch indicated with the solid red line. The height difference between the film surface and the scratch track (15 Å) suggests the formation of a peptide monolayer.*

9.1.2 Mott-Shottky Plot of Bulk GaN with Various Doping Ratios

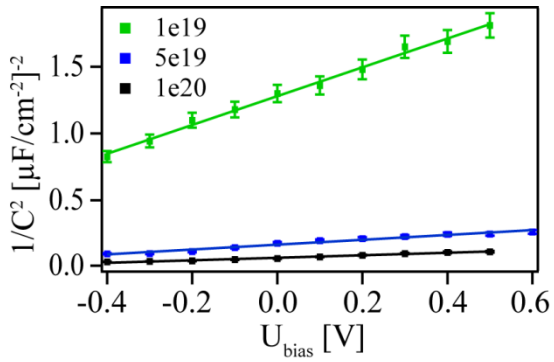

Figure 9.4: *Influence of carrier concentrations N_d in Mott-Schottky plot for different untreated GaN with the doping ratio of $N_d = 1{\cdot}10^{19}$ cm^{-3}(green), $5{\cdot}10^{19}$ cm^{-3}(blue) and $2{\cdot}10^{20}$ cm^{-3}(black) given by the manufacturer. Carrier concentrations calculated from the slope were $1.3{\cdot}10^{19}$ cm^{-3}, $6.3{\cdot}10^{19}$ cm^{-3} and $1.1{\cdot}10^{20}$ cm^{-3}. Flat-band potential were obtained from extrapolation of the linear regime to – 1.18 V, – 0.76 V and – 0.38 V respectively.*

9.1.3 Stability of GaN/AlGaN/GaN HEMT I-V Characteristics

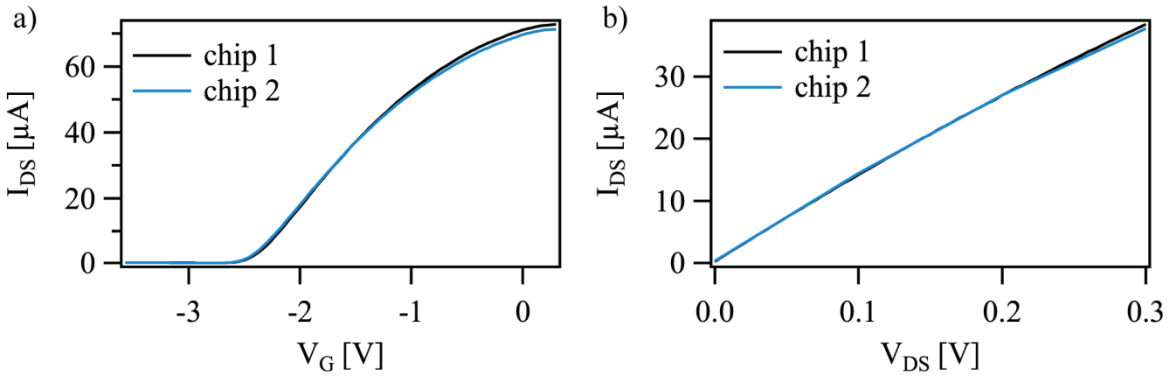

Figure 9.5: *I_{DS}-V_G curves from two uncoated HEMT chips produced from the same wafer measured at V_{DS} = 0.3 V. (b) I_{DS}-V_{DS} curves measured at V_G = – 1.5 V. Almost no changes in the curves were observed between the two chips.*

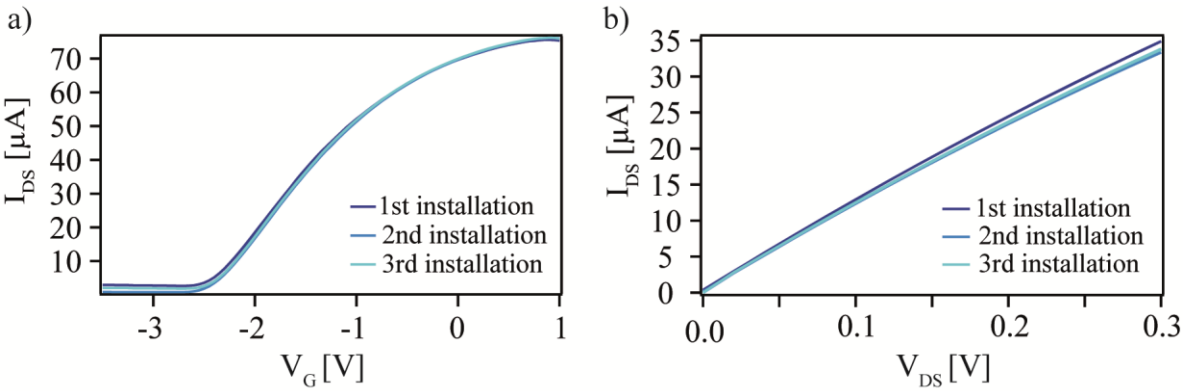

Figure 9.6: *Influence of repetitive dis- and remounting of the HEMT chip in the flow chamber. (a) I_{SD}-V_G curves measured at V_{SD} = 0.3 V and (b) I_{DS}-V_{DS} curves measured at V_G = – 1.5 V, showing almost no changes. An error range of ΔV_{th} = ± 17 mV and ΔI_{DS} = ±1.7µA, with low leak currents (I_G) < 100 nA were found from repeated installation of the same chip.*

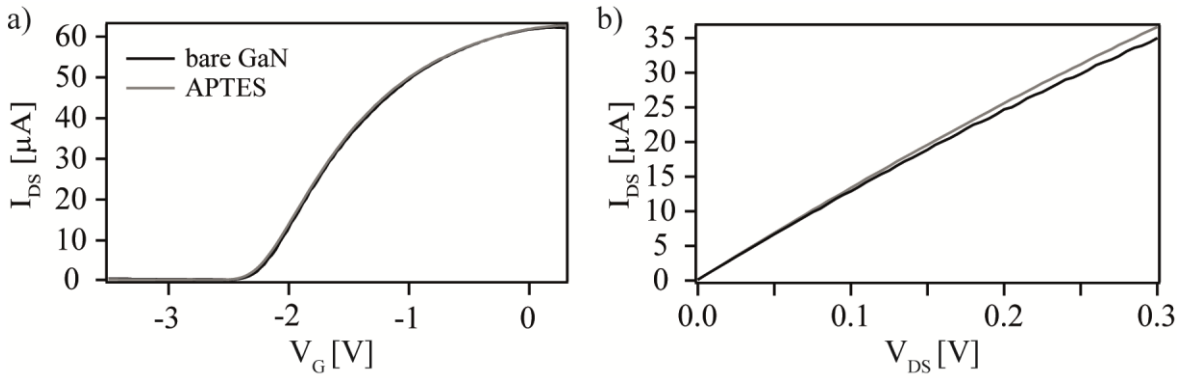

Figure 9.7: *Influence of APTES coating on I-V characteristics of the GaN HEMT. Comparison between the untreated GaN HEMT (black) and the ATPES coated HEMT (grey) shows almost no changes in (a) I_{SD}-V_G curves measured at V_{SD} = 0.3 V and (b) I_{DS}-V_{DS} curves measured at V_G = – 1.5 V.*

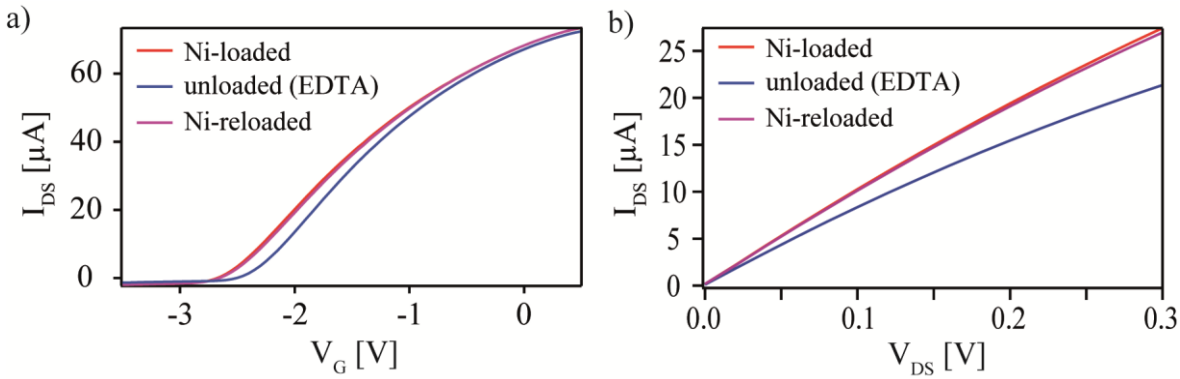

Figure 9.8: *Repetitive loading and unloading of the DMPC/cholesterol/DGS-NTA (63/35/2 mol%) monolayer with Ni^{2+}. (a) I_{SD}-V_G curves measured at V_{SD} = 0.3 V and (b) I_{DS}-V_{DS} curves measured at V_G = – 1.8 V show that the original Ni-loaded state could be reached again after unloading of the membrane with EDTA.*

9.1.4 Background Fluorescence and Leak Current of the DNBDT OFET

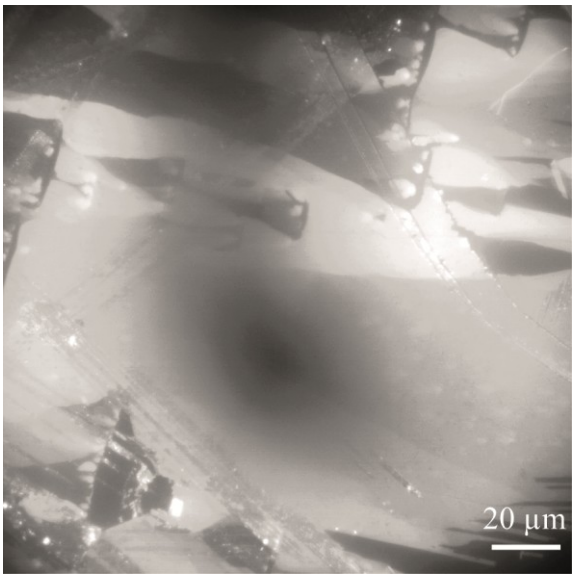

Figure 9.9: *Fluorescence image showing auto fluorescence of the single crystallites of the C8-DNBDT semiconductor prior to membrane fusion. Excitation wavelength is 488 nm.*

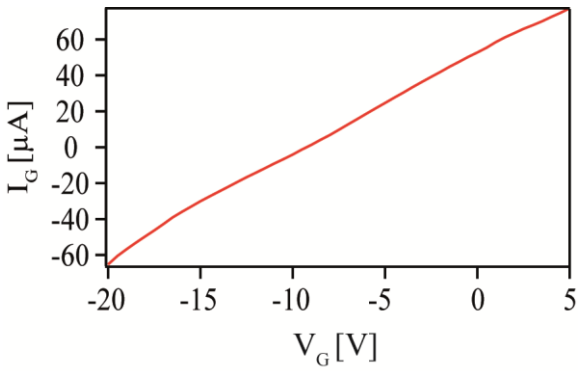

Figure 9.10: *Gate to source (Leak) current I_G of C9-DNBDT at V_{DS} = – 10 V.*

9.2 List of Abbreviations

2DEG	two dimensional electron gas
AFM	atomic force microscopy
Aib	α-amino isobutyric acid
APTES	(3-aminopropyl)triethoxysilane
CE	counter electrode
C_{GCS}	capacitance of the Gouy-Chapman-Stern layer
C_m	membrane capacitance
C_p	semiconductor interface capacitance
CPE	constant phase element
C_{pep}	peptide layer capacitance
C_{SC}	space-charge capacitance
C_{ss}	capacitance of surface states
CV	cyclic voltammetry
D	diffusion coefficient
DGS-NTA	*1,2-dioleoyl-sn-glycero-3-[(N-(5-amino-1-carboxypentyl)-iminodiacetic acid)succinyl]- nitrilotriaceticacid (nickel salt)*
DMTAP	*1,2-dimyristoyl-3-trimethylammonium-propane (chloride salt)*
DMPC	*1,2-dimyristoyl-sn-glycero-3-phosphocholine*
DNA	deoxyribonucleic acid
DNBDT	dinaphtho[2,3-*d*:2′,3′-*d*′]benzo[1,2-*b*:4,5-*b*’] dithiophene
DOPC	*1,2-dioleoyl-sn-glycero-3-phosphocholine*
DsRed	*discosoma red fluorescent protein*
ECM	*extra cellular matrix*
e.g.	exempli gratia
et al.	et alia
FET	field effect transistor
FRAP	fluorescence recovery after potobleaching
g	transconductance
HEMT	high electron mobility transistor

HEPES	4-(2-hydroxyethyl)-1-piperazineethanesulfonic acid
his-eGFP	histidin tagged green fluorescent protein
I_{DS}	drain to source current
IS	impedance spectroscopy
Leu	leucine
MOCVD	metal oxide chemical vapor deposition
ODTMS	octadecyl-trimethoxy-silane
OFET	organic field effect transistor
PBS	phosphate buffered saline
R_0	electrolyte resistance
RE	reference electrode
R_p	semiconductor resistance
R_{PT}	phase transfer resistance
R_{ss}	surface state resistance
SAM	self assembled monolayer
texas red DHPE	1,2-dihexadecanoyl-*sn*-glycero-3-phosphoethanolamine, Triethylammonium Salt
TMSC	trimethyl-silyl-cellulose
U_{bias}	working electrode to reference electrode bias potential
U_{fb}	flatband potential
V_{DS}	drain to source voltage
V_G	gate to source voltage
V_{th}	threshold voltage
W	Warburg element
WE	working electrode
XRR	X-ray reflectivity
XPS	X-ray photoemission spectroscopy

10. Bibliography

Adlkofer K., Tanaka M., Hillebrandt H., Wiegand G., Sackmann E., Bolom T., Deutschmann R., Abstreiter G. (2000). "Electrochemical passivation of gallium arsenide surface with organic self-assembled monolayers in aqueous electrolytes." *Applied Physics Letters*, *76*, 3313.

Adlkofer A., Tanaka M. (2001). "High Electric Resistance Polymer/Lipid Composite Films on Indium-Tin-Oxide Electrodes." *Langmuir*, 17, 4267.

Allongue P., Cachet H., (1985). "Band-Edge Shift and Surface Charges at Illuminated n-GaAs / Aqueous Electrolyte Junctions: Surface-State Analysis and Simulation of Their Occupation Rate." *Journal ot the Electrochemical Society*, *132*, 45

Allred A. (1961), "Electronegativity values from thermochemical data." *Journal of Inorganic and Nuclear Chemistry* 17, 215 – 221.

Als-Nielsen J, McMorrow D. (2011). „Elements of modern X-ray physics." *John Wiley & Sons.*

Ambacher O., Smart J., Shealy J. R., Weimann N. G., Chu K., Murphy M., Schaff W. J., Eastman L. F., Dimitrov R., Wittmer L., Stutzmann M., Rieger W., and Hilsenbeck J. (1999), "Two-dimensional electron gases induced by spontaneous and piezoelectric polarization charges in N- and Ga-face AlGaN/GaN heterostructures." *Journal of Applied Physics* 85, 3222 – 3233.

Ambacher O., Foutz B., Smart J., Shealy J. R., Weimann N. G., Chu K., Murphy M., Sierakowski A. J., Schaff W. J., Eastman L. F., and et al. (2000). "Two dimensional electron gases induced by spontaneous and piezoelectric polarization in undoped and doped AlGaN/GaN heterostructures." *Journal of Applied Physics* 87, 334 – 344.

Arikuma Y., Nakayama, H., Morita T., Kimura S. (2010) "Electron Hopping over 100 Å Along an α Helix."*Angewandte Chemie International Edition,* vol. 49, pp. 1800-1804, 2010.

Ashkenasy G., Cahen D., Cohen R., Shanzer A., Vilan A. (2002), *Acc. Chem. Res.*, *35*, 121.

Axelrod, D., Koppel D. E., Schlessinger J., Elson E.and Webb W. W. (1976). "Mobility measurement by analysis of fluorescence photobleaching recovery kinetics." *Biophysical Journal* 16(9): 1055-1069.

Bard, A.J.; Faulkner L.R. (2000). "Electrochemical Methods: Fundamentals and Applications." (2 ed.). *John Wiley & Sons* Chichester, John Wiley & Sons Ltd.

Baur B., Howgate J., von Ribbeck H. G., Gawlina Y., Bandalo V., Steinhoff G., Stutzmann M. and Eickhoff M. (2006). "Catalytic activity of enzymes immobilized on AlGaN/GaN solution gate field-effect transistors." *Applied Physics Letters*, 89(18).

Baur B., Steinhoff G., Hernando J., Purrucker O., Tanaka M., Nickel B., Stutzmann M., Eickhoff M. (2005), *Applied Physics Letters*, *87*, 263901

Beauchamp, A. L., Israeli J. and Saulnier H. (1969). "Reaction of metallic nitrilotriacetates with histamine." *Canadian Journal of Chemistry*, 47: 1269-1273.

Benedetti, E., Di Blasio, B., Pavone, V., Pedone, C., Santini, A., Crisma, M. & Toniolo, C. (1991) "in Molecular Conformation and Biological Interactions." Balaram, P. & Ramaseshan, s., Eds., *Indian Academy of Science*, Bangalore, pp. 497-502.

Bergveld, P. (1986). "The Development and Application of Field Effect Transistor-based Biosensors." *Biosensors*, 2(1): 15-34.

Bergveld P. (2003). "*Thirty years of ISFET-TECHNOLOGY:* What happened in the past 30 years and what may happen in the next 30 years." *Sensors and Actuators B*, *88*, 1.

Bernardini F., Fiorentini V., and Vanderbilt D. (1997), "Spontaneous polarization and piezoelectric constants of III-V nitrides." *Physical Review B*, 56, R10024 – R10027.

Biebuyck H. A. and Whitesides G. M. (1993). "Interchange between monolayers on gold formed from unsymmetrical disulfides and solutions of thiols: evidence for sulfur-sulfur bond cleavage by gold metal." *Langmuir*, 9, 1766-1770.

Binnig, G.; Quate, C. F.; Gerber, C. (1986). "Atomic Force Microscope." *Physical Review Letters*, 56: 930–933.

Born M, Wolf E. (1999). "Principles of optics: electromagnetic theory of propagation, interference and diffraction of light." *Cambridge university press*.

Brzoska J. B., Shahidzadeh N., Rondelez F. (1992). „Evidence of a transition temperature for the optimum deposition of grafted monolayer coatings." *Nature*, 360 , 719 – 721.

Burgess, A. W. and Leach S. J. (1973). "Obligatory alpha-helical amino-acid residue." *Biopolymers*, 12(11): 2599-2605.

Cantatore E., Geuns T. C. T., Gelinck G. H., Van Veenendaal E., Gruijthuijsen A. F. A., Schrijnemakers L., Drews S., and De Leeuw D. M. (2007). "A 13.56-MHz RFID System Based on Organic Transponders." *IEEE Journal of Solid-State Circuits*, 42, 84.

Cassie, A. B. D.; Baxter, S. (1944). "Wettability of porous surfaces." *Transactions of the Faraday Society* 40 (0).

Cevc G., editor (1993). *Phospholipids Handbook*. Marcel Dekker, New York.

Chen W. Q. and Hark S. K. (1995), "Strain-induced effects in (111)-oriented InAsP/InP, InGaAs/InP, and InGaAs/InAlAs quantum wells on InP substrates." *Journal of Applied Physics* 77, 5747 – 5750.

Chen S., Svedendahl M., Duyne R. P. V., and Kall M. (2011). "Plasmon-enhanced colorimetric ELISA with single molecule sensitivity." *Nano Letters*, 11, 1826 – 1830.

Chi Q., Wang G., Jiang J. (2013). "The persistence length and length per base of single-stranded DNA obtained from fluorescence correlation spectroscopy measurements using mean field theory." *Physica A*, Volume 392, Issue 5, 1, 1072-1079.

Chibowski, E. (2008). "Surface free energy of sulfur—Revisited I. Yellow and orange samples solidified against glass surface." *Journal of Colloid and Interface Science*, 319 (2): 505–13.

Clark L. C. and Lyons C. (1962). "Electrode systems for continuous monitoring in cardiovascular surgeries." *Annals of the New York Academy of Sciences,* 102, 29 – 45.

Comper W.D. (1996). "Extracellular Matrix*"*. *Harwood Academic Publishers*, Amsterdam.

Compton AH. (1923). "A quantum theory of the scattering of X-rays by light elements." *Physical Review* 21, 483.

Cui Y., Wei Q. Q., Park H. K. and Lieber C. M. (2001). "Nanowire nanosensors for highly sensitive and selective detection of biological and chemical species." *Science*, 293(5533): 1289-1292.

de Levie D. (1989). "On the impedance electrodes with rough interfaces." *Journal of Electroanalytical Chemistry*, 261:1.

Derjaguin B.V. and. Churaev N.V (1987). "Surface Forces". *Consultants Bureau*, NewYork, 1987.

Erokhina S., Berzina T., Cristofolini L., Konovalov O., Erokhin V. and Fontana M.P. *(2007). "*Interaction of DNA Oligomers with Cationic Lipidic Monolayers: Complexation and Splitting." *Langmuir,* Vol. 23, No. 8.

Finklea H. O., Snider D. A., Fedyk J., Sabatani E., Gafni Y., Rubinstein I. (1993). "Characterization of octadecanethiol-coated gold electrodes as microarray electrodes by cyclic voltammetry and ac-impedance spectroscopy." *Langmuir*, 9(12):3660–3667.

Frenkel N., Wallys J., Lippert S., Teubert J., Kaufmann S., Das A., Monroy E., Eickhoff M., Tanaka M., (2014). „High Precision, Electrochemical Detection of Reversible Binding of Recombinant Proteins on Wide Bandgap GaN Electrodes Functionalized with Biomembrane Models." *Advanced Functional Materials*, *24*, 4927–4934.

Frenkel N. (2015). "Creation of Novel Biochemical Sensor Platforms by Functionalization of GaN-based Semiconductors with Soft Interlayers." PhD thesis, Heidelberg University

Fritze S., Dadgar A., Witte H., Bügler M., Rohrbeck A., (2012). „High Si and Ge n-type doping of GaN doping - Limits and impact on stress." Applied Physics Letters, 100, 122104.

Fromherz P., Offenhausser A., Vetter T., and Weis J. (1991). „A neuron-silicon junction - a retzius cell of the leech on an insulated-gate field-effect transistor." *Science*, 252(5010):1290–1293.

Furukawa K., Ueno Y., Tamechika E. and Hibino H. (2013) "Protein recognition on a single graphene oxide surface fixed on a solid support." *Journal of Materials Chemistry B*, 1, 1119–1124.

Fujita K., Kimura S., Imanishi Y., Okamura E., Umemura J., (1995). "Monolayer formation and molecular orientation of various helical peptides at the air/water interface."*Langmuir*, 11, 1675.

Fujita K., Bunjes N., Nakajima K., Hara M., Sasabe H., Knoll W. (1998). "Macrodipole Interaction of Helical Peptides in a Self-Assembled Monolayer on Gold Substrate." *Langmuir,* vol. 14, pp. 6167-6172.

Fujiwara, H. (2007). "Spectroscopic Ellipsometry: Principles and Applications." *John Wiley & Sons, Ltd,* Chichester, England.

Gassull D., Ulman A., Grunze M. and Tanaka M. (2008). "Electrochemical Sensing of Membrane Potential and Enzyme Function Using Gallium Arsenide Electrodes Functionalized with Supported Membranes." *Journal of Physical Chemistry B*, *112,* 5736-5741.

Gebinoga M., Mai P., Donahue M., Kittler M., Cimalla I., Lubbers B., Klett M., Lebedev V., Silveira L., Singh S., and Schober A. (2012). "Nerve cell response to inhibitors recorded with
an aluminum-galliumnitride/galliumnitride field-effect transistor." *Journal of Neuroscience Methods*, 206, 195 – 199.

Gönnenwein S., Tanaka M., Hu B., Moroder L., and Sackmann E. (2004). „Functional incorporation of integrins into solid supported membranes on ultrathin films of cellulose: Impact on adhesion." *Biophysical Journal*, 85:846–855.

Gray, P. R.; Hurst, P. J.; Lewis, S. H. & Meyer, R. G. (2001). "Analysis and Design of Analog Integrated Circuits" (Fourth ed.). *John Wiley & Sons, Ltd*, New York, 66–67.

Gritsch, S., P. Nollert, F. Jahnig and E. Sackmann (1998). "Impedance spectroscopy of porin and gramicidin pores reconstituted into supported lipid bilayers on indium-tin-oxide electrodes." *Langmuir*, 14(11): 3118-3125.

Henmi M., Nakatsuji K., Ichikawa T., Tomioka H., Sakamoto T., Yoshio M., and Kato T., (2012). "Self-Organized Liquid-Crystalline Nanostructured Membranes for Water Treatment: Selective Permeation of Ions." *Advanced Materials*, 24, 2238–2241.

Hillebrandt H., Wiegand G., Tanaka M., and Sackmann E. (1999). "High electric resistance polymer/lipid composite films on indium-tin-oxide electrodes." *Langmuir*, 15(24):8451–8459.

Hillebrandt, H. and M. Tanaka (2001). "Electrochemical characterization of self-assembled alkylsiloxane monolayers on indium-tin oxide (ITO) semiconductor electrodes." *Journal of Physical Chemistry B*, 105(19): 4270-4276.

Hillebrandt H., Tanaka M., and Sackmann E. (2002). "A novel membrane charge sensor: Sensitive detection of surface charge at polymer/liquid composite films on indium tin oxide electrodes." *Journal of Physical Chemistry B*, 106:477–486.

Hirschhaeuser F., Sattler U.G.A., Mueller-Klieser W. (2011). „Lactate: A Metabolic Key Player in Cancer." *Cancer Research*, 71, 6921-6925.

Ho C., Raistrick I. D., Huggins R. A. (1980). "Application of ac techniques to the study of lithium diffusion in tungsten trioxide thin-films." *Journal of the Electrochemical Society*, 127(2):343–350.

Hohner A.O., David M.P.C., Rädler J.O., (2010). "Controlled solvent-exchange deposition of phospholipid membranes onto solid surfaces." *Biointerphases*, 5, 1.

Hol W. G. J., Van Duijnen P. T., Berendsen H. J. C. (1978). "The α-helix dipole and the properties of proteins." *Nature*, 273, 443.

Horowitz G., Allonge P., Cachet H., (1984). "Quantitative Comparison of Fermi Level Pinning at GaAs / Metal and GaAs / Liquid Junctions." *Journal of the Electrochemical Society*, 131, 2563.

Howgate J., Schoell S. J., Hoeb M., Steins W., Baur B., Hertrich S., Nickel B., Sharp I. D., Stutzmann M. and Eickhoff M. (2010). „Photocatalytic Cleavage of Self-Assembled Organic Monolayers by UV-Induced Charge Transfer from GaN Substrates." *Advanced Materials* 22(24): 2632–2636.

Huang C.C., Lee G.Y., Chyi J.I., Cheng H.T., Hsu C.P.,. Hsu Y.R, Hsu C.H., Huang Y.F., Sun Y.C., Chen C.C., Li S.S., Yeh J. A., Yao D.J., Ren F. and Wang Y.L. (2013). "AlGaN/GaN high electron mobility transistors for protein-peptide binding affinity study." *Biosensors and Bioelectronics*, 41, 717 – 722.

Hunter S., Chen J., and Anthopoulos T. D. (2014). "Microstructural Control of Charge Transport in Organic Blend Thin-Film Transistors." *Advanced Functional Materials* 24, 5969.

Immergut E., Brandrup J., (1989). "Polymer Handbook", *Wiley*, New York, NY, USA.

Israelachvili J. N. (1985). "Intermolecular and Surface Forces with Applications to Colloidal and Biological Systems." *Academic Press Inc*., London.

Kaindl T., Adlkofer K., Morita T., Umemura J., Konovalov O., Kimura S. and Tanaka M. (2010). "Modulation of Band Bending of Gallium Arsenide with Oriented Helical Peptide Monolayers." *Journal of Physical Chemistry C*, 114 (51), pp 22677–22683.

Kang B. S., Ren F., Wang L., Lofton C., Tan W. W., Pearton S. J., Dabiran A., Osinsky A., and Chow P. P. (2005). "Electrical detection of immobilized proteins with ungated AlGaN/GaN high-electronmobility transistors." *Applied Physic Letters,* 87, 023508.

Kang Y.W., Lee G.Y., Chyi J.I., Hsu C.P., Hsu Y.R., Hsu C.H., Huang Y.F., Sun Y.C., Chen C.C., Hung S. C., Ren F., Yeh J. A., and Wang Y.L. (2013). "Human immunodeficiency virus drug development assisted with AlGaN/GaN high electron mobility transistors and binding-site models." *Applied Physic Letters*, 102, 173704.

Karle I. L. and Balaram P. (1990). "Structural characteristics of alpha-helical peptide molecules containing Aib residues." *Biochemistry,* 29(29): 6747-6756.

Kim J. (2011). "Formation, Structure, and Reactivity of Amino-Terminated Organic Films on Silicon Substrates." *Interfaces and Interphases in Analytical Chemistry*, Chapter 6, pp 141–165.

Kimura S. (2008). "Molecular dipole engineering: new aspects of molecular dipoles in molecular architecture and their functions." *Organic & Biomolecular Chemistry* 6(7): 1143-1148.

Kitagawa K., Morita T., Umemura J., Kimura S. (2002). "Influence of Subphase on the Orientation of Helical Peptides at Interface." *Polymer*, 43, 3533.

Kitagawa K., Morita T. and Kimura S. (2004). "Observation of single helical peptide molecule incorporated into alkanethiol self-assembled monolayer on gold by scanning tunneling microscopy." *Journal of Physical Chemistry B*, 108(39): 15090-15095.

Knopfmacher O., Hammock M. L., Appleton A. L., Schwartz G., Mei J.,. Lei T, Pei J., and Bao Z. (2014). "Highly stable organic polymer field-effect transistor sensor for selective detection in the marine environment." *Nature Communication*, 5, 2954.

Lantzsch, G., Binder H., Heerklotz H., Wendling M. and Klose G. (1996). "Surface areas and packing constraints in POPC/C(12)EO(n) membranes. A time-resolved fluorescence study." *Biophysical Chemistry* 58(3): 289-302.

Lei T., Fanciulli M., Molnar R. J., Moustakas T. D., Graham R. J., and Scanlon J. (1991). "Epitaxial growth of zinc blende and wurtzitic gallium nitride thin films on (001) silicon." *Applied Physics Letters* 59, 944 – 946.

Levinshtein M. E., Rumyantsev S. L., Shur M. S. (2001)"Properties of Advanced Semiconductor Materials." *Wiley*, New York, NY, USA, pp. 1.

Lieber C. M.(1993). "Nanomachining and Manipulation with Atomic Force microscope." *Advanced Functional Materials*, 5, 5.

Lin P., Yan F. (2012). "Organic Thin-Film Transistors for Chemical and Biological Sensing." *Advanced Materials*, 24(1):34-51.

Lindholm-Sethson B. (1996). "Electrochemistry at ultrathin organic films at planar gold electrodes." *Langmuir*, 12(13):3305–3314.

Liu C., Li Y., Lee M. V., Kumatani A., and Tsukagoshi K. (2013). "Self-assembly of semiconductor/insulator interfaces in one-step spin-coating: a versatile approach for organic field-effect transistors." *Physical Chemistry Chemical Physics.* 15, 7917.

Lu N., Dai P., Gao A., Valiaho J., Kallio P., Wang Y. and Li T. (2014). "Label-Free and Rapid Electrical Detection of hTSH with CMOS-Compatible Silicon Nanowire Transistor Arrays**.**" *ACS Applied Materials & Interfaces*, 6, 20378-20384.

Luber S., Adlkofer A., Rant U., Ulman A., Gölzhäuser A., Grunze M., Schuh D., Tanaka M., Tornow M., Abstreiter G. (2004), *Physica E*, *21*, 1111.

Macdonald J. R. (1994). "Power-law exponents and hidden bulk relation in the impedance spectroscopy of solids." *Journal of Electroanalytical Chemistry*, 378(1-2):17–29.

Macdonald, J. R. and W. R. Kenan (1987). "Impedance Spectroscopy: Emphasizing Solid Materials and Systems." *John Wiley & Sons, Inc*.

Manning G.S., (2006). "The Persistence Length of DNA Is Reached from the Persistence Length of Its Null Isomer through an Internal Electrostatic Stretching Force." *Biophysical Journal*, 15; 91(10): 3607–3616.

Marshall G. R. and Bosshard H. E. (1972). "Angiotensin II Studies on the Biologically Active Conformation." *Circulation Research Supplement*, 31(9 SUPPL 2): 143-150.

Mehlhose S., Frenkel N., Uji H., Hölzel S., Müntze G., Stock D., Neugebauer S., Dadgar A., Abuillan W., Eickhoff M., Kimura S.,Tanaka M. (2018). „Flexible Modulation of Electronic Band Structures of Wide Band Gap GaN Semiconductors Using Bioinspired, Nonbiological Helical Peptides." *Advanced Functional Materials*, 28, 1704034.

Makita T., Sasaki M., Annaka T., Sasaki M., Matsui H., Mitsui C., Kumagai S., Watanabe S., Hayakawa T., Okamoto T. and Takeya J. (2017). "Spontaneously formed high-performance charge-transport layers of organic single-crystal semiconductors on precisely synthesized insulating polymers." Applied Physics Letters, 110, 163302.

Makowski M. S., Bryan I., Sitar Z., Arellano C., Xie J., Collazo R., and Ivanisevic A. (2013). "Kinase detection with gallium nitride based high electron mobility transistors." *Applied Physics Letters*, 103, 013701.

Merkel, R., Sackmann E. and Evans E. (1989). "Molecular Friction and Epitactic Coupling between Monolayers in Supported Bilayers." *Journal de Physique* 50(12): 1535-1555.

Middleman S., Hochberg A.K. (1993). "Process Engineering Analysis in Semiconductor Device Fabrication." *McGraw-Hill*, p. 313.

Minami T., Minamiki T., Hashima Y., Yokoyama D., Sekine T., Fukuda K., Kumaki D., Tokito S. (2014). "An extended-gate type organic field effect transistor functionalised by phenylboronic acid for saccharide detection in water." *Chemical Commun*ications, 50, pp. 15613-15615.

Mitsui C., Okamoto T., Yamagishi M., Tsurumi J., Yoshimoto K., Nakahara K., Soeda J., Hirose Y., Sato H., Yamano A., Uemura T., and Takeya J. (2014). "High-Performance Solution-Processable N-Shaped Organic Semiconducting Materials with Stabilized Crystal Phase." *Advanced Materials,* 26, 4546–4551.

Miura Y., Kimura S., Imanishi Y., Umemura J., (1998). "Formation of Oriented Helical Peptide Layers on a Gold Surface Due to the Self-Assembling Properties of Peptides." *Langmuir*, 14, 6935.

Morita T., Kimura S., Kobayashi S., Imanishi Y.(2000). "Photocurrent generation under a large dipole moment formed by self-assembled monolayers of helical peptides having an N-ethylcarbazolyl group." *Journal of the American Chemical Society,122, 2850–2859.*

Morita T. and Kimura S. (2003)."Long-Range Electron Transfer over 4 nm Governed by an Inelastic Hopping Mechanism in Self-Assembled Monolayers of Helical Peptides." *Journal of the American Chemical Society,* vol. 125, pp. 8732-8733.

Mooney J. F., Hunt A. J., McIntosh J. R., Liberko C. A., Walba D. M. and Rogers C. T. (1996). "Patterning of functional antibodies and other proteins by photolithography of silane monolayers." *Proceedings of the National Academy of Sciences of the United States of America*, 93(22): 12287-12291.

Nelson, A. (2006). "Co-Refinement of Multiple-Contrast Neutron/X-Ray Reflectivity Data Using Motofit." *Journal of Applied Crystallography*, 39(2): 273-276.

Nicholson, R.S.; Shain, I., (1965). "Theory of Stationary Electrode Polarography for a Chemical Reaction Coupled between Two Charge Transfers." *Analytical Chemistry*, 36, 706.

Nissen J., Gritsch S., Wiegand G., and Radler J. O. (1999). "Wetting of phospholipid membranes on hydrophilic surfaces—concepts towards self-healing membranes." *The European Physical Journal B*, 10:335–344.

Norrman, A. Ghanbari-Siahkali, Larsen N. B. (2005). „Studies of spin-coated polymer films*." Annual Reports on Progress of Chemistry, Section C: Physical Chemistry,*101, S. 174–201

Nuzzo R. G., Fusco F. A., and Allara D. L. (1987). "Spontaneously organized molecular assemblies. 3. Preparation and properties of solution adsorbed monolayers of organic disulfides on gold surfaces." *Journal of the American Chemical Society*, 109, 2358-2368.

Otoda K., Kitagawa Y., Kimura S. and Imanishi Y. (1993). "Chain length dependent transition of 310- to α-helix of Boc-(Ala-Aib)n-OMe." *Biopolymers*, 33(9): 1337-1345.

Parratt LG. (1954). Surface studies of solids by total reflection of X-rays. *Physical Review*, 95, 359.

Poisson A. , Papaud A. (1983). "Diffusion Coefficients of Major Ions in Sea Water". *Marine Chemistry*, 13, 265-280.

Popkirov G. S. and Schindler R. N. (1992). "A new impedance spectrometer for the investigation of electrochemical systems." *Review of Scientific Instruments*, 63(11):5366–5372.

Popkirov G. S.and Schindler R. N. (1993). „Optimization of the perturbation signal for electrochemical impedance spectroscopy in the time-domain." *Review of Scientific Instruments*, 64(11):3111–3115.

Purrucker O., Hillebrandt H., Adlkofer K., and Tanaka M. (2001). "Deposition of highly resistive lipid bilayer on silicon-silicon dioxide electrode and incorporation of gramicidin studied by ac impedance spectroscopy." *Electrochimica Acta*, 47(5):791–798.

Rädler J., Strey H., Sackmann E. (1995). "Phenomenology and Kinetics of Lipid Bilayer Spreading on Hydrophilic Surfaces." *Langmuir* 1995, *11*, 4539-4548.

Randles J. E. B. (1947). "Kinetics of rapid electrode reactions." *Discussions of the Faraday Society*, 1:11–19.

Rehfeldt F. and Tanaka M. (2003). "Hydration Forces in Ultrathin Films of Cellulose." *Langmuir, 19,* 1467-1473.

Rentschler M. and Fromherz P. (1998). "Membrane-transistor cable." *Langmuir* 14(2): 547-551.

Russell T. (1990). "X-ray and neutron reflectivity for the investigation of polymers." *Materials Science Reports* 5, 171-271.

Röntgen WC. (1898). „Über eine neue Art von Strahlen." *Annalen der Physik*, 300, 1-11.

Rossetti F.F., Panagiotou P., Rehfeldt F., Schneck E., Dommach M., Funari S. S., Timmann A., Müller-Buschbaum P., and Tanaka M. (2008). „Structures of regenerated cellulose films revealed by grazing incidence small-angle X-ray Scattering." *Biointerphases*, 3, 117.

Rossetti F.et al. (2015). „Generic Role of Polymer Supports in the Fine Adjustment of Interfacial Interactions between Solid Substrates and Model Cell Membranes." *Langmuir*, 31, 4473−4480

Sackmann E. (1996). "Supported Membranes: Scientific and Practical Applications." *Science* 271(5245): 43-48.

Sackmann, E. and M. Tanaka (2000). "Supported membranes on soft polymer cushions: fabrication, characterization and applications." *Trends in Biotechnology* 18(2): 58-64.

Saier M. H., Yen M. R., Noto K., Tamang D. G. and Elkan C. (2009). "The Transporter Classification Database: recent advances". *Nucleic Acids Research, 37.*

Sakamoto T., Ogawa T., Nada H., Nakatsuji K., Mitani M., Soberats B., Kawata K., Yoshio M., Tomioka H., Sasaki T., Kimura M., Henmi M., and Kato T., (2018). "Development of Nanostructured Water Treatment Membranes Based on Thermotropic Liquid Crystals: Molecular Design of Sub-Nanoporous Materials" *Advanced Science*, *5*, 1700405.

Salditt T*, et al.* (2002). *"*X-ray reflectivity of solid-supported, multilamellar membranes." *The European Physical Journal E,* 7, 105-116.

Schaefer S.,. Koch A. H. R, Cavallini A., Stutzmann M. and Sharp I. D. (2012). "Charge Transfer across the n-Type GaN-Electrolyte Interface." *Journal of Physical Chemistry C* 116(42): 22281-22286.

Schaub M., Wenz G., Wegner G., Stein A. and Klemm D. (1993). „Ultrathin films of cellulose on silicon wafers." *Advanced Materials*, 5, 919–922.

Schmitt L., Dietrich C. and Tampe R. (1994). "Synthesis and Characterization of Chelator-Lipids for Reversible Immobilization of Engineered Proteins at Self-Assembled Lipid Interfaces." *Journal of the American Chemical Society*, 116(19): 8485-8491.

Schmuki P., Böhni H., Bardwell J. A. (1995). *Journal of the Electrochemical Society*. 142 , 1705 – 1712.

Schubert T., Steinhoff G., von Ribbeck H.-G., Stutzmannn M., Eickhoff M., Tanaka M. (2009). *The European Physical Journal E*, 30, 233.

Sengupta, D., Behera, R. N., Smith, J. C., Ullmann, G. M. (2005). "The alpha helix dipole: screened out?" *Structure*, *13*, 849.

Shiwaku R., Takeda Y., Fukuda T., Fukuda K., and Matsui H. (2016). "Printed 2 V-operating organic inverter arrays employing a small-molecule/polymer blend." Science Reports 6, 34723.

Sigl H., Brink G., Seufert M., Schulz M., Wegner G. and Sackmann E. (1997). "Assembly of polymer/lipid composite films on solids based on hairy rod LB-films." *European Biophysics Journal* 25(4): 249-259

Sluyters J. H. and Oomen J. J. C. (1960). "On the impedance of galvanic cells .2. experimental verification." *Recueil Des Travaux Chimiques Des Pays-Bas-Journal of the Royal Netherlands Chemical Society*, 79(8):1101–1110.

Smith J., Zhang W., Sougrat R., Zhao K., Li R., Cha D., Amassian A., Heeney M., McCulloch I., and Anthopoulos T. D. (2012). "Solution- Processed Small Molecule- Polymer Blend Organic Thin- Film Transistors with Hole Mobility Greater than 5 cm^2/Vs." *Advanced Materials*, 24, 2441.

Smorchkova I. P., Elsass C. R., Ibbetson J. P., Vetury R., Heying B.,. Fini P, Haus E., DenBaars S. P., Speck J. S., and Mishra U. K. (1999), "Polarization-induced charge and electron mobility in AlGaN/GaN heterostructures grown by plasma-assisted molecularbeam Epitaxy." *Journal of Applied Physics*, 86, 4520 – 4526.

Soeda J., Okamoto T., Mitsui C., and Takeya J., (2016). "Stable growth of large-area single crystalline thin films from an organic semiconductor/polymer blend solution for high-mobility organic field-effect transistors." *Organic Electronics*, 39, 127.

Soumpasis D. M. (1983). *Biophysical Journal*, *41* , 95 – 98.

Steinhoff G., Baur B., Wrobel G., Ingebrandt S., Offenhausser A., Dadgar A., Krost A., Stutzmann M. and Eickhoff M. (2005). "Recording of cell action potentials with AlGaN/GaN field-effect transistors." *Applied Physics Letters*, 86(3).

Steinhoff G., Hermann M., Schaff W. J., Eastman L. F., Stutzmann M. and Eickhoff M. (2003). "pH response of GaN surfaces and its application for pH-sensitive field-effect transistors." *Applied Physics Letters*, 83(1): 177-179.

Steinhoff G., Purrucker O., Tanaka M., Stutzmann M., Eickhoff M. (2003). "pH-Response of GaN Surfaces and its Application in pH-Sensitive Field Effect Transistors", Advanced Functional Materials, 13, 841.

Stelzle M., G. Weissmuller and E. Sackmann (1993). "On the application of supported bilayers as receptive layers for biosensors with electrical detection." *Journal of Physical Chemistry*, 97(12): 2974-2981.

Stine R., Simpkins B. S, Mulvaney S. P., Whitman L. J. and Tamanaha C. R. (2010). "Formation of amine groups on the surface of GaN: A method for direct biofunctionalization." *Applied Surface Science*, 256(13): 4171-4175.

Sze S. M. (1985). Semiconductor Devices: Physics and Technology. *JohnWiley & Sons*, NewYork.

Tadmor R. (2004). "Line energy and the relation between advancing, receding, and Young contact angles." *Langmuir*. 20 (18): 7659–64.

Tanaka M., Hermann J., Haase I., Fischer M.and Boxer S. G. (2007). "Frictional Drag and Electrical Manipulation of Recombinant Proteins in Polymer-Supported Membranes." *Langmuir*, 23(10): 5638-5644.

Tanaka M., Kaufmann S., Nissen J., and Hochrein M. (2001). „Orientation selective immobilization of human erythrocyte membranes on ultrathin cellulose films." *Physical Chemistry Chemical Physics*, 3(18):4091–4095.

Tanaka M. and Sackmann, E. (2005). "Polymer-supported membranes asmodels of the cell surface." *Nature*, 437(7059):656-663.

Tanaka M. and Sackmann E. (2006). „Supported membranes as biofunctional interfaces and smart biosensor platforms." *Physica Status Solidi a-Applications and Materials Science*, 203(14):3452–3462, 2006.

Tanaka M., Wong A. P., Rehfeldt F., Tutus M., and Kaufmann S. (2004). "Selective deposition of native cell membranes on biocompatible micropatterns." *Journal of the American Chemical Society*, 126(10):3257–3260.

Thapa R., Alur S., Kim K., Tong F., Sharma Y., Kim M., Ahyi C., Dai J., Hong J. W., Bozack M., Williams J., Son A., Dabiran A., and Park M. (2012). "Biofunctionalized AlGaN/GaN high electron mobility transistor for DNA hybridization detection." *Applied Physics Letters* 100.

Thévenot D. R., Toth K., Durst R. A., and Wilson G. S. (2001). "Electrochemical biosensors: Recommended definitions and classification." *Biosensensors and Bioelectronics* 16, 121-131.

Thuselt F. (2005). Physik der Halbleiterbauelemente, *Springer*, Heidelberg.

Tolan M. (1999). "X-Ray Scattering from Soft-Matter Thin Films." *Springer*, Heidelberg.

Toniolo C., Crisma M., Formaggio F. and Peggion C. (2001). "Control of peptide conformation by the Thorpe-Ingold effect (Cα-tetrasubstitution)." *Peptide Science*, 60(6): 396-419.

Torsi L., Magliulo M., Manoli K., Palazzo G. (2013). "Organic field-effect transistor sensors: a tutorial review" *Chemical Society Reviews*, 42, pp. 8612-8628.

Ueno Y., Furukawa K., Matsuo K., Inoue S., Hayashi K., Hibino H. (2015). "On-chip graphene oxide aptasensor for multiple protein detection", *Analytica Chimica Acta*, 866 1–9.

Valincius G., Niaura G., Kazakeviciene B., Talaikyte Z., Kažemekaite M., Butkus E., Razumas V. (2004). *Langmuir*, *20*, 6631.

Verlaak S., Arkhipov V., and Heremans P. (2003). "Modeling of transport in polycrystalline organic semiconductor films." Applied Physics Letters, 82, 745.

Vickerman J. C. and Gimore I. C., Eds. (2009). "Surface Analysis - The Principal Techniques." *John Wiley & Sons, Ltd*, New York.

Wada A. (1976). "The alpha-helix as an electric macro-dipole." *Advances in Biophysics*, 1-63.

Wang, J., (2000). Analytical Electrochemistry, Chapter 2, *John Wiley & Sons Ltd*, Chichester.

Wegner G. (1992). "Ultrathin films of polymers: architecture, characterization and properties." *Thin Solid Films*, *216*, 105-116.

Wegner G. (1993). "Control of molecular and supramolecular architecture of polymer, polymer systems and nanocomposites." *Molecular Crystals and Liquid Crystals*, *235*, 1-34.

Wenzel R. N. (1936). "Resistance of solid surfaces to wetting by water." *Industrial and engineering chemistry,* 28, 988.

Wiegand G., Neumaier K. R., and Sackmann E., (2000). "Fast impedance spectroscopy: General aspects and performance study for single ion channel measurements." *Review of Scientific Instruments*, 71(6):2309–2320.

Yagi I., Hirai N., Miyamoto Y., Noda M., Imaoka A., Yoneya N., Nomoto K., Kasahara J., Yumoto A., and Urabe T. (2008). "A flexible full-color AMOLED display driven by OTFTs." *Journal of the Society for Information Displays*, 16, 15.

Zhang X., Ma X., Dou F., Zhao P., and Liu H. (2011). "A biosensor based on metallic photonic crystals for the detection of specific bioreactions." *Advanced Functional Materials*, 21, 4219 – 4227.

Zhong Q, Inniss D, Kjoller K, Elings V (1993). "Fractured polymer/silica fiber surface studied by tapping mode atomic force microscopy." *Surface Science Letters*, 290: L688.

11. Scientific Contributions

- Mehlhose S., Frenkel N., Uji H., Hölzel S., Müntze G., Stock D., Neugebauer S., Dadgar A., Abuillan W., Eickhoff M., Kimura S.,Tanaka M. (2018). „Flexible Modulation of Electronic Band Structures of Wide Band Gap GaN Semiconductors Using Bioinspired, Nonbiological Helical Peptides." *Advanced Functional Materials*, 28, 1704034.